
RICH TOWNSEND

STELLAR ASTROPHYSICS

DEPARTMENT OF ASTRONOMY, UW-MADISON

Copyright © 2019–2021 Rich Townsend

This version: December 14, 2021

Contents

1	<i>Position, Brightness & Magnitude</i>	9
2	<i>Color & Temperature</i>	11
3	<i>The Hertzsprung-Russell Diagram</i>	13
4	<i>Mass Equation & Gravity</i>	15
5	<i>Momentum Equation & Hydrostatic Equilibrium</i>	17
6	<i>The Ideal Gas</i>	19
7	<i>The Virial Theorem</i>	21
8	<i>Pre-Main Sequence Evolution</i>	23
9	<i>The Ignition of Hydrogen</i>	25
10	<i>Energy Equation & Thermal Equilibrium</i>	27
11	<i>Opacity & Optical Depth</i>	29
12	<i>Radiative Transport & Opacity Sources</i>	31
13	<i>Convective Stability</i>	33
14	<i>Convective Transport</i>	35

15	<i>The Full Equation of State</i>	37
16	<i>Electron Degeneracy</i>	39
17	<i>Ionization</i>	41
18	<i>The Overall Problem</i>	43
19	<i>Polytropes</i>	45
20	<i>Fully Convective Stars</i>	47
21	<i>The Main Sequence</i>	49
22	<i>Hydrogen Burning Reactions</i>	51
23	<i>The Red Giant Branch</i>	53
24	<i>The Helium Flash</i>	55
25	<i>The Horizontal Branch</i>	57
26	<i>The Asymptotic Giant Branch</i>	59
27	<i>Thermal Pulses & Mass Loss</i>	61
28	<i>White Dwarfs</i>	63
29	<i>Low-Mass Stellar Evolution</i>	65

30	<i>Binary Stars</i>	67
31	<i>Binary Orbits</i>	69
32	<i>Observing Binaries</i>	71
33	<i>Binary Evolution</i>	73
34	<i>Novae</i>	75
35	<i>Thermonuclear Supernovae</i>	77
36	<i>Intermediate-Mass Stellar Evolution</i>	79
37	<i>High-Mass Stellar Evolution</i>	81
38	<i>Core-Collapse Supernovae</i>	83
39	<i>Neutron Stars</i>	85
A	<i>Units & Constants</i>	87

Foreword

About these Handouts

These handouts comprise the primary instructional material for my *Astronomy 310* (Stellar Astrophysics) class at UW-Madison. I first drafted them in 2019, in response to a pair of realizations reached while teaching the class in previous years. First, I felt that none of the existing stellar astrophysics books offered a good balance between rigor and narrative¹. Second, I recognized that the recently developed *MESA* stellar evolution code (discussed further below) offers unique opportunities to illustrate the evolution of stars, thereby following the golden rule of writing: show don't tell.

The handouts are structured so that each fits on a single (two-sided) sheet of letter paper, and contains the right amount of material (more or less) for a 50-minute class. Their layout follows a style pioneered by Edward Tufte², with copious use of sidenotes and marginal figures that illustrate and comment on the main text. Although well suited to printing, the handouts are perhaps best experienced in electronic (PDF) form due to features such as a hyperlinked equation and figure cross-references, and vector-art figures that can be magnified on-screen without loss of detail.

¹ Narrative is especially important in my eyes: stellar astrophysics is telling stories about the lives of stars.

² A world leader in information design, most famous for his seminal book *The Visual Display of Quantitative Information* (yes, I'm a big fan).

Other Resources

At the end of each handout, I provide a 'Further Reading' section that points to relevant chapters and/or sections in three books:

- Kippenhahn, Weigert & Weiss: *Stellar Structure and Evolution*. This is a very thorough and detailed book, but be warned: it is as dry as a bone, lacking the engaging visuals and worked examples that make lower-level textbooks approachable.
- Ostlie & Carroll: *An Introduction to Modern Stellar Astrophysics*. This is a very approachable book although in some places it doesn't go into sufficient detail. Note that the same material is covered in Carroll & Ostlie: *An Introduction to Modern Astrophysics*, but the latter costs more because it covers other material (e.g., galaxies, cosmology).
- Prialnik: *An Introduction to the Theory of Stellar Structure and Evolution*. This offers a slightly more rigorous treatment than Carroll & Ostlie, and takes a refreshingly different perspective on some topics than other texts.

The *MESA* Code

The figures and data appearing in the handouts are almost universally based on stellar models constructed using *MESA*. *MESA* is a *stellar evolution code* — a piece of software that constructs a numerical rep-

resentation of the the interior of a star, and then simulates how this representation evolves over time.

Evolution codes allow us to check and refine the various physical theories that together compose stellar astrophysics (e.g., atomic physics, nuclear physics, fluid dynamics, thermodynamics); they provide laboratories for performing experiments on stars (e.g., discovering what factors contribute to the formation of red giants); and, they shed light on stages of stellar evolution that may be too fleeting to observe directly in the Universe.

While a number of stellar evolution codes exist, almost all are proprietary and unavailable outside restricted research settings. *MESA* is different: it is *open-source*, meaning that anyone can freely download, install and use it³; and it is *open-knowledge*, meaning that the details of how it works are publicized in the scientific literature⁴. Moreover, *MESA* has a large and vibrant global community of users and developers, supported by mailing lists, summer schools and other enrichment activities.

³See <http://mesa.sourceforge.net> for details. If the installation process seems daunting, you may want to consider using *MESA-Web* instead — a simplified web-based portal to *MESA*, available at <http://www.astro.wisc.edu/~townsend/static.php?ref=mesa-web>.

⁴See Paxton et al. (2011, *Astrophys. J. Supp.*, **193**, 3), Paxton et al. (2013, *Astrophys. J. Supp.*, **208**, 4), Paxton et al. (2015, *Astrophys. J. Supp.*, **220**, 15), Paxton et al. (2018, *Astrophys. J. Supp.*, **234**, 34), and Paxton et al. (2019, *Astrophys. J. Supp.*, **243**, 10).

Rich Townsend
Department of Astronomy
University of Wisconsin-Madison

1 Position, Brightness & Magnitude

Position

To specify the position of an object in 3-dimensional space, we require three coordinates. Astronomers use the *Celestial coordinate system*, which is a spherical system centered on the Earth. Two angular coordinates — the *right ascension α* and *declination δ* ¹ — describe the position of a star or other celestial object in the sky; the third coordinate gives the distance d to the object.

Distances are typically specified in *astronomical units* or *parsecs* (see Appendix A for conversions to more familiar units). An astronomical unit (au) is defined as the average distance from the center of the Earth to the center of the Sun. A parsec (pc) is defined so that a star at 1 pc distance will appear to move by an angle $\pm 1 \text{ arcseconds}^2$ relative to the background of more-distant stars, as a consequence of the Earth's year-long orbit around the Sun. More generally, a star at a distance of d will show parallax motion $\pm p$, where

$$d/1 \text{ pc} = \frac{1}{p/1''}. \quad [1.1]$$

(see Fig. 1.1). This formula, which can be derived from the small-angle approximation of trigonometry, allows us to calculate the distance to nearby stars (out to a few thousand parsecs, or kpc) from their parallax motion.

Brightness

When we observe a star from Earth, its apparent brightness depends on how much energy ΔE (in the form of light, or other electromagnetic radiation) is received by the detector. This in turn depends on the exposure time Δt and collection area ΔA of the detector³. We define the *energy flux* from the star as

$$f \equiv \frac{\Delta E}{\Delta t \Delta A} \quad [1.2]$$

The flux from the Sun — known as the *solar constant* — is $1.36 \times 10^6 \text{ erg cm}^{-2} \text{ s}^{-1}$. By contrast, the flux from Sirius (the brightest star in the night sky) is only $1.05 \times 10^{-4} \text{ erg cm}^{-2} \text{ s}^{-1}$.

Sirius appears much dimmer than the Sun because it is much further away. The energy flux from a star varies inversely with the square of the distance from the star to the detector — an instance of the *inverse square law of light*. Mathematically, we can express this as

$$f = \left(\frac{R}{d}\right)^2 F, \quad [1.3]$$

where R is the spherical radius of the star, and F is the hypothetical flux we would measure if we placed our detector right at the star's

¹ Right ascension (often abbreviated RA) is analogous to longitude on the Earth's surface, and declination (abbreviated Dec) is likewise analogous to latitude.

² An arcsecond is small unit of angular measurement, denoted by double apostrophes; $1'' = \frac{1}{3600}^\circ$.

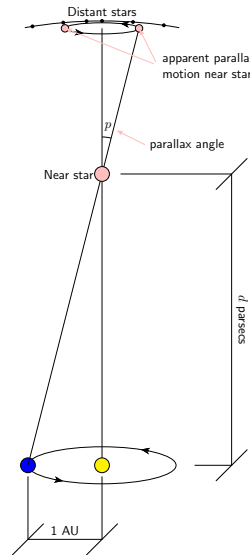


Figure 1.1: Parallax motion due to the Earth's orbit around the Sun.

³ Examples of detectors include the human eye, photographic film, a photo-multiplier tube or a charge-coupled device (CCD). For an unaided human eye under dark conditions, $\Delta t \approx 0.02 \text{ s}$ and $\Delta A \approx 0.5 \text{ cm}^2$. For other detectors, Δt can be much longer. Using binoculars or a telescope provides a way of increasing ΔA .

surface. We can also write this expression as

$$f = \frac{L}{4\pi d^2}, \quad [1.4]$$

where

$$L \equiv 4\pi R^2 F \quad [1.5]$$

is the *luminosity* of the star — the total amount of energy it radiates into space per unit time interval, with units of power. Luminosity is an intrinsic property of a star; unlike f , it does not depend on the star's distance.

Returning to the Sun and Sirius, we can use eqn. [1.4] to calculate their respective luminosities from their measured fluxes and distances ($d_{\odot} = 1 \text{ au}$; $d_{\text{Sirius}} = 2.64 \text{ pc}$). We find the solar luminosity is $3.828 \times 10^{33} \text{ erg s}^{-1} \equiv 1 L_{\odot}$, while the luminosity of Sirius is $8.75 \times 10^{34} \text{ erg s}^{-1} = 22.9 L_{\odot}$ ⁴; hence, although appearing much dimmer than the Sun when viewed from Earth, Sirius is significantly more luminous.

⁴ Here, we've expressed the luminosities in both cgs and solar units; see Appendix A for a discussion of these unit systems.

Magnitude

For historical reasons, astronomers often use a logarithmic scale to quantify the flux from a star. The *apparent magnitude* m of the star is defined by the equation

$$m = -2.5 \log \left(\frac{f}{f_0} \right), \quad [1.6]$$

where f_0 is a constant with units of flux. This definition, which was first proposed by the 19th-Century astronomer Norman Robert Pogson⁵, means that

- brighter stars have less positive (or more negative) magnitudes than dimmer stars;
- stars that differ in apparent magnitude by an additive offset of 5, differ in flux by a multiplicative factor of 100.

A logarithmic scale can also be used to quantify the luminosity of a star. The *absolute magnitude* \mathcal{M} of the star is defined⁶ as

$$\mathcal{M} = -2.5 \log \left(\frac{L}{4\pi[10 \text{ pc}]^2 f_0} \right). \quad [1.7]$$

Combining this expression with eqns. [1.4] and [1.6], we can show that

$$m - \mathcal{M} = 5 \log \left(\frac{d}{10 \text{ pc}} \right). \quad [1.8]$$

The quantity $m - \mathcal{M}$ is known as the *distance modulus*, as it provides an indication of the star's distance.

⁵ Pogson drew inspiration from ancient Greek astronomers, most prominently Hipparchus of Nicaea, who used a system where the brightest stars were assigned a magnitude '1', the next-brightest stars a magnitude '2', and so on through to the dimmest stars visible to the naked eye, with a magnitude '6'.

⁶ With this definition, the absolute magnitude \mathcal{M} of a star corresponds to its hypothetical apparent magnitude m if it were at a distance 10 pc from Earth.

Further Reading

Ostlie & Carroll, §§3.1,3.2; *Prialnik*, §1.2.

2 Color & Temperature

Colors of Stars

Stars exhibit colors that range from red, through yellow and white, to blue (see Fig. 2.1). These colors are due not to differences in composition¹, but rather to differences in surface temperature.

Black-body Radiation

If we heat an opaque enclosure to a finite temperature, the interior cavity will fill with electromagnetic radiation. Through a continual process of absorption and re-emission by the walls of the enclosure, this radiation will eventually approach an equilibrium state that depends only on the temperature T of the walls. This state is known as *black-body radiation*, and to a reasonable level of approximation, stars can be modeled as emitters of black-body radiation.

Suppose we open a small window into the enclosure, allowing the black-body radiation to gradually escape. The energy flux in the narrow wavelength interval $[\lambda, \lambda + d\lambda]$, measured by a detector placed at the window, is given by *Planck's law*:

$$F_\lambda d\lambda = \frac{2\pi hc^2}{\lambda^5} \frac{1}{e^{hc/\lambda k_B T} - 1} d\lambda \quad [2.1]$$

Here, k_B is Boltzmann's constant, h is Planck's constant, and c is the speed of light in vacuum. The quantity F_λ is the *flux density*, with units of flux per unit wavelength interval. Fig. 2.2 plots the black-body flux density for three different temperatures. Each curve exhibits a single peak where F_λ is maximal. Toward higher temperatures, the wavelength λ_{\max} of this peak decreases. The result, when perceived in the visible part of the electromagnetic spectrum, is that hotter black-body radiation appears bluer, while cooler radiation appears redder.

Wien's Law

The dependence of λ_{\max} on temperature is encapsulated in *Wien's law*,

$$\lambda_{\max} = \frac{2.898 \times 10^7 \text{ \AA K}}{T}. \quad [2.2]$$

Wien's law allows us to measure the temperature of a black-body emitter simply by determining λ_{\max} from its flux density.

The Stefan-Boltzmann Law

Integrating Planck's law [2.1] over all wavelengths leads² to the *Stefan-Boltzmann law*,

$$F = \sigma T^4, \quad [2.3]$$

where

$$F \equiv \int_0^\infty F_\lambda d\lambda \quad [2.4]$$

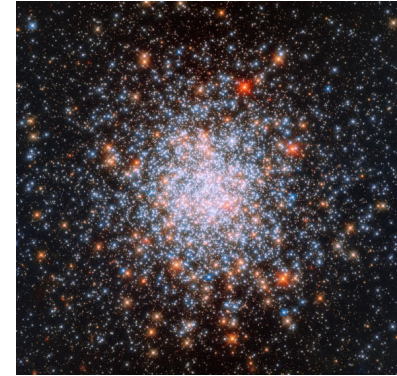


Figure 2.1: The globular cluster NGC 1866 — a spherical collection of hundreds of thousands of stars, packed into a few tens of parsecs. Credit: NASA/ESA/Hubble.

¹ Most stars have a composition similar to the Sun: around 70% (by mass) hydrogen, 28% helium, and the remainder a mixture of heavier elements.

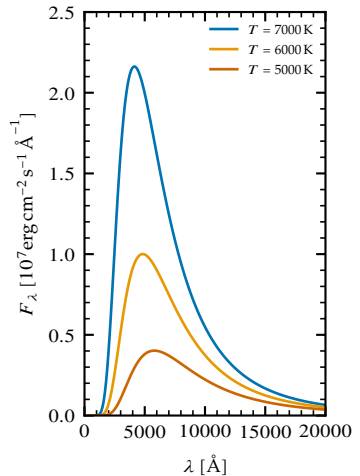


Figure 2.2: The black-body flux density predicted by Planck's law [2.1], plotted against wavelength λ for three choices of the temperature T . The wavelength is measured in angstrom (see Appendix A).

² The derivation involves a bit of math, but is simplified with a change of variables to $u = hc/\lambda k_B T$.

is the total flux measured by the detector, and the Stefan-Boltzmann constant is introduced as

$$\sigma \equiv \frac{2\pi^5 k_B^4}{15h^3 c^2} = 5.6704 \times 10^{-5} \text{ erg cm}^{-2} \text{ s}^{-1} \text{ K}^{-4} \quad [2.5]$$

Similarly to Wien's law, we can use the Stefan-Boltzmann law to determine the temperature of a black-body emitter. However, one complication in this case is that we typically can't measure F directly, but must instead infer it from the flux f measured at a distance from the emitter (cf. eqn. 1.3).

Application to Stars

Real stars aren't black-body emitters; their flux density doesn't follow Planck's law [2.1] exactly. However, as Fig. 2.3 illustrates, they come reasonably close. This motivates us to define the *effective temperature* of a star to be the temperature of a hypothetical black-body emitter that has the same surface flux F as the star:

$$T_{\text{eff}} \equiv \sqrt[4]{\frac{F}{\sigma}}. \quad [2.6]$$

Combining this expression with the relationship [1.5] between F and the star's luminosity L and radius R , we arrive at the Stefan-Boltzmann law as applied to stars,

$$L = 4\pi R^2 \sigma T_{\text{eff}}^4. \quad [2.7]$$

This is one of the most important equations of stellar astrophysics, and we will be making extensive use of it.

In the case of the Sun, careful measurement of L and R (or F , as shown in Fig. 2.3) indicates an effective temperature $T_{\text{eff}} = 5772$ K. For other stars, we can estimate³ T_{eff} by determining λ_{max} from its flux density, and then applying Wien's law. This estimate is a useful stepping stone to other information; for instance, it can be used to obtain (via eqn. [2.7]) a star's luminosity if its radius is already known, or vice versa.

It's tempting to interpret a star's effective temperature as its surface temperature. However, we have to be careful here: stars don't have sharp boundaries, and so there isn't a single outer layer corresponding to the 'surface'. Nevertheless, although the proof lies beyond the scope of these notes, it can be shown that T_{eff} corresponds to the physical temperature at the star's *photosphere* — the thin layer responsible for emitting most of the star's radiation.

Further Reading

Ostlie & Carroll, §3.4; *Prialnik*, §1.2.

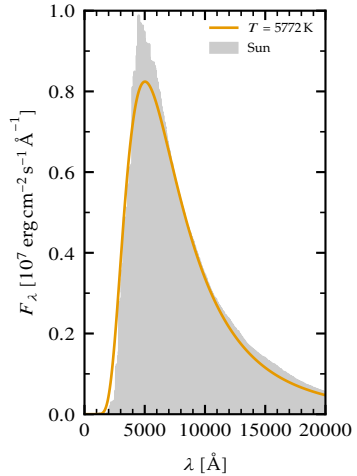


Figure 2.3: The flux density predicted by Planck's law [2.1], plotted against wavelength λ for the Sun's effective temperature $T_{\text{eff}} \approx 5772$ K. The shaded region shows the actual (measured) flux density of the Sun. Due to the way the effective temperature is defined (see eqn. [2.6]), the area under the curves — corresponding to the bolometric flux F — is identical.

³ A more-accurate approach to estimating stellar effective temperatures involves careful analysis of the absorption lines in their spectra, because the strength of these lines changes with T_{eff} .

3 The Hertzsprung-Russell Diagram

Spectral Types

As mentioned briefly in *Handout 2*, the dark absorption lines in stellar spectra (see Fig. 3.1) provide information about the stars' effective temperatures. At the beginning of the 20th century, Annie Jump Cannon devised a classification scheme that assigns stars a *spectral type* from the sequence O-B-A-F-G-K-M¹, on the basis of the strength of various absorption lines. This sequence forms a temperature progression, with O-type stars the hottest and M-type stars the coolest. In the modern form of this scheme, each type is further subdivided into sub-types indicated by an Arabic numeral, with smaller numbers indicating earlier (hotter) in the sequence. The Sun ($T_{\text{eff}} = 5772 \text{ K}$) is a G2 star, while Sirius ($T_{\text{eff}} = 9940 \text{ K}$) is an A1 star.

The Hertzsprung-Russell Diagram

Building on Cannon's spectral classification scheme, Ejnar Hertzsprung and Henry Norris Russel independently developed a diagram that plots the spectral type of stars against their absolute magnitude. This *Hertzsprung-Russell* (HR) diagram remains the most important visualization tool in stellar astrophysics. Fig. 3.2 shows an early HR diagram created by Russel. The stars are not uniformly distributed across the diagram, but tend to cluster into distinct regions:

- *main-sequence* stars, lying along a diagonal band running from top-left to bottom-right;
- *giant* stars, lying in the upper right;
- *white-dwarf* stars, lying in the lower left.

The names 'giant' and 'dwarf' already hint at the distinction between these regions. To understand them further, we must place the HR diagram on a more quantitative footing.

Quantitative HR Diagrams

Although the original HR diagrams used spectral type and absolute magnitude for their axes, equivalent diagrams can be constructed using effective temperature (or a proxy such as color) on the horizontal axis and luminosity on the vertical one. Fig. 3.3 shows one such HR diagram, plotting $\log T_{\text{eff}}$ versus $\log L$ for a selection of stars out to a distance 30 pc. In keeping with the layout of the original HR diagrams, temperature *decreases* from left-to-right in the diagram.

The main sequence can be clearly seen in the diagram, together with a sprinkling of giant stars and a couple of white dwarfs. Taking the logarithm of the Stefan-Boltzmann law [2.7] applied to stars,

$$\log(L/L_{\odot}) = 4 \log(T_{\text{eff}}/\text{K}) + 2 \log(R/R_{\odot}) + C \quad [3.1]$$

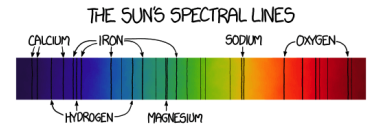


Figure 3.1: A schematic visible-light spectrum of the Sun, showing dark lines superimposed on nearly black-body emission. These lines arise due to preferential absorption of light at certain wavelengths by some of the elements (labeled) present in the solar photosphere. Adapted from the XKCD comic strip at <https://xkcd.com/1733/>.

¹ The sequence is not alphabetical for historical reasons. Earlier attempts at devising a classification scheme focused only on the strength of hydrogen lines, with A-type stars showing the strongest lines and O-type the weakest. Cannon re-ordered this sequence to follow temperature, and eliminated many of the intervening letters.

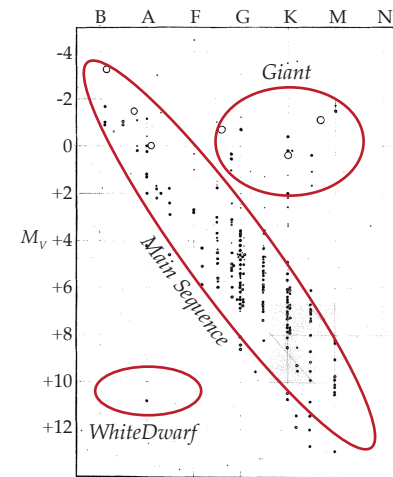


Figure 3.2: An early HR diagram, created by Russel (1914, *Pop. Ast.*, 22, 331) for nearby stars having measured parallaxes. The regions containing the main-sequence, giant and white-dwarf stars have been highlighted by the red ellipses, and the axes have been reworked to make them legible. Spectral type N is no longer used.

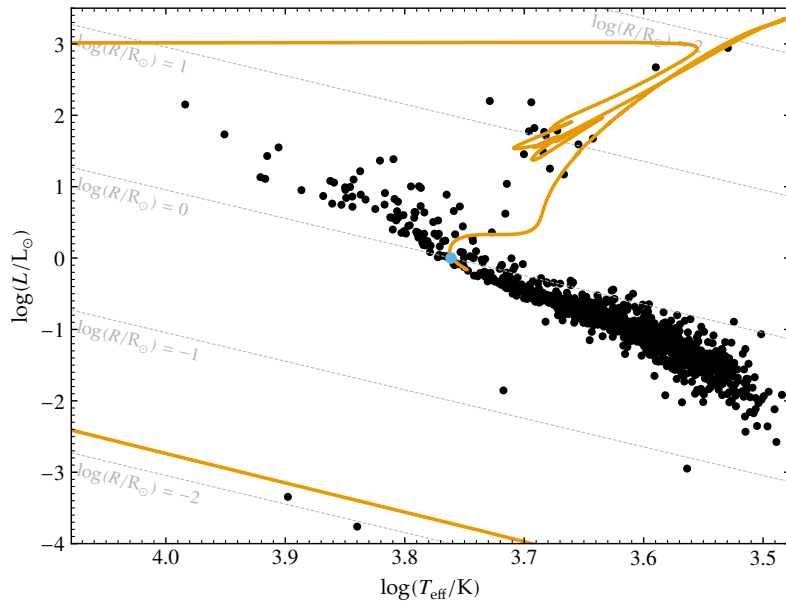


Figure 3.3: An HR diagram for stars within 30 pc of the Earth, comprising 1130 main-sequence stars, 16 giants and 2 white dwarfs (taken from the *Exocat-1* catalog compiled by Margaret Turnbull). The dashed lines mark contours of constant stellar radius, labeled with reference to the solar radius $R_\odot = 6.957 \times 10^{10}$ cm. The orange line shows the evolutionary track of the Sun, calculated using *MESA*; toward the end of the Sun's life, the track disappears off the top-left of the diagram, before reappearing at the bottom left. The blue dot shows the present-day position of the Sun, on the main sequence

where C is a constant; therefore, contours of constant R appear in this HR diagram as straight lines with slope 4. From these contours, we see that giants have radii $R \gtrsim 10 R_\odot$; in fact, the largest giants — known as *supergiants* — can be as large as $R \approx 10^3 R_\odot$. Likewise, white dwarfs exhibit typical radii $R \approx 0.01 R_\odot$, about the same size as the Earth. Main-sequence stars lie between these extremes, with typical radii in the range $0.1 R_\odot \lesssim R \lesssim 10 R_\odot$.

Evolution in the HR Diagram

The different regions of the HR diagram represent stars at different stages in their *evolution*. Stars spend most of their lives on the main sequence, converting hydrogen into helium in their cores via nuclear fusion. When their supplies of hydrogen are exhausted, they evolve to lower effective temperature but larger radius and luminosity, carrying them into the giant region of the HR diagram. Eventually, they shed their outer layers, and move left and then down in the HR diagram to become a white dwarf.

The orange curve plotted in Fig. 3.3 shows the *evolutionary track* that will be followed by the Sun as it passes through these stages. This track isn't a result of observational measurement², but a theoretical prediction by *MESA*³, a software package that applies the knowledge presented in these handouts (and much more) to simulate the structure and evolution of stars. We'll be seeing much more of *MESA* as we progress through the handouts — it's the workhorse for constructing the data featured in most of the plots.

Further Reading

Ostlie & Carroll, §§8.1, 8.2; *Prialnik*, §1.4.

² Over the history of humanity, the Sun has barely changed its position in the HR diagram.

³ Modules for Experiments in Stellar Astrophysics; see <http://mesa.sourceforge.net/>.

4 Mass Equation & Gravity

Preliminaries

In this handout and the subsequent one, we're going to assemble the basic equations governing stellar structure and evolution. The starting point is the presumption¹ of spherical symmetry: we assume that the physical quantities describing the internal structure of a star — density, pressure, temperature, etc. — should depend only on the radial coordinate r and the time t . The center of the star is at $r = 0$, by definition; likewise, remembering that R denotes the stellar radius, the surface of the star is at $r = R$.

Mass Equation

The distribution of matter in a star is described by a pair of connected functions: $\rho(r)$ is the local density at radial coordinate r , while $m(r)$ is the mass of the star contained within the sphere with radius r . This latter quantity is often known as the *interior mass*, to distinguish it from the total stellar mass $M \equiv m(R)$.

The density and interior mass are related by the *mass equation*

$$m(r') = \int_0^{r'} 4\pi r^2 \rho \, dr, \quad [4.1]$$

which can also be written in the differential² form

$$\frac{\partial m}{\partial r} = 4\pi r^2 \rho. \quad [4.2]$$

Because $\partial m / \partial r$ is always positive, m is a monotonic-increasing function of r . Therefore, there is a one-to-one mapping between interior mass and radial coordinate, and we can use m itself as a coordinate for specifying location within the star. For instance, $m = 0.75 M$ corresponds to any point on a centered sphere sized so that 75% of the star's mass lies inside, and the remaining 25% outside.

Fig. 4.1 illustrates the density and interior mass functions for a Sun-similar model. The matter at the center is around 150 times more dense than water, yet it remains in a gaseous state due to its high temperature. Moving from the center to the surface, the density drops rapidly while the interior mass grows steadily.

Gravitational Field

Stars are held together by the gravitational field arising from their mass. This field is described by the gravitational potential Φ , which satisfies the *spherical Poisson equation*

$$\frac{1}{r^2} \frac{\partial}{\partial r} \left(r^2 \frac{\partial \Phi}{\partial r} \right) = 4\pi G \rho \quad [4.3]$$

(here, G is the universal constant of gravitation). Multiplying both sides by r^2 and integrating with respect to r , we obtain an expression

¹ For most stars, this is a very good approximation. Exceptions can arise when a star is rotating rapidly, or when it is distorted by the tidal forces of a binary companion; but we'll neglect these complications for now.

² We use partial derivatives here to highlight the fact that m — and all other dependent variables — also depend on time t .

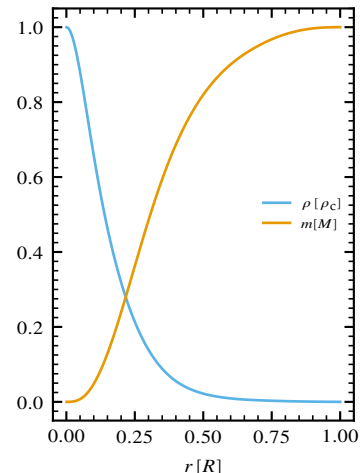


Figure 4.1: The density ρ (in units of its central value $\rho_c = 149 \text{ g cm}^{-3}$) and interior mass m (in units of its surface value $M = M_\odot = 1.989 \times 10^{33} \text{ g}$), plotted as a function of radial coordinate r for a MESA model similar to the present-day Sun. This model has the same mass as the Sun, and is at a similar evolutionary stage; however, its radius ($R = 0.84 R_\odot$) and luminosity ($L = 0.97 L_\odot$) are slightly smaller, and its effective temperature ($T_{\text{eff}} = 6255 \text{ K}$) slightly higher, due to various simplifications that were made during its construction. We'll encounter this model a fair bit in subsequent handouts, and for simplicity we'll label it the ‘Sun-similar’ model.

for the gravitational acceleration (also known just as the *gravity*),

$$g \equiv -\frac{\partial \Phi}{\partial r} = -\frac{Gm}{r^2}. \quad [4.4]$$

Formally, this can be integrated again to obtain the gravitational potential

$$\Phi(r') = \int_{r'}^{\infty} \frac{Gm}{r'^2} dr' + C, \quad [4.5]$$

where the constant of integration C is chosen so that $\Phi \rightarrow 0$ as $r \rightarrow \infty$. Fig. 4.2 illustrates both the gravity and the potential for the Sun-similar model shown in Fig. 4.1. The gravity is strongest around $r \approx 0.2R$, and drops to zero at the center of the star (where the potential is at its minimum).

Gravitational Potential Energy

Imagine assembling a star from the center out, by bringing each successive layer down from infinity to its final position. When adding a new layer with mass dm , the change in its potential energy during the assembly process is³

$$d\Omega = -\frac{Gm}{r} dm, \quad [4.6]$$

Integrating over all layers, we obtain the *gravitational potential energy* of the star

$$\Omega \equiv \int d\Omega = - \int_0^M \frac{Gm}{r} dm. \quad [4.7]$$

The minus sign appears here because energy is released when assembling the star layer-by-layer; $|\Omega|$ is sometimes termed the *binding energy* of the star, because it represents the amount of energy that would have to be injected into the star to disperse it back to infinity.

In most cases it's not possible to evaluate Ω analytically, because r in the integrand of eqn. [4.7] depends on m in a way that's not known *a priori*. Therefore, when making order-of-magnitude estimates, we will often express it as

$$\Omega = -f_\Omega \frac{GM^2}{R}, \quad [4.8]$$

where the 'shape factor' f_Ω is a number not too different from unity. For the Sun-similar model shown in Figs. 4.1 and 4.2, $\Omega = -6.14 \times 10^{48}$ erg and $f_\Omega = 1.36$. This star could survive for $|U|/L = 5.08 \times 10^7$ yr if it could somehow convert its binding energy into light; this is a long time by human standards, but very short compared to the $\approx 5 \times 10^9$ yr age of the Earth⁴.

Further Reading

Kippenhahn, Weigert & Weiss, §§1.1–1.3; Ostlie & Carroll, §§2.2, 10.1; Prialnik, §1.3.

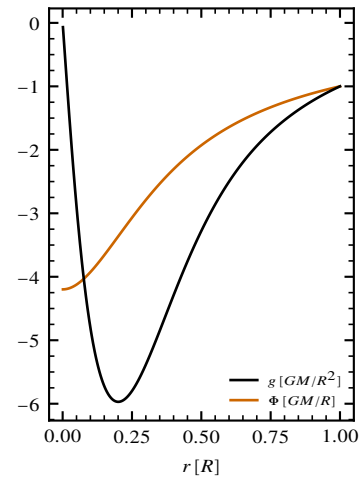


Figure 4.2: The gravity g (in units of its surface magnitude $GM/R^2 = 3.88 \times 10^4 \text{ cm s}^{-2}$) and gravitational potential Φ (in units of its surface magnitude $GM/R = 2.27 \times 10^{15} \text{ cm}^2 \text{s}^{-2}$), plotted as a function of radial coordinate r for the Sun-similar model (see Fig. 4.1).

³ This comes from multiplying the layer's mass by the change in its gravitational potential.

⁴ It's this line of reasoning that first convinced astronomers the Sun can't be powered by gravitational energy alone.

5 Momentum Equation & Hydrostatic Equilibrium

Momentum Equation

Consider a vertically oriented cylindrical volume element with cross-sectional area dA , extending from radial coordinate r_a out to radial coordinate r_b (see Fig. 5.1). Denoting the net radial (upward) force on this element as f , and the net radial momentum of the element as p , Newton's second law¹ applied to the element is

$$f = \frac{dp}{dt} \quad [5.1]$$

The momentum of the element can be evaluated via the integral

$$p = \int_{r_a}^{r_b} \rho v_r dr dA, \quad [5.2]$$

where v_r is the radial velocity. The force on the element comes from a combination of pressure P acting on the top and bottom of the cylinder, and the gravitational acceleration g acting throughout:

$$f = \underbrace{\left[P(r_a) - P(r_b) \right] dA}_{\text{pressure force}} + \underbrace{\int_{r_a}^{r_b} g \rho dr dA}_{\text{gravitational force}}. \quad [5.3]$$

Applying the fundamental theorem of calculus², we can write the pressure term as an integral:

$$f = - \int_{r_a}^{r_b} \frac{\partial P}{\partial r} dr dA + \int_{r_a}^{r_b} g \rho dr dA. \quad [5.4]$$

Substituting this and eqn. [5.2] back into Newton's second law [5.1], and dividing through by dA , we arrive at the *momentum equation* for the element:

$$-\int_{r_a}^{r_b} \left[\frac{\partial P}{\partial r} - \rho g \right] dr = \frac{d}{dt} \int_{r_a}^{r_b} \rho v_r dr \quad [5.5]$$

Hydrostatic Equilibrium

Now let's suppose that the velocity throughout the star vanishes, so the right-hand side of eqn. [5.5] is zero for every possible choice of r_a and r_b . It then follows that the integrand on the left-hand side of the equation must also be zero; that is,

$$\frac{\partial P}{\partial r} = \rho g \quad [5.6]$$

This is the equation of *hydrostatic equilibrium*. It establishes the basic condition that must be satisfied at every point in a star, in order for the stellar material to remain in static (zero velocity) equilibrium. In words, *the outward force due to the pressure gradient must balance the inward force due to gravity*. Fig. 5.2 demonstrates hydrostatic equilibrium in action for the Sun-similar model.

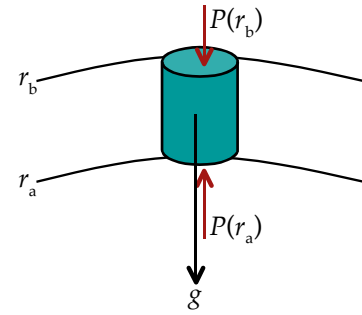


Figure 5.1: A cylindrical volume element with cross sectional area dA , extending between radial coordinates r_a to r_b . This element is acted on by both pressure (P) and gravitational forces (g), as shown.

¹ While the second law is often given as *force is mass times acceleration*, it is more correctly stated as *force is rate-of-change of momentum*.

² This is the theorem that

$$\int_a^b \frac{dy}{dx} dx = y(b) - y(a).$$

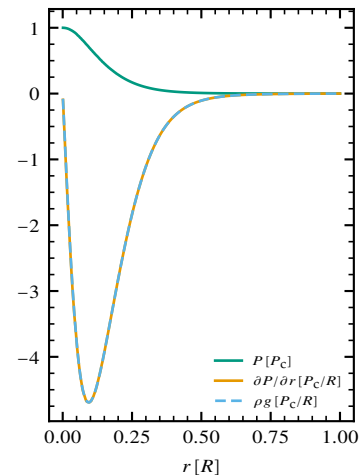


Figure 5.2: The pressure P (in units of its central value $P_c = 2.27 \times 10^{17}$ Pa), its gradient dP/dr and the gravitational force per unit volume ρg (both in units of P_c/R), plotted as a function of radial coordinate r for the Sun-similar model (see Fig. 4.1). The close match between dP/dr and ρg confirms that the model is in hydrostatic equilibrium.

Central Pressure

The hydrostatic equilibrium equation [5.6] provides us with a simple way to place a lower limit on the central pressure P_c of a star. Integrating the equation, we can write³

$$P_s - P_c = \int_0^R g \rho \ dr = - \int_0^M \frac{Gm}{4\pi r^4} \ dm, \quad [5.7]$$

The surface pressure P_s is much smaller than P_c , and can be neglected to yield

$$P_c = \int_0^M \frac{Gm}{4\pi r^4} \ dm > \frac{GM^2}{8\pi R^4}. \quad [5.8]$$

Applying this to the Sun-similar model, we find $P_c > 9 \times 10^{14}$ Ba.

Comparing this inequality against the actual value of P_c (see Fig. 5.2), we can see that the lower limit is pretty loose.

³ In the second equality we have used the mass equation [4.2] to switch to an integral over interior mass m , and likewise expressed the gravity in terms of m and r .

The Dynamical Timescale

Imagine that all pressure forces in a star suddenly vanish. Then, the star will begin to collapse under its own gravitational force. The initial acceleration of the surface layers is

$$g_s = -\frac{GM}{R^2}$$

Assuming that this acceleration remains constant, the time taken for these surface layers to collapse down to the origin is

$$\Delta t = \sqrt{\frac{2R}{|g_s|}} = \sqrt{\frac{2R^3}{GM}}$$

This motivates us to define the *dynamical timescale* of the star as

$$\tau_{\text{dyn}} \equiv \sqrt{\frac{R^3}{GM}}. \quad [5.9]$$

This quantity⁴represents the characteristic timescale over which the star responds to departures from hydrostatic equilibrium. After any perturbation which pushes a star out of hydrostatic equilibrium⁵, the star will (if able) come back into hydrostatic equilibrium over a timescale on the order of τ_{dyn} . Turning this statement around, when considering physical processes that unfold over timescales much longer than τ_{dyn} , we can assume that stars remain in almost-perfect hydrostatic equilibrium.

⁴ For the Sun-similar model, $\tau_{\text{dyn}} \approx 1200$ s.

⁵ For instance, the pressure wave arising from the sudden ignition of a new nuclear fuel source in the core; or, an external process such as the gravitational disturbance produced by a companion star.

Further Reading

Kippenhahn, Weigert & Weiss, §2.1; Ostlie & Carroll, §10.1; Prialnik, §2.3.

6 The Ideal Gas

General Equation of State

The physical properties of stellar material depend on its *thermodynamic state*, as specified by the three *state variables*: density ρ , pressure P and temperature T . Only two of these are needed for a unique specification of the state, because the third can always be calculated using the *equation of state* (EOS) of the material. Most generally, the EOS can be written in the form

$$P = P(\rho, T; \mathcal{C}), \quad [6.1]$$

indicating that the pressure is a function of density, temperature and the composition¹ of the stellar material (here written symbolically as \mathcal{C}).

The Ideal Gas Equation of State

For main-sequence stars in the mass range $0.1 M_{\odot} \lesssim M \lesssim 10 M_{\odot}$, which includes the Sun, the stellar material comes close to fulfilling the criteria for an ideal gas: the size of the gas particles is tiny compared to the average distance between them, collisions between the particles are perfectly elastic, and there are no inter-particle forces. Therefore, the EOS for the material is well approximated by the *ideal gas equation of state*²

$$P = n k_B T \quad [6.2]$$

where k_B is Boltzmann's constant and n the number of particles per unit volume.

At the high temperatures encountered inside stars (see Fig. 6.1), the particles making up the stellar material are a mixture of ions³ and free electrons. We introduce the *mean molecular weight*⁴

$$\mu \equiv \frac{\rho}{n m_H} \quad [6.3]$$

as the average mass per particle (ions *and* free electrons), expressed in units of the hydrogen atomic mass m_H . With this definition, the ideal gas EOS [6.4] can be recast following the general form [6.1], as

$$P = \frac{\rho k_B T}{\mu m_H}. \quad [6.4]$$

Composition & Mean Molecular Weight

The mean molecular weight μ depends both on the composition and the ionization state of the stellar material. Composition is specified by *mass fractions*, which quantify what fraction by mass is composed of a given element. By convention, X denotes the mass fraction of hydrogen, Y the mass fraction of helium, and $Z \equiv 1 - X - Y$ the mass fraction of metals⁵.

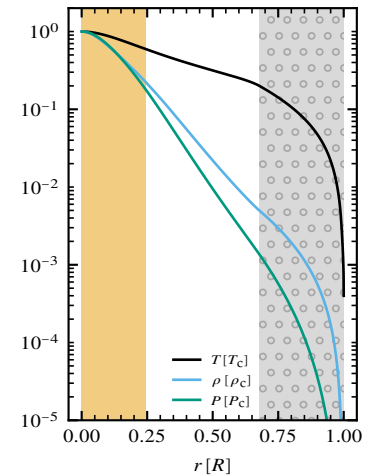


Figure 6.1: The temperature T , density ρ and pressure P (in units of their central values $T_c = 1.57 \times 10^7$ K, $\rho_c = 149$ g cm $^{-3}$, $P_c = 2.27 \times 10^{17}$ Pa), plotted as a function of radial coordinate r for the Sun-similar model (see Fig. 4.1). The orange-shaded region indicates the stellar core where fusion reactions are converting hydrogen into helium; the gray-shaded/dotted region indicates the surface layer where convection is transporting energy outward.

¹ That is, which chemical elements are present, and in what proportions.

² In laboratory contexts this EOS is usually written

$$PV = Nk_B T,$$

where N is the number of particles contained in the volume V . The form given in eqn. [6.2] simply results from setting $n = N/V$.

³ Here, we use 'ions' generically to denote atoms in any ionization state — whether neutral (when the atoms have their full complement of bound electrons), fully ionized (when the atoms have lost their bound electrons into the pool of free electrons), or some partially ionized state.

⁴ In spite of its name, the mean molecular weight has nothing to do with molecules or weight!

⁵ Another weird nomenclature choice: 'metals', to astronomers, are all elements that aren't hydrogen or helium.

The mean molecular weight in the neutral limit, when no elements are ionized, is approximated by

$$\mu \approx \left[X + \frac{Y}{4} + \frac{Z}{12} \right]^{-1} \quad [6.5]$$

The corresponding value in the fully ionized limit, when all elements are completely ionized, is likewise approximated by

$$\mu \approx \left[2X + \frac{3Y}{4} + \frac{Z}{2} \right]^{-1} \quad [6.6]$$

A later handout will discuss the origin of these formulae, and how to evaluate μ for partially ionized samples. Fig. 6.2 shows how these formulae apply to the Sun-similar model.

Isothermal & Adiabatic Changes

Sometimes, we wish to know how stellar material responds to changes in its thermodynamic state. For an *isothermal* change the temperature of the material remains constant; then, the pressure follows the relation

$$P = K_{\text{iso}} \rho, \quad [6.7]$$

where the constant K_{iso} is set by the temperature and composition of the material. Likewise, for an *adiabatic* change there is no heat absorbed or released by the material; then, the pressure follows the relation

$$P = K_{\text{ad}} \rho^\gamma, \quad [6.8]$$

where the constant K_{ad} is set by the *initial* temperature and composition of the material. In both the neutral and fully ionized limits, the exponent γ (which is formally known as the ‘ratio of specific heats’) takes the value $5/3$; however, in the partially ionized case its value is usually closer to 1.

Thermal Energy

In subsequent handouts we’ll need to evaluate the thermal (or internal) energy of the stellar material — that is, the energy associated with the random thermal motions of the particles. For the ideal gas EOS [6.4], the thermal energy per unit mass is

$$u = \frac{1}{\gamma - 1} \frac{k_B T}{\mu m_H}. \quad [6.9]$$

Further Reading

Kippenhahn, Weigert & Weiss, §§4.1–4.2; Ostlie & Carroll, §10.2; Prialnik, §§3.1–3.1.

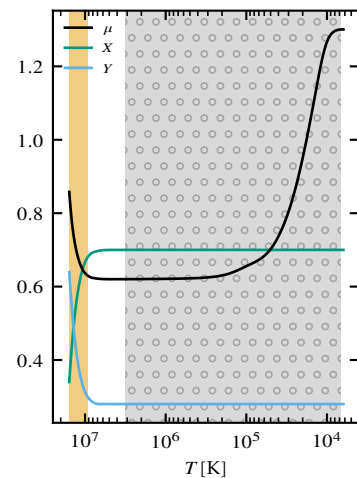


Figure 6.2: The mean molecular weight μ , and hydrogen (X) and helium (Y) mass fractions, for the Sun-similar model (see Fig. 4.1). The shaded regions have the same meaning as in Fig. 6.1. Note that temperature T rather than radial coordinate is used along the abscissa (horizontal axis); this helps highlight the surface layers of the star, which span a narrow range in radius but a large range in temperature. The composition of the model at birth was $X = 0.70$, $Y = 0.28$ and $Z = 0.02$, and these values still apply for $T \lesssim 8 \times 10^6$ K. At higher temperatures, however, the hydrogen is depleted and the helium is enriched; this is the result of the past fusion of hydrogen into helium. With declining temperature below $T \approx 2 \times 10^5$ K, the transition from fully ionized to neutral causes the increase in μ from the value $\mu \approx 0.62$ given by eqn. [6.6], to the value $\mu \approx 1.30$ given by eqn. [6.5].

7 The Virial Theorem

The Virial Theorem

The *virial theorem* (from the Latin word ‘vis’, meaning ‘force’) is a mathematical relationship between the total gravitational and thermal energies of ideal gas stars¹ that are in hydrostatic equilibrium. It’s one of the central concepts of stellar astrophysics, as it allows us to understand how stars respond to the loss (or gain) of energy.

Derivation of the Virial Theorem

To derive the virial theorem, we start with the equation of hydrostatic equilibrium [5.6],

$$\frac{\partial P}{\partial r} = \rho g.$$

Eliminate the gravity g using eqn. [4.4], multiply both sides by $4\pi r^3$, and then integrate with respect to r over the whole star², to yield

$$\int_0^R \frac{\partial P}{\partial r} 4\pi r^3 dr = - \int_0^R \frac{Gm}{r} 4\pi r^2 \rho dr \quad [7.1]$$

Using the mass equation [4.2], we transform the right-hand side into an integral with respect to interior mass m ,

$$-\int_0^R \frac{Gm}{r} 4\pi r^2 \rho dr = -\int_0^M \frac{Gm}{r} dm \equiv \Omega, \quad [7.2]$$

where the second equality follows from the definition [4.7] of the gravitational potential energy. Likewise, we integrate the left-hand side by parts, and then also transform it into an integral with respect to m ,

$$\int_0^R \frac{\partial P}{\partial r} 4\pi r^3 dr = \left[4\pi r^3 P \right]_0^R - 3 \int_0^R 4\pi r^2 P dr = -3 \int_0^M \frac{P}{\rho} dm, \quad [7.3]$$

where the second equality follows from neglecting the (typically-tiny) pressure at the stellar surface $r = R$.

If we now assume the stellar material is described by an ideal-gas equation of state, then from *Handout 6* we have

$$\frac{P}{\rho} = \frac{k_B T}{\mu m_H} = (\gamma - 1)u, \quad [7.4]$$

and so

$$-3 \int_0^M \frac{P}{\rho} dm = -3 \int_0^M (\gamma - 1)u dm = -3(\gamma - 1)U. \quad [7.5]$$

where

$$U \equiv \int_0^M u dm. \quad [7.6]$$

is the total thermal energy of the star. Note that in making the second equality in eqn. [7.5], we’ve assumed that the ratio of specific heats γ remains constant throughout the star, allowing us to bring it out from under the integral sign.³

¹ There also exist versions of the virial theorem as applied to systems of particles bound by gravity (e.g., individual galaxies in a galaxy cluster); these versions have a similar form to the one we derive here, but the derivation process is rather different.

² A common question here is: why $4\pi r^3$? The answer is that this factor transforms the right-hand side of the hydrostatic equilibrium equation into the integrand appearing in the definition of the gravitational potential energy Ω .

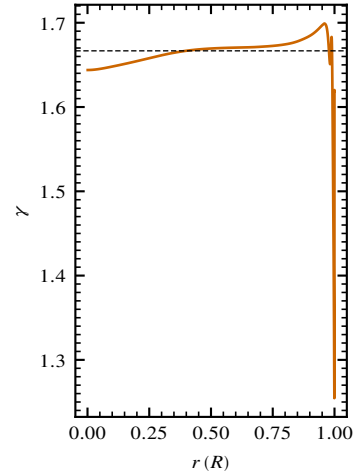


Figure 7.1: The ratio of specific heats γ , plotted as a function of radial coordinate r for the Sun-similar model (see Fig. 4.1). The dotted line shows the fiducial value $\gamma = 5/3 = 1.667$.

³ As Fig. 7.1 shows, for the Sun-similar model γ does vary quite a bit in the surface layers ($r \geq 0.95 R_\odot$); however, these layers account for only a tiny fraction of the star’s mass, and so the error introduced by our assumption is small.

Putting eqns. [7.1], [7.2] and [7.5] together, we arrive at the final result

$$U = -\frac{\Omega}{3(\gamma - 1)}, \quad [7.7]$$

which is the *virial theorem for stars*. In the common case where $\gamma = 5/3$, it reduces to the even-simpler form

$$U = -\frac{\Omega}{2}. \quad [7.8]$$

Understanding the Virial Theorem

The virial theorem [7.7] appears quite straightforward, but don't be deceived by appearances. It's quite unusual for the thermal energy of an object to be tied in any way to its gravitational potential energy⁴. However, the force balance between gravity and pressure, for a star *in hydrostatic equilibrium* and following *an ideal gas law*, creates an inescapable link between thermal and gravitational potential energies: U and Ω are not independent quantities, but tied together by eqn. [7.7]. Fig. 7.2 demonstrates this link in action for a $1 M_\odot$ model.

Virial Theorem and Stellar Energy

The virial theorem leads to a couple of important results when applied to the total stellar energy,

$$E \equiv U + \Omega \quad [7.9]$$

If we combine this with eqn. [7.7], we obtain a pair of complementary expressions for E in terms of U alone and Ω alone:

$$E = -(3\gamma - 4)U, \quad E = \frac{3\gamma - 4}{3\gamma - 3}\Omega. \quad [7.10]$$

For the star to be stably bound E must be negative⁵. Since U is always positive, the left expression here tells us that $\gamma > 4/3$ for stability.

The two expressions [7.10] also indicate a counterintuitive property of stars. Assuming that $\gamma > 4/3$, then a change $\Delta E < 0$ in total energy must be accompanied by a change $\Delta\Omega < 0$ in the gravitational potential energy, but a change $\Delta U > 0$ in the thermal energy. Therefore, as the star loses *total* energy, its *thermal* energy increases — in some sense, it gets hotter. This may seem to violate conservation of energy, but it doesn't.

Further Reading

Kippenhahn, Weigert & Weiss, §3; Prialnik, §2.4.

⁴ Consider, for instance, the objects you see around you as you read this – is there any relationship between their thermal and potential energies? Almost certainly not!

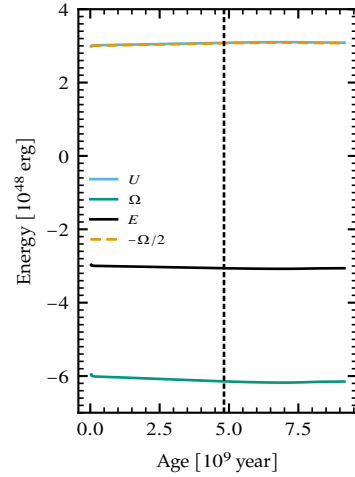


Figure 7.2: The thermal energy U , gravitational potential energy Ω and total energy E , plotted as a function of age for a $1 M_\odot$ MESA model as it evolves through the main-sequence (core hydrogen fusing) phase. The vertical dotted line marks the Sun-similar model. Also plotted is the quantity $-\Omega/2$; by the virial theorem [7.8], this quantity should match U — and clearly, it does.

⁵ If instead $E > 0$ then the star has sufficient energy to spontaneously unbind, dispersing its material to infinity.

8 Pre-Main Sequence Evolution

Star Formation in Brief

Stars form from the gravitational collapse of giant molecular clouds (GMCs) — huge ($\lesssim 100$ pc), massive ($\lesssim 10^5 M_\odot$), cold (≈ 30 K) agglomerations of dust¹ and gas. This collapse ultimately leads to the formation of one or more *protostars* — large, luminous, spherical orbs of gas surrounded by accretion disks. Eventually, the material in a protostar's accretion disk either falls onto the star or is driven away in a jet outflow, leaving behind a *pre-main sequence* (PMS) star.

From this point onward, the star's fate is sealed: its entire future evolution can be predicted based only on its initial mass M and composition \mathcal{C} . This principle of stellar predestination, which is known as the *Vogt-Russell theorem*, means that the distribution of stars in the Hertzsprung-Russell diagram (see Figs. 3.2 and 3.3) comes about wholly due to differences in their mass, composition and time elapsed since birth.

¹ Interstellar dust isn't the same stuff as household dust; it's the generic name given to small ($\lesssim 0.1 \mu\text{m}$) solid grains composed primarily of carbon, silicon and oxygen compounds.

Kelvin-Helmholtz Contraction

PMS stars differ from regular main-sequence stars through their lack of significant internal energy production by nuclear reactions. Nevertheless, because they are hot compared to their surroundings², they lose energy via electromagnetic radiation from their surface layers. Conservation of energy requires that

$$\frac{dE}{dt} = -L, \quad [8.1]$$

where, as usual, E and L are the star's total energy and surface luminosity, respectively. Using eqns. [4.8] and [7.10] we can recast this as

$$\frac{d}{dt} \left(\frac{3\gamma - 4}{3\gamma - 3} f_\Omega \frac{GM^2}{R} \right) = L. \quad [8.2]$$

Let's assume that the ratio of specific heats remains fixed at $\gamma = 5/3$, and that the shape factor f_Ω doesn't change with time. Since the stellar mass is also fixed, we can rearrange this equation to find the rate-of-change of the star's radius:

$$\frac{dR}{dt} = -\frac{2R^2 L}{f_\Omega GM^2}. \quad [8.3]$$

Because dR/dt is negative, the star shrinks as it loses energy — a process known³ as *Kelvin-Helmholtz contraction*. The characteristic timescale for the contraction (neglecting factors of order unity) is

$$\tau_{\text{KH}} \equiv \frac{GM^2}{RL}, \quad [8.4]$$

which is known as the *Kelvin-Helmholtz timescale* of the star. During the Sun's PMS phase, when its radius was $10 R_\odot$, its luminosity was

² Empty space has the same temperature ≈ 2.73 K as the cosmic microwave background (the afterglow of the Big Bang).

³ After the physicists William Thompson (Lord Kelvin) and Hermann von Helmholtz, who first considered the process in the late 19th century.

$\approx 63 L_\odot$, leading to $\tau_{\text{KH}} \approx 50000$ yr. This is small compared to the Sun's main-sequence lifetime $\approx 10^{10}$ yr, indicating that the PMS phase is typically brief.

Pre-Main Sequence Tracks

Although eqn. [8.3] tells us that PMS stars must contract, it doesn't indicate how they move in the Hertzsprung-Russell diagram. Fig. 8.1 reveals what happens, plotting evolutionary tracks for PMS stars with a range of masses. The tracks start in the top-right (low-temperature, high-luminosity, large-radius) of the HR diagram, and evolve toward the *zero-age main sequence* (ZAMS) — the line marking where the main-sequence phase begins. For most of the stars, the evolution occurs in two distinct stages:

- the *Hayashi track*, where energy is transported within the star by convection, and the star evolves vertically downward in the HR diagram (approximately constant T_{eff} , decreasing L and R);
- the *the Henyey track*, where energy is transported within the star primarily by radiation, and the star evolves horizontally leftward in the HR diagram (approximately constant L , increasing T_{eff} , decreasing R).

The switch from the Hayashi track to the Henyey track, corresponding to the transition from convective energy transport to radiative energy transport, occurs toward hotter effective temperatures and higher luminosities as the stellar mass increases. For stars with masses $M \lesssim 0.4 M_\odot$, this switch never takes place and they remain on the Hayashi track all the way to the ZAMS.

A Simple Hayashi Track Model

With $L = 4\pi R^2 \sigma T_{\text{eff}}^4$ (cf. eqn. [2.7]), we can write eqn. [8.3] as

$$\frac{dR}{dt} = -\frac{8\pi R^4 \sigma T_{\text{eff}}^4}{f_\Omega GM^2}. \quad [8.5]$$

To develop a simple model for radius evolution on the Hayashi track, let's assume that T_{eff} does not vary. Then, we solve this equation to find

$$\frac{1}{R^3} = \frac{24\pi \sigma T_{\text{eff}}^4}{f_\Omega GM^2} t, \quad [8.6]$$

where t is the time elapsed since the radius was very large. This equation tells us that R^{-3} should increase linearly with time for a PMS star on the Hayashi track; Fig. 8.2 confirms this approximate behavior for a $1 M_\odot$ model.

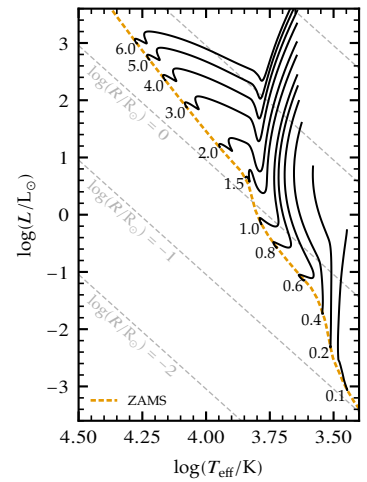


Figure 8.1: Pre-main sequence evolutionary tracks in the Hertzsprung-Russell diagram for a set of solar-composition ($X = 0.7, Y = 0.28, Z = 0.02$) MESA models of differing mass. Each track is labeled at the zero-age main sequence (ZAMS) with the stellar mass in M_\odot . The dashed lines mark contours of constant stellar radius.

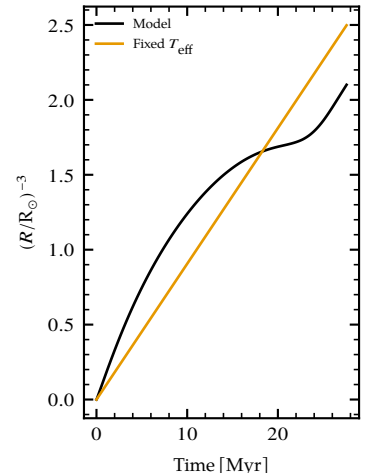


Figure 8.2: The quantity $(R/R_\odot)^{-3}$, plotted as a function of age for a $1 M_\odot$ MESA model during its pre-main sequence phase. The straight line shows the behavior predicted by eqn. [8.6], assuming $f_\Omega = 1.5$ and a fixed effective temperature $T_{\text{eff}} = 5300$ K on the Hayashi track.

Further Reading

Ostlie & Carroll, §12.3; Prialnik, §9.1.

9 The Ignition of Hydrogen

The Approach to the Main Sequence

As a pre-main sequence star approaches the main sequence, the ignition of hydrogen fusion deep within its core slows and eventually halts its Kelvin-Helmholtz contraction. To see why, we re-write the stellar energy conservation equation [8.1] as

$$\frac{dE}{dt} = L_H - L, \quad [9.1]$$

where the new term L_H represents the total energy produced per unit time by hydrogen fusion within the star – its *hydrogen-burning luminosity*. Early during the PMS phase L_H is negligible, and so the star necessarily loses energy with time ($dE/dt < 0$) and contracts. However, near the main sequence L_H ramps up rapidly, reducing the rate of energy loss and slowing the rate of contraction. Eventually, the hydrogen-burning luminosity is large enough to match the surface luminosity L , such that the star is generating energy as fast as it is losing it, and the right-hand side of eqn. [9.1] vanishes. This point formally defines the zero-age main sequence: with no further energy loss from the star, the Kelvin-Helmholtz contraction ceases. Fig. 9.1 demonstrates the approach to the ZAMS for a $1 M_\odot$ model.

Evolution in the Density-Temperature Plane

To understand *why* hydrogen fusion ramps up near the main sequence, let's first note that this fusion involves *thermonuclear* reactions — ones primarily driven by high temperature. Once the central temperature T_c of a star reaches a threshold $T_c \approx 10^7 \text{ K}^1$, the reaction rate rapidly climbs.

A useful way to visualize the approach to this ignition threshold is to plot the path followed by the center of a star in the $\log \rho_c$ – $\log T_c$ plane. Fig. 9.2 shows a number of these paths, for stars in the mass range $0.1 M_\odot \leq M \leq 10 M_\odot$ ². The paths all take a similar form: starting at low central density and temperature, they evolve toward higher density due to Kelvin-Helmholtz contraction, and this evolution is accompanied by a steady increase in temperature. Eventually, T_c reaches the threshold for hydrogen ignition.

The paths followed by the stars are well approximated by parallel straight lines. To understand this behavior, let's estimate the central pressure of a star using eqn. [5.8]:

$$P_c \approx \frac{GM^2}{8\pi R^4}.$$

Using the ideal-gas EOS [6.4], we express the central pressure in terms of the central density and temperature, so that

$$\frac{\rho_c k_B T_c}{\mu m_H} \approx \frac{GM^2}{8\pi R^4}. \quad [9.2]$$

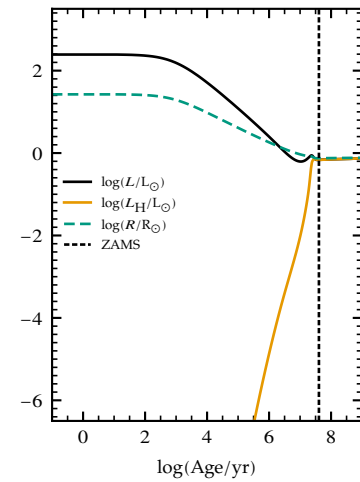


Figure 9.1: The surface luminosity L , hydrogen-burning luminosity L_H and stellar radius R , plotted as a function of age for a $1 M_\odot$ MESA model as it approaches the zero-age main sequence (ZAMS). The age is measured relative to the arbitrary point on pre-main sequence when $L = 250 L_\odot$. The vertical dashed line marks the ZAMS, where L_H first matches L ; note how the radius stops changing from this point onward.

¹ The precise value depends also on the central density ρ_c .

² We will discuss the $0.03 M_\odot$ case separately, below

Then, with the order-of-magnitude estimate $R \approx (M/\rho_c)^{1/3}$, we can eliminate the radius to find a relationship between $\log T_c$ and $\log \rho_c$:

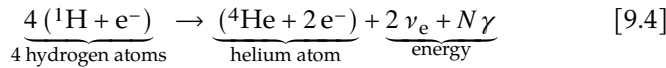
$$\log T_c \approx \frac{1}{3} \log \rho_c + \frac{2}{3} \log M + C \quad [9.3]$$

where C is a constant depending on μ and other quantities. This equation explains the behavior seen in Fig. 9.2: a contracting star follows a straight-line path in the $\log \rho_c$ - $\log T_c$ plane, with slope $d\log T_c / d\log \rho_c \approx 1/3$. More-massive stars follow parallel paths displaced toward high temperatures and/or lower densities.

Let's now briefly consider the $0.03 M_\odot$ path in the figure, which describes the evolution of a *brown dwarf* — a sub-stellar object that never reaches a temperature sufficiently high for hydrogen ignition. As the brown dwarf contracts, the central temperature rises to a maximum $T_c \approx 10^6$ K before decreasing again. Such behavior, which departs from the scaling given in eqn. [9.3], occurs because the electrons become degenerate³ in the core of the brown dwarf. A similar fate is shared by all objects with masses $M \lesssim 0.08 M_\odot$.

A First Look at Hydrogen Fusion

Without going into the specific details, we can write the reaction for the fusion of hydrogen into helium as



where ν_e denotes an electron neutrino, and $N \gamma$ indicates some number of γ -ray photons. There are typically many ways to write this reaction; however, the form given here is special in that not only does it conserve baryon number, lepton number and charge (as all valid versions of the reaction must), but each side is set up to have zero net charge. This makes it possible to group together particles into discrete atoms (indicated here with parentheses), and so the energy release from the reaction, $\Delta \mathcal{E}$, can be expressed in terms of *atomic* masses (see Tab. 9.1):

$$\Delta \mathcal{E} = [4m_{\text{H}} - m_{\text{He}}] c^2 = 0.028\,698 \text{ u} c^2 = 26.73 \text{ MeV.} \quad [9.5]$$

Some fraction⁴ of this energy goes into the two neutrinos, which escape from the star without further interaction, while the remainder (typically denoted Q) is deposited locally as photons.

Further Reading

Kippenhahn, Weigert & Weiss, §§18.1, 18.5.3; Ostlie & Carroll, §10.3; Prialnik, §§4.1, 4.3.

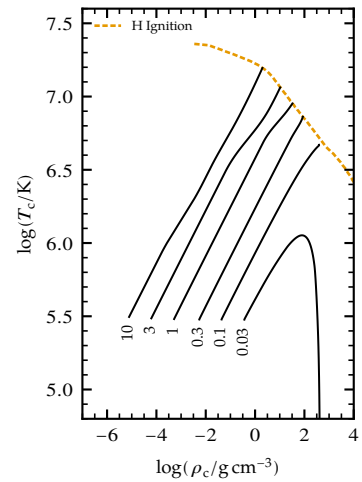


Figure 9.2: Pre-main sequence paths followed in the $\log \rho_c$ - $\log T_c$ plane by a set of solar-composition *MESA* models of differing mass. Each path is labeled at its start with the stellar mass in M_\odot . The dashed line shows the locus in the plane where hydrogen ignites. Note that the $0.03 M_\odot$ model, which doesn't reach the ignition line, corresponds to a brown dwarf rather than a star.

³ Meaning that they depart from the ideal-gas EOS. The departure originates from the Pauli exclusion principle of quantum mechanics, which prohibits two fermions from being packed into the same state. We'll discuss degeneracy in further detail in a later handout.

Isotope	Atomic Mass (u)
${}^1\text{H}$	1.007 825
${}^4\text{He}$	4.002 603
${}^{12}\text{C}$	12.000 000
${}^{14}\text{N}$	14.003 074
${}^{16}\text{O}$	15.994 915

Table 9.1: Atomic masses (in atomic mass units, $1 \text{ u} = 1.6605 \times 10^{-24} \text{ g} = 931.5 \text{ MeV}$) for selected isotopes. From Table D of Audi & Wapstra (1993, *Nucl. Phys. A*, **565**, 1).

⁴ The precise fraction depends on the details of how the hydrogen fusion occurs. We'll discuss these details in a later handout; for now, note that the process is more complicated than four protons magically coming together.

10 Energy Equation & Thermal Equilibrium

Interior Luminosity

In Handout 6 we introduced $m(r)$ as the mass of a star contained within the sphere with radius r . We now define the *interior luminosity* $\ell(r)$ as the total energy flowing through the surface of the same sphere, per unit time interval. By definition, $L \equiv \ell(R)$.

Fig. 10.1 illustrates the interior luminosity for a model of the present-day Sun. Also plotted are the radiative (ℓ_{rad}) and convective (ℓ_{conv}) interior luminosities, representing the energy transported by radiation and convection, respectively; by definition,

$$\ell \equiv \ell_{\text{rad}} + \ell_{\text{conv}}. \quad [10.1]$$

In the figure, we see that ℓ rises rapidly from zero at the center of the star, and by $r \approx 0.35R$ is already very close to its surface value. In the inner parts of the star ($r \lesssim 0.7R$), and also in a thin layer at the stellar surface (the photosphere) there is no convection: $\ell_{\text{conv}} = 0$ and so $\ell_{\text{rad}} = \ell$. Elsewhere, both radiation and convection contribute by varying amounts toward ℓ .

Thermal Equilibrium

The interior luminosity is closely linked to the generation and transport of energy within the star. To establish this link, consider a spherical shell extending from radial coordinate r_a out to radial coordinate r_b . The rate $d\dot{Q}$ that energy is added or removed from this shell is as

$$d\dot{Q} = \underbrace{\left[\ell(r_a) - \ell(r_b) \right]}_{\text{luminosity}} + \underbrace{\int_{r_a}^{r_b} 4\pi r^2 \rho \epsilon_{\text{nuc}} dr}_{\text{nuclear reactions}} - \underbrace{\int_{r_a}^{r_b} 4\pi r^2 \rho \epsilon_{\nu} dr}_{\text{non-nuclear neutrinos}} \quad [10.2]$$

The terms on the right-hand side represent three separate processes (from left-to-right):

- (I) Energy entering the shell through its lower boundary, and leaving through its upper boundary, via the interior luminosity;
- (II) Energy deposited throughout the shell via nuclear reactions. The term ϵ_{nuc} represents the *net*¹ energy release due to nuclear reactions, per unit time interval and mass.
- (III) Energy removed throughout the shell via non-nuclear neutrino production². The term ϵ_{ν} represents the energy lost as non-nuclear neutrinos, per unit time interval and mass.

Applying the fundamental theorem of calculus, the equation can also be expressed as

$$d\dot{Q} = \int_{r_a}^{r_b} \left[-\frac{\partial \ell}{\partial r} + 4\pi r^2 \rho (\epsilon_{\text{nuc}} - \epsilon_{\nu}) \right] dr. \quad [10.3]$$

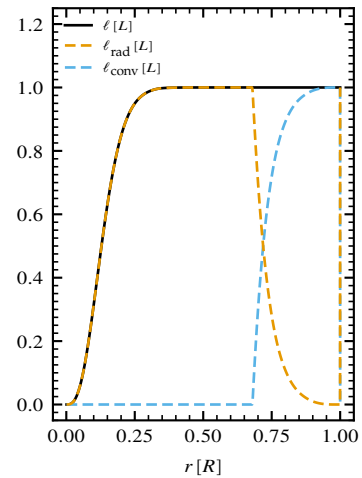


Figure 10.1: The interior luminosity ℓ (in units of its surface value $L = 3.71 \times 10^{33} \text{ erg s}^{-1} = 0.97 L_{\odot}$), plotted as a function of radial coordinate for the Sun-similar model (see Fig. 4.1). Also show are the contributions toward ℓ from the radiative (ℓ_{rad}) and convective (ℓ_{conv}) interior luminosities.

¹ That is, the total energy release minus the energy of any neutrinos generated, since the latter escape from the star with no further interactions.

² An example here is photo-neutrino reactions: $e^- + \gamma \rightarrow e^- + \nu_e + \bar{\nu}_e$.

For stars on the main sequence, $d\dot{Q}$ vanishes for all possible choices of r_a and r_b . This condition is known as *thermal equilibrium*; it arises due to precise balance between the transport, generation and loss of energy. Setting the integrand to zero in the eqn. [10.3], we find the condition for thermal equilibrium:

$$\frac{\partial \ell}{\partial r} = 4\pi r^2 \rho (\epsilon_{\text{nuc}} - \epsilon_\nu). \quad [10.4]$$

Fig. 10.2 demonstrates thermal equilibrium in action for the Sun-similar model.

Departures from Thermal Equilibrium

In certain phases of stellar evolution, thermal equilibrium does not hold. Then, eqn. [10.4] must be replaced by the full *energy equation*

$$\frac{\partial u}{\partial t} = \frac{1}{4\pi r^2 \rho} \left[-\frac{\partial \ell}{\partial r} + 4\pi r^2 \rho (\epsilon_{\text{nuc}} - \epsilon_\nu) \right] + \frac{P}{\rho^2} \frac{\partial \rho}{\partial t}. \quad [10.5]$$

This is a form of the *first law of thermodynamics* (FLOT), which relates the change in thermal energy of a thermodynamic system (the left hand side) to the heat added to the system (the first term on the right hand side), and the work done on the system (the second term).

Fig. 10.3 gives an example of a star that's not in thermal equilibrium. As with all stars on the PMS, the nuclear energy generation in this star is negligible (as are the neutrino losses), and so there's no way it can satisfy eqn. [10.4]. As we already know, the star will undergo Kelvin-Helmholtz contraction ($\partial \rho / \partial t > 0$) and heat up ($\partial u / \partial t > 0$).

The Thermal Timescale

In *Handout 5*, we introduced the dynamical timescale τ_{dyn} as the characteristic timescale over which a star re-establishes hydrostatic equilibrium. A corresponding quantity, the *thermal timescale* τ_{thm} , measures how long it takes for a star to re-establish thermal equilibrium. We already have encountered this timescale — it's the Kelvin-Helmholtz timescale:

$$\tau_{\text{thm}} = \tau_{\text{KH}} \equiv \frac{GM^2}{RL} \quad [10.6]$$

(see eqn. [8.4]).

Further Reading

Kippenhahn, Weigert & Weiss, §4.4; Ostlie & Carroll, §10.3; Prialnik, §2.1.

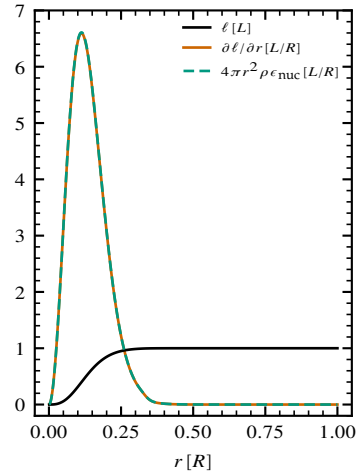


Figure 10.2: The interior luminosity ℓ (in units of L), its gradient $d\ell/dr$ and the nuclear energy release rate per unit radius $4\pi r^2 \rho \epsilon_{\text{nuc}}$ (both in units of L/R), plotted as a function of radial coordinate r for the Sun-similar model (see Fig. 4.1). With ϵ_ν being negligible, the close match between $d\ell/dr$ and $4\pi r^2 \rho \epsilon_{\text{nuc}}$ indicates that the model is in thermal equilibrium.

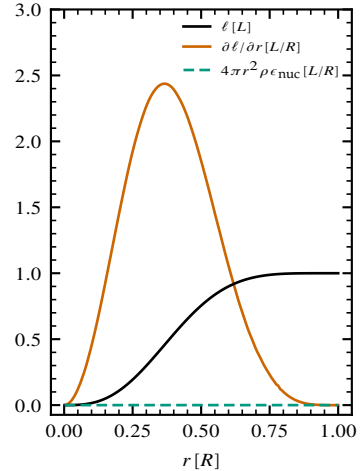


Figure 10.3: As in Fig. 10.2, but for a $1 M_\odot$ model during the pre-main sequence phase when $L = 250 L_\odot$. Because there is no energy generation, $d\ell/dr$ does not match $4\pi r^2 \rho \epsilon_{\text{nuc}}$, and so the star isn't in thermal equilibrium.

11 Opacity & Optical Depth

Radiation & Matter

In this handout, we lay the groundwork for discussing radiative energy transport (*Handout 12*) by reviewing the interaction between photons and matter. This interaction occurs via three processes:

- *emission*, where a new photon is created by extracting energy from the matter;
- *absorption*, where an existing photon is destroyed by depositing energy into the matter;
- *scattering*, where an existing photon's direction (and possibly energy) is altered by the matter, but the photon is not destroyed.

Opacity

Consider a radiation beam passing through matter with a density ρ . Let $\mathcal{P}(l)$ be the probability that a photon in the beam manages to travel a distance l along the beam without interacting with the matter (either by absorption or scattering). The probability that the photon continues on a little further without interacting, to a distance $l + dl$, is given by

$$\mathcal{P}(l + dl) = \mathcal{P}(l) [1 - \kappa \rho dl]. \quad [11.1]$$

Here,

$$\kappa \equiv \frac{\sigma}{\mu m_H} \quad [11.2]$$

is the *opacity* of the matter — the cross section σ for interaction between a photon and a single particle of matter¹, divided by the average mass per particle μm_H (see *Handout 6*).

Rearranging equation [11.1] and taking the limit $l \rightarrow 0$, we obtain

$$\lim_{l \rightarrow 0} \frac{\mathcal{P}(l + dl) - \mathcal{P}(l)}{dl} \equiv \frac{d\mathcal{P}}{dl} = -\kappa \rho \mathcal{P}. \quad [11.3]$$

Solving this differential equation with the initial condition $\mathcal{P}(0) = 1$ gives the result

$$\mathcal{P}(l) = \exp(-\kappa \rho l). \quad [11.4]$$

for the probability that a photon travels at least a distance l without interacting.

Mean Free Path & Optical Depth

The *mean free path* is the average distance a photon travels before it interacts. It is given by²

$$\langle l \rangle = \int_0^\infty l \mathcal{P} \kappa \rho dl = \frac{1}{\kappa \rho}. \quad [11.5]$$

When dealing with stars, it is often useful to express depth below the surface in terms of this mean free path. We therefore introduce the

¹Conceptually, you can think of the particle as blocking out a small area σ of the beam, so that a fraction σ / dA of all photons in a beam with cross-sectional area dA are absorbed or scattered by the particle.

²This expression represents the expectation value of l , weighted by the probability \mathcal{P} that a photon travels a distance l without interacting, times the probability $\kappa \rho dl$ that it *does* interact while traveling the additional distance dl .

optical depth as

$$\tau(r') \equiv \int_{r'}^R \frac{dr}{\langle l \rangle} = \int_{r'}^R \kappa \rho \, dr, \quad [11.6]$$

corresponding to how many mean free paths span the radial coordinate interval from r' to R . Fig. 11.1 shows the optical depth for the Sun-similar model.

Random Walk of Photons

Suppose a photon is emitted at radial coordinate r in the star. Assuming that it interacts with matter only by scattering (so that it is never destroyed), how long will the photon take to escape from the star?

This time can be written generally as

$$t_{\text{esc}} = \frac{\Delta}{c} \quad [11.7]$$

where Δ represents the total distance the photon must travel in order to escape from the star. If the photon could travel in a straight line to the stellar surface, then $\Delta = R - r$ and the escape time is

$$t_{\text{esc}} = \frac{R - r}{c}. \quad [11.8]$$

However, in reality the photon only travels a distance $\langle l \rangle$ before it is scattered, randomizing its direction. Hence, the process by which the photon reaches the stellar surface is a *random walk*³. As an admittedly-crude simplification, if we assume $\langle l \rangle$ remains constant as the photon travels through the star, then the photon can escape by undergoing

$$N \approx \frac{(R - r)^2}{\langle l \rangle^2} \approx \tau^2 \quad [11.9]$$

scatterings. Here, the second equality follows from evaluating the optical depth integral [11.6] for constant $\langle l \rangle$. The total distance traveled by the photon is then $\Delta = N\langle l \rangle \approx (R - r)\tau$, giving an escape time

$$t_{\text{esc}} \approx \frac{(R - r)}{c} \tau. \quad [11.10]$$

This is larger the straight-line escape time [11.8] by a factor τ .

Applying this formalism to the center of the Sun-similar model ($r = 0, R = 0.84 R_\odot, \tau = 3 \times 10^{12}$), we find $N \approx 10^{25}, \Delta \approx 2 \times 10^{23} \text{ cm} \approx 70 \text{ kpc}^4$, and $t_{\text{esc}} \approx 200,000 \text{ yr}$. We therefore see that if nuclear reactions at the star's center suddenly ceased, it would take hundreds of thousands of years for this change to become apparent at its surface.

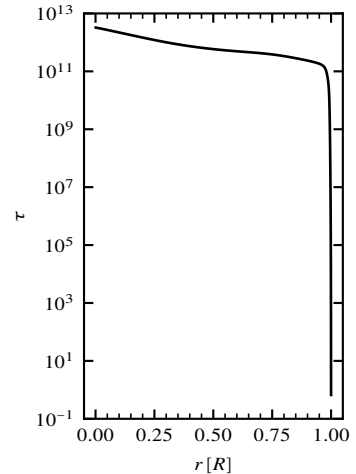


Figure 11.1: The optical depth τ plotted as a function of radial coordinate r for the Sun-similar model (see Fig. 4.1). Observe that τ is zero at the stellar surface, and increases very rapidly as we go deeper into the star, eventually reaching $\approx 3 \times 10^{12}$ at the center.

³A random walk is a stochastic process where the position changes by a fixed amount $\langle l \rangle$ each step, but the direction of the change is random. After a large number of steps N , the average distance from the starting point is $\approx \langle l \rangle \sqrt{N}$.

⁴Larger than the diameter of the Milky Way galaxy!

Further Reading

Kippenhahn, Weigert & Weiss, §5.1.1; Ostlie & Carroll, §9.3; Prialnik, §3.7.

12 Radiative Transport & Opacity Sources

Radiative Diffusion

In stellar interiors, the mean free path of photons (*Handout 11*) is tiny compared to the length scales over which the temperature changes appreciably. This allows us to treat the transport of heat by radiation as a *diffusion* process, with a radiative flux F_{rad} given by

$$F_{\text{rad}} = -k_{\text{rad}} \frac{\partial u_{\text{rad}}}{\partial r}. \quad [12.1]$$

Here, the *radiation energy density* is

$$u_{\text{rad}} = aT^4, \quad [12.2]$$

with $a \equiv 4\sigma/c$ being the *radiation constant*, and the *radiative diffusivity* is

$$k_{\text{rad}} = \frac{1}{3}c\langle l \rangle = \frac{c}{3\kappa\rho}. \quad [12.3]$$

The radiative flux is related to the radiative interior luminosity (see *Handout 10*) via $\ell_{\text{rad}} \equiv 4\pi r^2 F_{\text{rad}}$; putting these expressions together, we arrive at the *radiative diffusion equation*

$$\ell_{\text{rad}} = -\frac{16\pi r^2 acT^3}{3\kappa\rho} \frac{\partial T}{\partial r}. \quad [12.4]$$

Temperature Gradients

Expressed in the form [12.4], the radiative diffusion equation allows us to calculate ℓ_{rad} given dT/dr and other quantities. However, we often need to solve the converse problem: what temperature gradient is required to transport a given radiative luminosity? In such cases, we use the equation of hydrostatic equilibrium [5.6] to rewrite the diffusion equation as

$$\nabla_T = \frac{3}{16\pi acG} \frac{\kappa \ell_{\text{rad}} P}{m T^4}, \quad [12.5]$$

where

$$\nabla_T \equiv \frac{\partial \ln T}{\partial \ln P} = \frac{P}{T} \frac{\partial T}{\partial P} \quad [12.6]$$

(pronounced ‘grad- T ’, or ‘nabla- T ’) is the *dimensionless temperature gradient*, a unit-less quantity that measures how rapidly the temperature rises with respect to pressure as we move deeper into a star.

A related quantity of interest is the *radiative temperature gradient* ∇_{rad} , which quantifies the hypothetical temperature gradient that could transport *all* of the interior luminosity by radiative diffusion alone:

$$\nabla_{\text{rad}} = \frac{3}{16\pi acG} \frac{\kappa \ell P}{m T^4} \quad [12.7]$$

(compare against [12.5]; the only difference is that ℓ rather than ℓ_{rad} appears on the right-hand side). When $\nabla_{\text{rad}} = \nabla_T$, all the interior

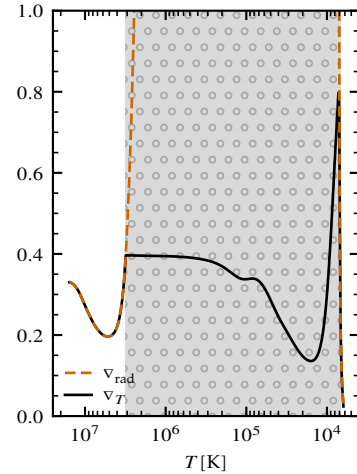


Figure 12.1: The dimensionless temperature gradient ∇_T and radiative temperature gradient ∇_{rad} , plotted as a function of temperature T for the Sun-similar model (see Fig. 4.1; also, see Fig. 6.2 for a reminder of why it’s useful to use T along the abscissa). Energy transport is by radiation alone in regions where $\nabla_{\text{rad}} = \nabla_T$; and by radiation and convection together in regions (gray-shaded/dotted) where $\nabla_{\text{rad}} > \nabla_T$.

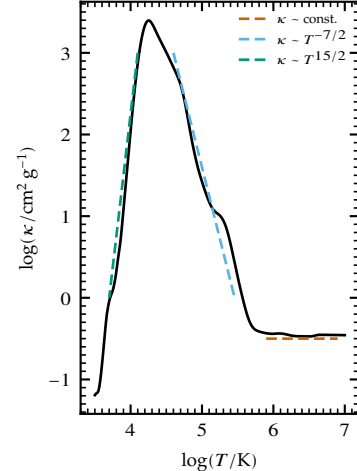


Figure 12.2: The opacity κ log-log plotted as a function of temperature T , for a fixed density $\rho = 10^{-6} \text{ g cm}^{-3}$. The data are taken from MESA for solar composition. The lines show the three regimes discussed in the text: $\kappa \sim \text{const}$. (electron scattering), $\kappa \sim T^{-7/2}$ (bound-free and free-free absorption) and $\kappa \sim T^{15/2}$ (bound-free absorption due to H-minus).

luminosity is transported by radiation (by definition); whereas when $\nabla_{\text{rad}} > \nabla_T$, a fraction $\nabla_T/\nabla_{\text{rad}}$ is transported by radiation, and the remaining fraction $1 - \nabla_T/\nabla_{\text{rad}}$ by convection. Fig. 12.1 plots the two temperature gradients for the Sun-similar model.

Opacity Sources

The opacity κ of stellar material arises from a number of distinct physical processes, known collectively as *opacity sources*:

- (a) *bound-bound absorption*, where a photon is absorbed by a bound electron, exciting the electron to a higher energy level.
- (b) *bound-free absorption*, where a photon is absorbed by a bound electron, freeing the electron from the atom. This is the same process as *ionization*.
- (c) *free-free absorption*, where a photon is absorbed by a free electron in the vicinity of an atom, raising the electron to a higher (and still free) energy state. This is the inverse process of *bremssstrahlung*.
- (d) *electron scattering*, where a photon is scattered by a free electron.

Fig. 12.3 sketches these processes. Because free-free absorption and electron scattering require the presence of free electrons, they are absent in completely neutral material. Conversely, because bound-bound and bound-free absorption require the presence of bound electrons, they are absent in fully ionized material.

The dependence of opacity on temperature and density is generally quite complex. However, in stellar interiors there are three main regimes where a simple power-law relationship applies. At high temperatures ($T \gtrsim 10^6$ K) electron scattering is dominant, and the opacity is virtually independent of T and ρ . At intermediate temperatures ($10^4 \text{ K} \lesssim T \lesssim 10^6$ K) bound-free and free-free absorption by hydrogen, helium and metal atoms and ions are dominant, and the opacity follows *Kramers' law*,

$$\kappa \sim \rho T^{-7/2}. \quad [12.8]$$

Finally, at low temperatures ($T \lesssim 10^4$ K) so-called *H-minus* opacity becomes dominant. This is bound-free absorption by H^- ions — hydrogen atoms with a second, loosely-bound electron. In this special case, the opacity then behaves as

$$\kappa \sim \rho^{1/2} T^{15/2}. \quad [12.9]$$

Fig. 12.2 demonstrates these three regimes for solar-composition material at fixed density.

Further Reading

Kippenhahn, Weigert & Weiss, §§5.1,5.2; Ostlie & Carroll, §10.4; Prialnik, §3.7.

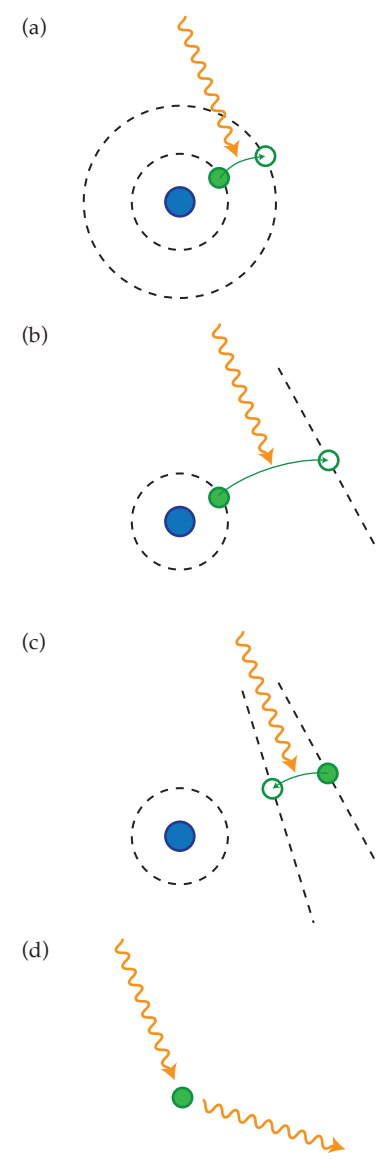


Figure 12.3: Pictorial representation of the four opacity sources in stars: (a) bound-bound absorption, (b) bound-free absorption, (c) free-free absorption, (d) electron scattering. The blue circle indicates the atomic nucleus, the green circle an electron.

13 Convective Stability

Stability of Hydrostatic Equilibrium

Consider a small blob of material with volume ΔV , at rest within a star in hydrostatic equilibrium. Suppose we displace this blob in the vertical (radial) direction by a small amount. The blob will expand or contract to remain in pressure equilibrium with its surroundings, and as a result its density will change. Let's denote this change as $\delta \rho_b$, and the corresponding change in the density of the blob's surroundings (caused by the blob being at a slightly different position in the star) as $\delta \rho_s$ ¹. Generally, $\rho_b \neq \rho_s$, and so there will be a net buoyant force on the blob given² by

$$f_b = (\delta \rho_s - \delta \rho_b)g \Delta V. \quad [13.1]$$

Depending on the sign of f_b , this force will either pull the blob back to its original position, or push it further away. These two outcomes correspond, respectively, to the hydrostatic equilibrium being *stable* or *unstable*³.

In the unstable case, any tiny departures from perfect hydrostatic balance in the star will be amplified over time. However, the final outcome of this instability isn't complete disruption of the star, but a steady-state system of circulatory currents, with low-density upwellings balanced by high-density downwellings; these currents are what we have been calling *convection*. When averaged over many circulation timescales⁴, hydrostatic balance [5.6] still applies.

The Schwarzschild Criterion

To establish the circumstances leading to convection, let's figure out how we can evaluate the $\delta \rho$ terms appearing in eqn. [13.1]. Regarding the density as a function of pressure and temperature, we can write

$$\delta \rho = \left(\frac{\partial \rho}{\partial T} \right)_P \delta T + \left(\frac{\partial \rho}{\partial P} \right)_T \delta P. \quad [13.2]$$

(we've dropped subscripts for the moment, because this expression applies separately to both blob and surroundings). Using the ideal-gas equation of state [6.4] to evaluate the partial derivatives⁵, this becomes

$$\delta \rho = \rho \left(-\frac{\delta T}{T} + \frac{\delta P}{P} \right). \quad [13.3]$$

For the surroundings, the temperature change δT_s can be expressed in terms of the pressure change δP_s via

$$\frac{\delta T_s}{T} = \frac{\partial \ln T}{\partial \ln P} \frac{\delta P_s}{P} = \nabla_T \frac{\delta P_s}{P}, \quad [13.4]$$

where the second equality follows from the definition [12.6] of the dimensionless temperature gradient ∇_T .

For the blob, we have to consider how its state adjusts as it expands or contracts. It's reasonable to assume that this adjustment occurs

¹ Here, we use the subscript 'b' to refer to the blob, and the subscript 's' to refer to the blob's surroundings.

² This equation comes from applying Archimedes principle: *Any object, totally or partially immersed in a fluid, is buoyed up by a force equal to the weight of the fluid displaced by the object.*

³ An analogy here is a solid cone resting on a table, in one of two possible orientations: base at the bottom, and base at the top. Both configurations are in equilibrium with zero net force, but the former is stable and the latter unstable.

⁴ These timescales can vary from minutes to centuries, but are typically much shorter than stellar evolutionary timescales.

⁵ Although our derivation here assumes an ideal gas EOS, the resulting stability criterion (eqn. 13.9) is in fact generally applicable to any EOS.

without any exchange of heat between the blob and its surroundings — that is, an *adiabatic* process. Therefore, we write

$$\frac{\delta T_b}{T} = \nabla_{\text{ad}} \frac{\delta P_b}{P}, \quad [13.5]$$

where

$$\nabla_{\text{ad}} \equiv \left(\frac{\partial \ln T}{\partial \ln P} \right)_{\text{ad}}, \quad [13.6]$$

is the *adiabatic temperature gradient* (the subscript ‘ad’ indicates that the partial derivative here should be evaluated for an adiabatic change). An important distinction between ∇_T and ∇_{ad} is that the former depends on the temperature and pressure stratification — $T(r)$ and $P(r)$ — within the star, whereas the latter depends only on the equation of state. For the specific case of an ideal gas EOS,

$$\nabla_{\text{ad}} = \frac{\gamma - 1}{\gamma}, \quad [13.7]$$

where γ is the usual ratio of specific heats.

Let’s now put everything together. Using eqns. [13.3]–[13.5] to evaluate the density changes in the blob and surroundings, the buoyant force becomes

$$f_b = (\nabla_{\text{ad}} - \nabla_T) \frac{\delta P_s}{P} \rho g \Delta V, \quad [13.8]$$

where we’ve used the fact that $\delta P_b = \delta P_s$ because the blob remains in pressure equilibrium with its surroundings. For stability, the term in parentheses must be positive⁶, leading to the criterion

$$\nabla_T < \nabla_{\text{ad}}. \quad [13.9]$$

This is known as the *Schwarzschild*⁷ criterion for convective stability. At any point in this star, if this inequality holds then the material is stable against small displacements and there will be no convection. Conversely, if this inequality is violated then the material is unstable and convection will spontaneously commence.

Fig. 13.1 plots ∇_T and ∇_{ad} for the Sun-similar model. In the hot core region of the star ($T \gtrsim 3 \times 10^6$ K) the Schwarzschild criterion [13.9] is satisfied and there is no convection. Conversely, in the cooler envelope region ($T \lesssim 3 \times 10^6$ K) the criterion is violated and so convection occurs.

Further Reading

Kippenhahn, Weigert & Weiss, §6.1; Ostlie & Carroll, §10.4; Prialnik, §6.5.

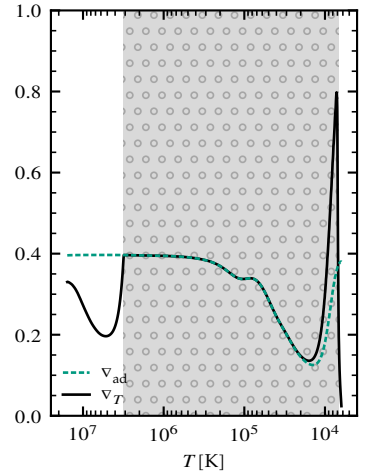


Figure 13.1: The dimensionless temperature gradient ∇_T and adiabatic temperature gradient ∇_{ad} , plotted as a function of temperature T for the Sun-similar model (see Fig. 4.1). The gray-shaded/dotted region highlights the convection zone where the Schwarzschild stability criterion $\nabla_T < \nabla_{\text{ad}}$ is violated.

⁶ To see this, consider an upward displacement of the blob. Because pressure decreases outward in a star in hydrostatic equilibrium, $\delta P_s < 0$. In order for the force to pull the blob back down, $f_b < 0$; therefore, the term in parentheses must be positive.

⁷ After Martin Schwarzschild, one of the pioneers of modern stellar astrophysics. Martin’s father, Karl, gave his name to the radius of a black hole event horizon.

14 Convective Transport

An Algorithm for the Temperature Gradient

At any point within a star, suppose we know the opacity κ , the interior luminosity ℓ and the thermodynamic state (T , P and ρ) of the material. How then do we calculate the temperature gradient ∇_T ? Putting together our knowledge from previous handouts, we can devise a suitable algorithm. First, use eqn. [12.7] to evaluate ∇_{rad} from κ , ℓ and the state, and eqn. [13.6] to evaluate ∇_{ad} from the state. Then, compare these two quantities¹ and set up ∇_T as follows:

$$\nabla_T = \begin{cases} \nabla_{\text{rad}} & \text{if } \nabla_{\text{rad}} < \nabla_{\text{ad}}, \\ \varphi_{\text{conv}} \nabla_{\text{ad}} + (1 - \varphi_{\text{conv}}) \nabla_{\text{rad}} & \text{if } \nabla_{\text{rad}} > \nabla_{\text{ad}}. \end{cases} \quad [14.1]$$

Here, φ_{conv} is a *convective efficiency parameter*, which we'll discuss below.

The upper choice in eqn. [14.1] satisfies the Schwarzschild criterion $\nabla_T < \nabla_{\text{ad}}$, indicating that no convection occurs. Then, radiation transports all of the interior luminosity: $\ell_{\text{rad}} = \ell$ and $\ell_{\text{conv}} = 0$. However, the lower choice violates the Schwarzschild criterion, indicating that convection must be present. Then, the interior luminosities transported by radiation and convection are²

$$\begin{aligned} \ell_{\text{rad}} &= \ell \left(1 - \varphi_{\text{conv}} \frac{\nabla_{\text{rad}} - \nabla_{\text{ad}}}{\nabla_{\text{rad}}} \right), \\ \ell_{\text{conv}} &= \ell \left(\varphi_{\text{conv}} \frac{\nabla_{\text{rad}} - \nabla_{\text{ad}}}{\nabla_{\text{rad}}} \right). \end{aligned} \quad [14.2]$$

Convective Efficiency

The efficiency parameter φ_{conv} is bounded³ to lie in the interval $[0, 1]$. It depends in a complicated fashion on κ , ℓ and other local quantities; to evaluate it, we need to apply so-called *mixing-length theory* (MLT). We won't go into MLT in detail here, but let's consider a couple of limiting cases. In the 'efficient' limit $\varphi_{\text{conv}} \rightarrow 1$, convection transports as much energy as it is able, and the radiative and convective luminosities are

$$\ell_{\text{rad}} \rightarrow \ell \left(\frac{\nabla_{\text{ad}}}{\nabla_{\text{rad}}} \right), \quad \ell_{\text{conv}} \rightarrow \ell \left(\frac{\nabla_{\text{rad}} - \nabla_{\text{ad}}}{\nabla_{\text{rad}}} \right). \quad [14.3]$$

In the opposite 'inefficient' limit $\varphi_{\text{conv}} \rightarrow 0$, convection transports essentially no energy, and the luminosities are

$$\ell_{\text{rad}} \rightarrow \ell, \quad \ell_{\text{conv}} \rightarrow 0. \quad [14.4]$$

In stars, it's typically the case that convection is only inefficient ($\varphi_{\text{conv}} \rightarrow 0$) when it occurs very near the stellar surface; otherwise, it's efficient. Fig. 14.1 demonstrates this by plotting the three gradients (∇_T , ∇_{rad} and ∇_{ad}) for the Sun-similar model. Throughout most of the zone where $\nabla_{\text{rad}} > \nabla_{\text{ad}}$, the high efficiency of convection ($\varphi_{\text{conv}} \approx 1$) means that $\nabla_T \approx \nabla_{\text{ad}}$.

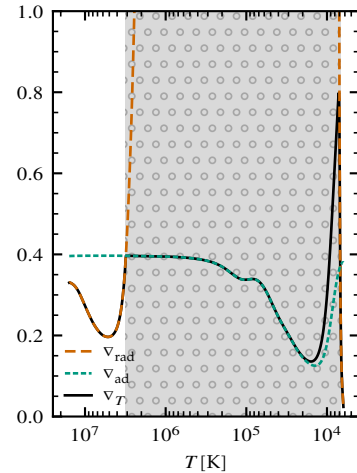


Figure 14.1: The dimensionless (∇_T), radiative (∇_{rad}) and adiabatic (∇_{ad}) temperature gradients, plotted as a function of temperature T for the Sun-similar model (see Fig. 4.1). This brings together the data shown in Figs. 12.1 and 13.1; as before, the gray-shaded/dotted region highlights the convection zone where the Schwarzschild stability criterion $\nabla_T < \nabla_{\text{ad}}$ is violated.

¹ Note that we're comparing ∇_{rad} against ∇_{ad} ; contrast with the Schwarzschild criterion [13.9], which relates ∇_T and ∇_{ad} .

² The upper expression here can be derived from eqns. [12.5], [12.7] and [14.1]; the lower one then follows from the fact that $\ell = \ell_{\text{rad}} + \ell_{\text{conv}}$.

³ This is because $\nabla_{\text{ad}} < \nabla_T < \nabla_{\text{rad}}$ in convection zones; ∇_T must exceed ∇_{ad} in order for the convection to occur; but cannot exceed ∇_{rad} because, otherwise, ℓ_{rad} would be larger than ℓ .

Convection on the Main Sequence

Intermediate-mass ($0.4 M_{\odot} \lesssim M \lesssim 1.4 M_{\odot}$) stars on the main sequence share the same general structural layout as the Sun-similar model (Fig. 14.1), comprising a radiative core and a convective envelope. For higher-mass stars ($M \gtrsim 1.4 M_{\odot}$) on the main sequence the configuration is opposite, comprising a convective core and a radiative envelope (see Fig. 14.2). Whereas, low-mass stars ($M \lesssim 0.4 M_{\odot}$) are convective throughout their entire interior.

To understand these different outcomes, let's examine what can cause ∇_{rad} to rise above the typical threshold $\nabla_{\text{ad}} \approx 2/5$ for the onset of convection. From *Handout 12*, the radiative temperature gradient is

$$\nabla_{\text{rad}} = \frac{3}{16\pi acG} \frac{\kappa \ell P}{m T^4}.$$

The two important terms on the right-hand side are the opacity κ and the interior luminosity-to-mass ratio ℓ/m ; if either of these are large, then so too is ∇_{rad} and convection must occur.

Fig. 14.3 plots these terms for the Sun-similar model, the $5 M_{\odot}$ model, and a $0.2 M_{\odot}$ main-sequence model. Breaking down the data for each mass,

- the solar model shows a large opacity in the envelope (due mainly to bound-free and free-free absorption), explaining why convection occurs there;
- the low-mass model shows a large opacity in the envelope *and* the core (again due to bound-free and free-free absorption), explaining why the entire star is convective;
- the high-mass model shows a relatively small opacity everywhere, compared to the other models, due to its lower density. However, the model has a large luminosity-to-mass ratio in the core, explaining why convection occurs there.

Further Reading

Kippenhahn, Weigert & Weiss, §§7.22.3; Ostlie & Carroll, §10.4; Prialnik, §9.2.

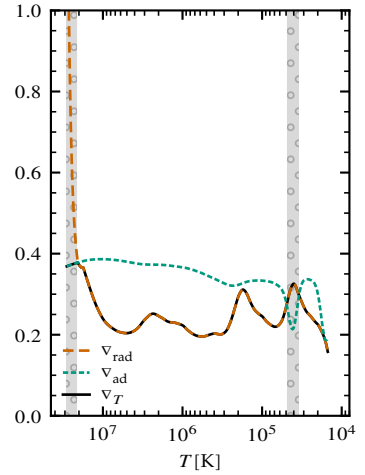


Figure 14.2: As with Fig. 14.1, except that a $5 M_{\odot}$ star with a core hydrogen abundance $X_c \approx 0.34$ is shown (this abundance is chosen to match that of the Sun-similar model). Note the convection zone in the core ($T \gtrsim 2 \times 10^7$ K), but also the thin zone out near the surface ($3.5 \times 10^4 \text{ K} \lesssim T \lesssim 5 \times 10^4$ K); convection in the latter is very inefficient, and so $\nabla_T \approx \nabla_{\text{rad}}$.

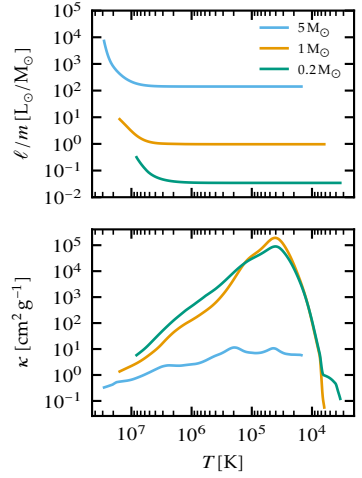


Figure 14.3: The interior mass-to-luminosity ℓ/m (in units of L_{\odot}/M_{\odot}) and the opacity, plotted as a function of temperature for the Sun-similar model (Fig. 14.1), the $5 M_{\odot}$ model (Fig. 14.2), and a $0.2 M_{\odot}$ MESA model with the same core hydrogen abundance $X_c \approx 0.34$ as the first two.

15 The Full Equation of State

General Form

In *Handout 6* we introduced the ideal gas equation of state. This performs well for main-sequence stars in the range $0.1 M_{\odot} \lesssim M \lesssim 10 M_{\odot}$; however, for lower- and higher-mass stars, and for later evolutionary stages, we need a more-sophisticated EOS. We write this as

$$P = P_{\text{ion}} + P_{\text{e}} + P_{\text{rad}} \quad [15.1]$$

where the terms on the right-hand side represent the partial pressures from ions, free electrons and radiation, respectively.

Radiation Pressure

Radiation pressure arises because photons have momentum and therefore can exert a force. Its form is very simple:

$$P_{\text{rad}} = \frac{a T^4}{3}, \quad [15.2]$$

where T is the temperature and a is the usual radiation constant.

Generally, the radiation pressure becomes important in stars with masses $M \gtrsim 10 M_{\odot}$; hence, we have been well justified in neglecting it when dealing with the evolution, e.g., of the Sun.

Ion Pressure

The ions¹ in stellar material can (almost) always be treated like an ideal gas. The partial pressure associated with ions of isotope j is then given by

$$P_{\text{ion}} = n_{\text{ion}}^j k_B T = \frac{\mathcal{X}_j \rho k_B T}{\mathcal{A}_j m_H}. \quad [15.3]$$

Here, n_{ion}^j in the middle expression is the number density of the ions. In the right-hand expression, we re-write this in terms of the overall mass density ρ of the stellar material, together with the mass fraction \mathcal{X}_j and the mass number² \mathcal{A}_j of the isotope. Summing over all isotopes, we obtain the total ion pressure as

$$P_{\text{ion}} = \left[\sum_j \frac{\mathcal{X}_j}{\mathcal{A}_j} \right] \frac{\rho k_B T}{m_H} = \frac{\rho k_B T}{\mu_{\text{ion}} m_H}, \quad [15.4]$$

where μ_{ion} in the right-hand expression denotes the *effective molecular weight associated with ions*, equal to the reciprocal term in brackets in the middle expression.

¹ Remember from *Handout 6* that we are using ‘ions’ generically to denote atoms in any ionization state.

² The number of protons plus neutrons in the nucleus. Note that eqn. [15.3] treats the protons and neutrons as if they have the same mass m_H as the hydrogen atom — not exactly true, but also not too bad of an approximation.

Electron Pressure

Unlike the ions, the free electrons in stellar material don’t always behave like an ideal gas; at (relatively) low temperatures and high densities, quantum mechanical effects cause their EOS to behave in a very non-ideal manner. We’ll look into these effects shortly; but for now let’s assume ideal behavior.

The pressure associated with the free electrons 'belonging'³ to isotope j is

$$P_e^j = \mathcal{N}_j P_{\text{ion}}^j = \frac{\mathcal{N}_j \mathcal{A}_j}{m_H} \rho k_B T; \quad [15.5]$$

here, \mathcal{N}_j is the average number of free electrons per ion of the isotope⁴. Summing over all isotopes, we obtain the total free electron pressure as

$$P_e = \left[\sum_j \frac{\mathcal{N}_j \mathcal{A}_j}{m_H} \right] \frac{\rho k_B T}{m_H} = \frac{\rho k_B T}{\mu_e m_H}, \quad [15.6]$$

where μ_e in the right-hand expression denotes the *effective molecular weight associated with free electrons*, equal to the reciprocal of the term in brackets in the middle expression.

Ions & Electrons Together

When we can neglect radiation pressure, and treat the free electrons as an ideal gas, we can combine equations [15.4] and [15.6] to obtain

$$P = \left[\sum_j \frac{(1 + \mathcal{N}_j) \mathcal{A}_j}{m_H} \right] \frac{\rho k_B T}{m_H} = \frac{\rho k_B T}{\mu m_H} \quad [15.7]$$

where μ in the right-hand expression is the usual mean molecular weight, equal to the reciprocal of the term in brackets in the middle expression. This is the same as the ideal-gas EOS given in eqn. [6.4].

In the neutral limit, where $\mathcal{N}_j \rightarrow 0$ for all j , the mean molecular weight simplifies to

$$\mu = \left[\sum_j \frac{\mathcal{A}_j}{m_H} \right]^{-1} \approx \left[X + \frac{Y}{4} + \frac{Z}{12} \right]^{-1}, \quad [15.8]$$

where the second, approximate equality follows from assuming⁵ $\mathcal{A}_j \approx 12$ for all the metals. This result is the same as eqn. [6.5] — but now we can see where that formula comes from!

In the opposite, fully ionized limit, we have $\mathcal{N}_j \rightarrow \mathcal{Z}_j$, where \mathcal{Z}_j is the atomic number⁶ of isotope j . Then, the mean molecular weight likewise simplifies to

$$\mu = \left[\sum_j \frac{(1 + \mathcal{Z}_j) \mathcal{A}_j}{m_H} \right]^{-1} \approx \left[2X + \frac{3Y}{4} + \frac{Z}{2} \right]^{-1}, \quad [15.9]$$

where the second, approximate equality follows from assuming⁷ $\mathcal{Z}_j + 1 \approx \mathcal{A}_j/2$ for all the metals. This result is the same as eqn. [6.6].

³ In the sense that these electrons originate from ionization of the isotope.

⁴ Another way of saying this is that the average charge per ion is $\mathcal{N}_j e$, where e is the fundamental charge unit.

⁵ Based on the recognition that ^{12}C is usually the most abundant of the light metals.

⁶ The number of protons in the nucleus.

⁷ Based on the fact that the number of neutrons, for metals, is about the same as the number of protons.

Further Reading

Kippenhahn, Weigert & Weiss, §4.2; Ostlie & Carroll, §10.2; Prialnik, §§3.2-3.4.

16 Electron Degeneracy

The Distribution Function

So far we've been describing the properties of stellar material through an equation of state (see, e.g., *Handout 6* and *Handout 15*). However, a more-fundamental representation is in terms of the *momentum distribution function*¹ $f(p)$. Given this function, we can evaluate the number density n and pressure P via the integrals

$$n = \int_0^\infty f(p) \, dp \quad [16.1]$$

and

$$P = \frac{1}{3} \int_0^\infty f(p) p v(p) \, dp, \quad [16.2]$$

where $v(p)$ is the velocity of a particle with momentum p .

¹ The product $f(p) \, dp$ gives the number of particles per unit volume with momenta between p and $p + dp$.

The Free Electron Distribution Function

Because free electrons are *fermions*², they follow the Fermi-Dirac distribution function

$$f_e(p) \equiv \frac{8\pi p^2}{h^3} \frac{1}{\exp[p^2/(2m_e k_B T) - \psi] + 1}, \quad [16.3]$$

where h is Planck's constant, m_e the electron mass, and ψ the *degeneracy parameter*, which quantifies the extent to which the Pauli exclusion principle affects the electrons' behavior. Typically, we use eqn. [16.1] to determine ψ from the electron number density n_e and temperature T ; and then apply eqn. [16.2] to evaluate the electron pressure P_e .

² Particles with half-integer spins, which are subject to the Pauli exclusion principle

Free Electrons in the Classical Limit

In the *classical limit*, where ψ is large and negative, the $+1$ term in the denominator of eqn. [16.3] is negligible, and so the free electron distribution function is well approximated by

$$f_e(p) \approx \frac{8\pi p^2}{h^3} \exp[-p^2/(2m_e k_B T) + \psi]. \quad [16.4]$$

We can solve³ for $\exp[\psi]$ in terms of n_e and T , to obtain

$$\exp[\psi] = \frac{h^3 n_e}{2(2\pi m_e k_B T)^{3/2}}. \quad [16.5]$$

Combining these two equations, we find

$$f_e(p) \approx \frac{4\pi p^2 n_e}{(2\pi m_e k_B T)^{3/2}} \exp[-p^2/(2m_e k_B T)]. \quad [16.6]$$

This can be recognized as a form of the well-known *Maxwell-Boltzmann distribution function* for ideal gasses (see Fig. 16.1). Substituting it into eqn. [16.2], and assuming the electrons are non-relativistic⁴, the

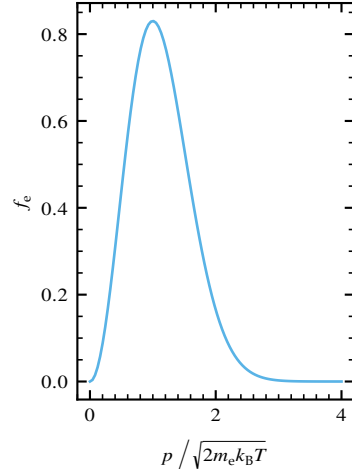


Figure 16.1: The electron momentum distribution function f_e , plotted as a function of scaled momentum $p / \sqrt{2m_e k_B T}$ in the classical (Maxwell-Boltzmann) limit. The vertical scale has been chosen so that the area under the curve is unity.

³ To do this for yourself, first substitute the expression for $f_e(p)$ into the integral [16.1] for n_e .

⁴ So that $v(p) = p/m_e$.

free electron pressure follows as

$$P_e = n_e kT. \quad [16.7]$$

Because $n_e = \rho / (\mu_e m_H)$, this is equivalent to the expression [15.6] for the free electron pressure under the ideal-gas assumption.

Free Electrons in the Completely Degenerate Limit

In the *completely degenerate* limit, where ψ is large and positive, the free electron distribution function is well approximated by

$$f_e(p) \approx \begin{cases} \frac{8\pi p^2}{h^3} & p < p_F, \\ 0 & p > p_F \end{cases} \quad [16.8]$$

(see Fig. 16.2); here, p_F is the *Fermi momentum* defined by

$$\frac{p_F^2}{2m_e k_B T} = \psi. \quad [16.9]$$

Substituting eqn. [16.8] into [16.1], we can solve for p_F in terms of n_e to obtain

$$p_F = \left(\frac{3h^3 n_e}{8\pi} \right)^{1/3}. \quad [16.10]$$

Again assuming that the electrons are non-relativistic, the electron pressure follows from eqns. [16.2] and [16.8] as

$$P_e = \left(\frac{3}{\pi} \right)^{2/3} \frac{h^2}{20m_e} n_e^{5/3} \quad [16.11]$$

This is a significant result: it tells us that the pressure of completely degenerate electrons is independent of temperature, and scales as the $5/3$ power of the density.

Partial Degeneracy

For the intermediate case of *partial degeneracy*⁵, we have to evaluate P_e numerically. However, it's useful to get a sense of what parts of parameter space correspond to the classical and degenerate limits. This can be done by comparing⁶ the *Fermi energy* $\mathcal{E}_F \equiv p_F^2 / 2m_e$ against the *Boltzmann energy* $k_B T$:

$$\mathcal{E}_F \ll k_B T \rightarrow \text{classical}, \quad \mathcal{E}_F \gg k_B T \rightarrow \text{degenerate}. \quad [16.12]$$

Thus, degeneracy is important either when the temperature is low, or the Fermi energy (and therefore the density) is high.

Further Reading

Kippenhahn, Weigert & Weiss, §15; Ostlie & Carroll, §16.3; Prialnik, §3.3.

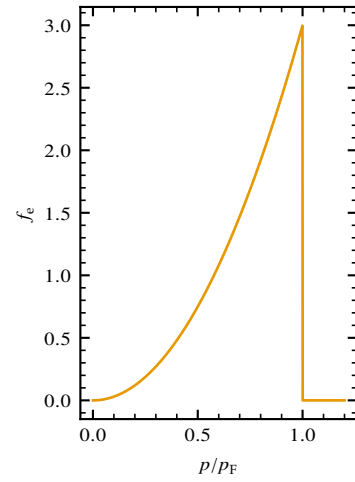


Figure 16.2: The electron momentum distribution function f_e , plotted as a function of scaled momentum p/p_F in the completely degenerate limit. As with Fig. 16.1, the vertical scale has been chosen so that the area under the curve is unity. Note the abrupt cutoff in f_e for momenta $p > p_F$: all of the electrons are packed into the lowest-possible momentum states, subject to the restrictions of the Pauli exclusion principle.

⁵I.e., when $|\psi|$ is not large.

⁶These energies give the order of magnitude of the electron kinetic energy in the completely degenerate (\mathcal{E}_F) and classical ($k_B T$) limits.

17 Ionization

Free Electrons from Ionization

In previous handouts we've discussed the important role that free electrons play in establishing the properties of stellar material; and we've derived expressions¹ for how their pressure P_e depends on the temperature T and their number density n_e . However, we've yet to delve into the physical process responsible for determining n_e : *ionization*.

As stellar material becomes progressively hotter, some of the thermal energy can be used to unbind electrons from atoms, adding them to the pool of free electrons. In this handout we'll explore this process for the simplest case of hydrogen.

Ionization of Hydrogen

The ionization of hydrogen can be written as a chemical process involving three particles:



On the left-hand side, we have a hydrogen atom; and on the right-hand side we have a hydrogen ion² and a free electron. Like all chemical processes, this process is bidirectional; in a sample of stellar material, there are left-to-right reactions (ionizations) taking place at the same time as right-to-left reactions (recombination). Any difference between the rates of these two reactions will cause the relative numbers of atoms, ions and free electrons to change over time; but eventually an equilibrium will be reached where the two reaction rates are balanced.

¹ See eqn. [16.7] for the classical limit, and eqn. [16.11] for the completely degenerate limit.

² Which is, of course, just a bare proton

The Saha Equation for Hydrogen

To determine the relative numbers of hydrogen atoms, ions and free electrons in this equilibrium, we start by writing down the momentum distribution functions³ for the three particle types⁴:

$$\begin{aligned} f_{\text{H},0}(p) &= \frac{8\pi p^2}{h^3} \frac{1}{\exp[p^2/(2m_{\text{H}}k_{\text{B}}T) - \chi_{\text{H}}/(k_{\text{B}}T) - \psi_{\text{H},0}] + 1}, \\ f_{\text{H},1}(p) &= \frac{1}{2} \frac{8\pi p^2}{h^3} \frac{1}{\exp[p^2/(2m_{\text{H}}k_{\text{B}}T) - \psi_{\text{H},1}] + 1}, \\ f_e(p) &= \frac{8\pi p^2}{h^3} \frac{1}{\exp[p^2/(2m_e k_{\text{B}}T) - \psi_{el}] + 1}. \end{aligned} \quad [17.2]$$

In the distribution function for the atoms ($f_{\text{H},0}$), an extra term $-\chi_{\text{H}}/k_{\text{B}}T$ appears in the exponent; χ_{H} is the ionization energy of hydrogen⁵, and this term accounts for the (negative) potential energy of the bound electron. In the distribution function for the ions ($f_{\text{H},1}$), the initial factor of 1/2 is to avoid double counting the spins of the ions

³ See Handout 16 for a reminder of what a momentum distribution function is, and how we can use it.

⁴ Here, the subscripts 'H,0' and 'H,1' refer to the hydrogen atoms and ions, respectively; while 'el' refers to free electrons, as usual.

⁵ $\chi_{\text{H}} = 13.6 \text{ eV} = 2.18 \times 10^{-11} \text{ erg}$.

and free electrons⁶. As a final remark, we've assumed (as a simplifying approximation) that both atoms and ions have a mass m_H .

Let's assume that all particles are in the classical limit, so that the degeneracy parameters are all large and negative. Then, we can neglect the $+1$ term in the denominator of the distribution functions. Integrating over momentum, we arrive at expressions for the number density of each type of particle:

$$\begin{aligned} n_{H,0} &= \frac{2(2\pi m_H k_B T)^{3/2}}{\hbar^3} \exp[\chi_H/(k_B T) + \psi_{H,0}], \\ n_{H,1} &= \frac{(2\pi m_H k_B T)^{3/2}}{\hbar^3} \exp[\psi_{H,1}], \\ n_e &= \frac{2(2\pi m_e k_B T)^{3/2}}{\hbar^3} \exp[\psi_{el}]. \end{aligned} \quad [17.3]$$

As a next step, we take advantage of the fact that the degeneracy parameters are not completely independent; the reaction given in eqn. [17.1] means that⁷

$$\psi_{H,0} = \psi_{H,1} + \psi_{el}. \quad [17.4]$$

This allows us to combine the three equations for the number density into a single equation, known as the *Saha equation*⁸ for hydrogen:

$$\frac{n_{H,1} n_e}{n_{H,0}} = \frac{(2\pi m_e k_B T)^{3/2}}{\hbar^3} \exp[-\chi_H/(k_B T)]. \quad [17.5]$$

To solve this equation, we must augment it with a couple of other relations. Conservation of baryon number and charge require that

$$n_{H,0} + n_{H,1} = n_H, \quad n_{H,1} = n_e, \quad [17.6]$$

respectively, where n_H is the total number density of hydrogen (which we assume is a known quantity).

The Ionization Fraction

Combining the Saha equation [17.5] with the conservation relations following it, we can calculate the *ionization fraction* $x \equiv n_{H,1}/n_H$ of the hydrogen — given T and n_H — by solving the quadratic equation

$$\frac{x^2}{1-x} = \frac{(2\pi m_e k_B T)^{3/2}}{n_H \hbar^3} \exp[-\chi_H/(k_B T)]. \quad [17.7]$$

Fig. 17.1 demonstrates the application of this equation.

Further Reading

Kippenhahn, Weigert & Weiss, §14; Ostlie & Carroll, §8.1; Prialnik, §3.6.

⁶ For each ion and free electron *pair*, there are two spin states: aligned and anti-aligned. The $8\pi p^2/h^3$ factor in the distribution function already includes two spin states, and so either the ion or free electron distribution function must include a factor of $1/2$ to avoid double counting.

⁷ This is a result from statistical mechanics, that arises due to chemical equilibrium: for every hydrogen atom destroyed, there must be a hydrogen ion and free electron created.

⁸ After the Indian physicist Meghnad Saha, who first derived it.

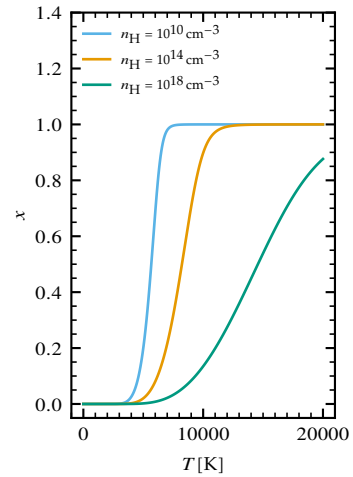


Figure 17.1: The hydrogen ionization fraction x , plotted as a function of temperature T for three choices of the hydrogen number density n_H . For the lower densities, note how almost complete ionization is achieved, even though $\chi_H/k_B T \ll 1$; this is a consequence of the $(2\pi m_e k_B T)^{3/2}/n_H \hbar^3$ term in eqn. [17.7].

18 The Overall Problem

Overview

We're now reaching the end of the journey we began in *Handout 4*: we have enough understanding of stellar physics to assemble a closed¹ set of equations that — if we can solve them — will allow us to theoretically predict the structure and evolution of stars. In this handout, we're going to collect these equations in one place (albeit in slightly different forms than when we introduced them), and discuss the boundary conditions that accompany them.

First, let us define the variables that we'll be using. The independent variables are the interior mass² m and the time t . The dependent variables are the radial coordinate r , interior luminosity ℓ , density ρ and temperature T , plus a set of mass fractions $\{\mathcal{X}_k\}$ for the isotopes comprising the stellar material.

Structure Equations

The *structure equations* are the first-order partial differential equations comprising the mass equation [4.2], the hydrostatic equilibrium equation [5.6], the energy equation [10.5] and an equation governing energy transport. Written with interior mass as the independent variable, these are

$$\frac{\partial r}{\partial m} = \frac{1}{4\pi r^2 \rho}, \quad [18.1]$$

$$\frac{\partial P}{\partial m} = -\frac{Gm}{4\pi r^4}, \quad [18.2]$$

$$\frac{\partial \ell}{\partial m} = \epsilon_{\text{nuc}} - \epsilon_v - \frac{\partial u}{\partial t} + \frac{P}{\rho^2} \frac{\partial \rho}{\partial t}, \quad [18.3]$$

$$\frac{\partial T}{\partial m} = -\frac{GmT}{4\pi r^4 P} \nabla_T. \quad [18.4]$$

The last equation³ must be augmented with a formula for the dimensionless temperature gradient ∇_T . Under the simplifying assumption that convection is everywhere efficient (i.e., $\phi_{\text{conv}} = 1$), eqn. [14.1] becomes

$$\nabla_T = \begin{cases} \nabla_{\text{ad}} & \text{if } \nabla_{\text{rad}} > \nabla_{\text{ad}} \quad (\text{convective}) \\ \nabla_{\text{rad}} & \text{if } \nabla_{\text{rad}} < \nabla_{\text{ad}} \quad (\text{radiative}) \end{cases}, \quad [18.5]$$

where ∇_{rad} is defined in eqn. [12.7], and ∇_{ad} in eqn. [13.6].

Evolution Equations

To establish how a star changes with time, we augment the four structure equations [18.1]–[18.4] with a set of *evolution equations* that describe how the mass fractions $\{\mathcal{X}_k\}$ change with time. For isotope j , the evolution equation⁴ is

¹ In the sense that there are as many equations as unknowns, so we have hope for finding a well-determined solution.

² We use m rather than radial coordinate r , because it serves as a better label of different parts of the star. A piece of stellar material will generally remain at the same m throughout a star's evolution, but its r may change dramatically as the star contracts on the pre-main sequence and expands on the red giant branch.

³ This equation may look unfamiliar, but it is simply a different way of expressing the definition [12.6] of ∇_T .

⁴ In convection zones, we must modify this equation with additional terms accounting for the rapid mixing that occurs; often, however, it is simpler to assume that convection zones remain fully mixed, so that $\partial \mathcal{X}_j / \partial m = 0$ over the extent of the zone for all j .

$$\frac{\partial \mathcal{X}_j}{\partial t} = \frac{\mathcal{A}_j m_H}{\rho} \sum_{k \neq j} (\mathcal{R}_{kj} - \mathcal{R}_{jk}), \quad [18.6]$$

where \mathcal{R}_{kj} represents the rate (in particles per unit volume) at which the isotope is created from another isotope k via nuclear reactions.

Constitutive Relations

The structure and evolution equations are accompanied by a set of *constitutive relations* that specify how the properties of stellar material depend on temperature, density and composition. These are the equation of state [15.1] giving P ; the thermal energy equation⁵ giving u ; the opacity equation⁶ giving κ ; the nuclear reaction equations giving \mathcal{R}_{kj} and ϵ_{nuc} ; and the neutrino loss equation giving ϵ_ν .

Boundary Conditions

To complete our specification of the overall problem, we augment the structure equations [18.1]–[18.4] with four *boundary conditions*. At the center we have, by definition,

$$\left. \begin{array}{l} \ell \rightarrow 0 \\ r \rightarrow 0 \end{array} \right\} \quad \text{as } m \rightarrow 0. \quad [18.7]$$

For the surface boundary conditions, we use a formula⁷ giving the temperature in the stellar atmosphere as a function of optical depth as

$$T^4(\tau) = \frac{3}{4} T_{\text{eff}}^4 \left(\tau + \frac{2}{3} \right). \quad [18.8]$$

To find the pressure, we integrate the equation of hydrostatic equilibrium down from the top of the atmosphere. If we assume that the opacity and gravity remain constant, then

$$P(\tau) = \frac{GM}{R^2 \kappa} \tau. \quad [18.9]$$

Usually, we define the nominal outer boundary to be at the photosphere, where $T = T_{\text{eff}}$; from the temperature equation [18.8], we see this corresponds to $\tau = 2/3$. Therefore, evaluating the pressure at this optical depth, we establish the outer boundary conditions as

$$\left. \begin{array}{l} P \rightarrow \frac{2}{3} \frac{GM}{R^2 \kappa} \\ T \rightarrow T_{\text{eff}} \end{array} \right\} \quad \text{as } m \rightarrow M. \quad [18.10]$$

⁵ An example in the ideal-gas case is eqn. [6.9]. Things become more complicated when radiation pressure and/or electron degeneracy are significant.

⁶ Examples include eqns. [12.8] and [12.9].

⁷ This formula comes from the theory of stellar atmospheres, adopting the *Eddington-gray* approximation. T_{eff} is the usual effective temperature defined by the luminosity L and radius R at the outer boundary (see eqn. [2.7]).

Further Reading

Kippenhahn, Weigert & Weiss, §10.1; Ostlie & Carroll, §10.5.

19 Polytropes

Introducing Polytropes

In the early days of stellar astrophysics, researchers lacked the powerful computers necessary to solve the stellar structure and evolution equations laid out in *Handout 18*. They therefore resorted to simplified models for stars. One of the most useful classes of these models are *polytropes*, where the material obeys the *polytropic relation*

$$P = K \rho^{(1+n)/n} \quad [19.1]$$

for constant K and *polytropic index* n .

This equation looks remarkably similar to equation [6.8]. The polytropic relation is, however, more general: it encompasses all possible power-law relationships between pressure and density.

The Lane-Emden Equation

The structure of polytropes is found by solving the *Lane-Emden equation*¹

$$\frac{1}{z^2} \frac{d}{dz} \left(z^2 \frac{dw}{dz} \right) = -w^n. \quad [19.2]$$

Here, the independent variable z is a re-scaling of the radial coordinate, defined by

$$z = \left[\frac{4\pi G}{K \rho_c^{(1-n)/n} (n+1)} \right]^{1/2} r, \quad [19.3]$$

where ρ_c is the central density of the polytrope. Likewise, the dependent variable w is a re-scaling of the density, defined by

$$w = \left(\frac{\rho}{\rho_c} \right)^{1/n}. \quad [19.4]$$

The Lane-Emden (L-E) equation is solved subject to the boundary conditions

$$\left. \begin{array}{l} w = 1 \\ \frac{dw}{dz} = 0 \end{array} \right\} \text{at } z = 0, \quad w = 0 \text{ at } z = z_s. \quad [19.5]$$

Typically, the surface coordinate z_s isn't known *a priori* — it is determined by integrating the L-E equation from the origin $z = 0$ and finding where w drops to zero. Figure 19.1 plots solutions to the L-E equation, and the corresponding density distributions, for five different choices $n = 0, \dots, 4$ of the polytropic index. Toward larger n , ρ decays more rapidly with radial coordinate, meaning that more of the polytrope's mass is concentrated near the center.

¹ Named after Jonathan Homer Lane and Robert Emden, who formulated it in the late 19th century. It can be derived by combining the polytropic relation [19.1] with the mass equation [4.2], Poisson's equation [4.3] and the hydrostatic equilibrium equation [5.6].

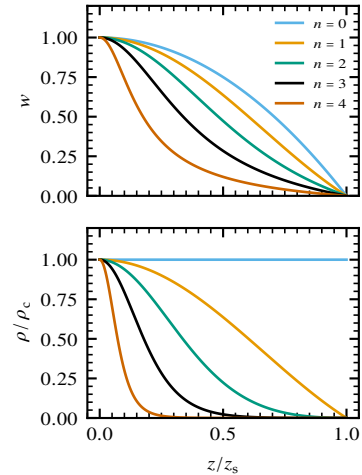


Figure 19.1: The Lane-Emden solution w (upper panel) and normalized density $\rho/\rho_c = w^n$ (lower panel), plotted as a function of normalized radial coordinate $z/z_s = r/R$ for polytropes with five different choices of the index n . Note that the $n = 0$ case has uniform density throughout, because $w^0 = 1$ for all $w > 0$.

Analytic Solutions

The L-E equation admits analytic solutions for three choices of the polytropic index. When $n = 0$, the solution is

$$w(z) = 1 - \frac{z^2}{6} \quad [19.6]$$

and the surface coordinate is $z_s = \sqrt{6} \approx 2.45$. When $n = 1$, the solution is

$$w(z) = \frac{\sin z}{z}, \quad [19.7]$$

and the surface coordinate is $z_s = \pi$. Finally, when $n = 5$, the solution is

$$w(z) = \frac{1}{(1 + z^2/3)^{1/2}} \quad [19.8]$$

and the surface is located at $z_s \rightarrow \infty$.

For other choices of the polytropic index, the L-E equation must be solved numerically, using standard techniques for integrating initial-value problems². Table 19.1 lists the surface coordinate for selected n , combining values from analytic solutions and values obtained numerically.

Mass Distribution

Once the L-E equation has been solved to obtain $w(z)$, the interior mass is calculated using the expression

$$m(r) = 4\pi \rho_c r^3 \left(-\frac{1}{z} \frac{dw}{dz} \right). \quad [19.9]$$

For the special case $r = R$, this becomes

$$M \equiv m(R) = 4\pi \rho_c R^3 \left(-\frac{1}{z} \frac{dw}{dz} \right)_{z=z_s}. \quad [19.10]$$

The parenthetical term on the right-hand side can be evaluated using the data given in table 19.1.

Scaling Relations

The central density of a polytrope can be determined by rearranging equation [19.10] as

$$\rho_c = \frac{1}{4\pi} \frac{M}{R^3} \left(-\frac{1}{z} \frac{dw}{dz} \right)_{z=z_s}^{-1}. \quad [19.11]$$

Hence, we see that polytropes follow the scaling relation $\rho_c \propto M/R^3$, with the constant of proportionality depending only on the polytropic index n .

The central pressure can likewise be found by combining eqns. [19.1], [19.3] and [19.11] to yield

$$P_c = \frac{G}{4\pi(n+1)} \frac{M^2}{R^4} \left(-\frac{dw}{dz} \right)_{z=z_s}^{-2}. \quad [19.12]$$

Thus, polytropes follow the scaling relation $P_c \propto M^2/R^4$, with the constant of proportionality again depending only on n .

Further Reading

Kippenhahn, Weigert & Weiss, §19

n	z_s	$(-z^2 dw/dz)_{z_s}$
0	2.44949	4.89898
1	3.14159	3.14159
2	4.25287	2.41105
3	6.89685	2.01824
4	14.97155	1.79723
5	∞	1.73205

Table 19.1: The surface coordinate z_s , and the (scaled) solution slope dw/dz at the surface, for polytropes of selected indices n .

² An online web tool for solving the L-E equation, based on a second-order finite difference technique, is available at <http://www.astro.wisc.edu/~townsend/static.php?ref=poly-web>.

20 Fully Convective Stars

Overview

In this handout we're going to build a simple model for *fully convective stars* — that is, stars where convection is occurring throughout the entire interior, with only a thin radiative layer¹ at the surface.

Interior Solution

We start by developing a formula for how the temperature T behaves with respect to pressure P throughout the stellar interior. Assuming the convection is efficient, the upper row in eqn. [18.5] gives

$$\frac{\partial \ln T}{\partial \ln P} \equiv \nabla_T = \nabla_{\text{ad}}. \quad [20.1]$$

Let's also assume an ideal-gas equation of state applies with $\gamma = 5/3$, so that $\nabla_{\text{ad}} = 2/5$ (see eqn. [13.7]). Then, we integrate this expression to obtain

$$\ln\left(\frac{T}{T_c}\right) = \frac{2}{5} \ln\left(\frac{P}{P_c}\right). \quad [20.2]$$

To eliminate the central pressure P_c and temperature T_c , we assume the scaling relations² $\rho_c \propto M/R^3$ and $P_c \propto M^2/R^4$; then, $T_c \propto M/R$ via the ideal-gas EOS [6.4], and the interior solution becomes

$$\ln\left(\frac{T}{K}\right) = \frac{2}{5} \ln\left(\frac{P}{B_a}\right) + \frac{1}{5} \ln\left(\frac{M}{M_\odot}\right) + \frac{3}{5} \ln\left(\frac{R}{R_\odot}\right) + C_{\text{int}}, \quad [20.3]$$

where C_{int} is a constant. Fig. 20.1 plots this solution in the $\ln P$ - $\ln T$ plane, for a star with fixed M and three different choices $R_1 < R_2 < R_3$ of radius.

Photosphere Solution

Because stellar atmospheres are radiative, we use a separate $\ln P$ - $\ln T$ relation to describe them, based on the outer boundary conditions from eqn. [18.10]:

$$P_{\text{phot}} = \frac{2}{3} \frac{GM}{R^2 \kappa}, \quad T_{\text{phot}} = T_{\text{eff}}. \quad [20.4]$$

(the subscript ‘phot’ is to remind us that these values refer to the photosphere). Let's assume that the opacity depends on pressure and temperature via the generic power-law relation

$$\kappa = \kappa_0 P_{\text{phot}}^a T_{\text{phot}}^b, \quad [20.5]$$

where κ_0 , a and b are constants. Combining this with the pressure boundary condition leads, after some algebra, to the solution³

$$\ln\left(\frac{T_{\text{phot}}}{K}\right) = -\frac{1+a}{b} \ln\left(\frac{P_{\text{phot}}}{B_a}\right) + \frac{1}{b} \ln\left(\frac{M}{M_\odot}\right) - \frac{2}{b} \ln\left(\frac{R}{R_\odot}\right) + C_{\text{phot}}, \quad [20.6]$$

where C_{phot} is another constant. Fig. 20.1 plots this photosphere solution in the $\ln P$ - $\ln T$ plane for the same radius choices as before.

¹ The surface layers of *any* star — the atmosphere — must always be radiative, because $\nabla_{\text{rad}} \propto P/T^4$ inevitably becomes smaller than ∇_{ad} in these layers.

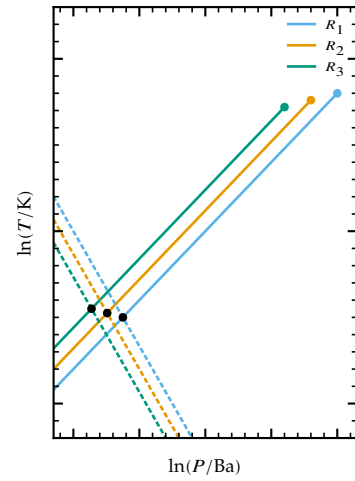


Figure 20.1: Schematic showing interior solutions (solid lines) and photosphere solutions (dotted lines) in the $\ln P$ - $\ln T$ plane, for a fully convective star with three different choices $R_1 < R_2 < R_3$ of the stellar radius. The colored filled circles mark the center of the star, and the black filled circles show where the interior and photosphere solutions intersect. The opacity exponents in eqn. [20.5] have been chosen as $a = 1$, $b = 3$.

² These come from assuming the star can be modeled as a polytrope with fixed index n ; see Handout 19.

³ It's important to recognize that this solution doesn't describe how temperature depends on pressure throughout the atmosphere; rather, it relates the temperature and pressure at a special point, the photosphere.

Matching Solutions

Let's suppose that the convective interior extends all the way up to the photosphere. At that point, the interior solution [20.3] must match the photosphere solution [20.6]. Setting these two equations equal, we obtain the photospheric pressure as

$$\ln\left(\frac{P_{\text{phot}}}{P_{\text{Ba}}}\right) = \frac{(10 - 3b)\ln\left(\frac{R}{R_{\odot}}\right) + (5 - b)\ln\left(\frac{M}{M_{\odot}}\right) + C_P}{5 + 5a + 2b}, \quad [20.7]$$

where C_P is a constant. The photospheric temperature, which by eqn. [20.4] is also the effective temperature, is likewise obtained as

$$\ln\left(\frac{T_{\text{phot}}}{K}\right) = \frac{(3a - 1)\ln\left(\frac{R}{R_{\odot}}\right) + (3 + a)\ln\left(\frac{M}{M_{\odot}}\right) + C_T}{5 + 5a + 2b}, \quad [20.8]$$

where C_T is another constant. Fig. 20.1 marks these photospheric points for the same radius choices as before.

Fully Convective Star in the HR Diagram

For a fully convective star with a given mass, eqn. [20.8] indicates that its effective temperature $T_{\text{eff}} = T_{\text{phot}}$ is a function only of its radius. This means that the star must lie on a well-defined line in the Hertzsprung-Russell diagram. To determine this line, we use the eqn. [2.7] to eliminate $\ln R$ in favor of $\ln L$ and $\ln T_{\text{eff}}$, yielding

$$\ln\left(\frac{L}{L_{\odot}}\right) = \frac{(6 + 22a + 4b)\ln\left(\frac{T_{\text{eff}}}{K}\right) - (6 + 2a)\ln\left(\frac{M}{M_{\odot}}\right) + C_L}{3a - 1}, \quad [20.9]$$

where C_L is a constant. The slope of this line is

$$\frac{d\log L}{d\log T_{\text{eff}}} = \frac{d\ln L}{d\ln T_{\text{eff}}} = \frac{6 + 22a + 4b}{3a - 1}. \quad [20.10]$$

In cool stars ($T_{\text{eff}} \lesssim 10^4$ K), H^- opacity dominates throughout much of the star, leading to an empirical scaling $a \approx 1$ and $b \approx 3$ and a steep slope $d\log L / d\log T_{\text{eff}} \approx 20$. So, fully convective stars lie on almost vertical lines in the HR diagram.

We've already encountered these vertical lines for stars during their pre-main sequence evolution: they are Hayashi tracks (see Fig. 20.2). Initially, all PMS stars are fully convective; as they undergo Kelvin-Helmholtz contraction they move vertically down in the HR diagram. Eventually, for stars with $M \gtrsim 0.4 M_{\odot}$, a radiative region develops in the interior; then, the star pulls off its Hayashi track and evolves blueward along a Henyey track.

Further Reading

Kippenhahn, Weigert & Weiss, §24; Prialnik, §9.1.

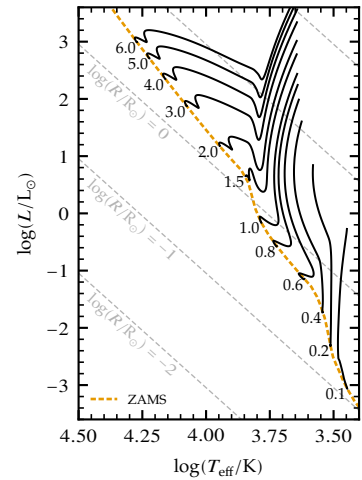


Figure 20.2: Evolutionary tracks in the Hertzsprung-Russell diagram for stars in the pre-main sequence phase, calculated using *MESA*. Each track is labeled at the zero-age main sequence (ZAMS) with the stellar mass in M_{\odot} . With increasing mass, the vertical Hayashi tracks are displaced toward hotter effective temperatures — exactly as predicted by eqn. [20.9]. Taken from Fig. 8.1.

21 The Main Sequence

Radiative Stars

In Handout 20 we showed that fully convective ideal-gas stars lie on almost vertical lines¹ in the Hertzsprung-Russell diagram. What about the opposite case, of fully radiative ideal-gas stars? To build a model for such cases, let's start by adopting the same scaling relations for the central density, pressure and temperature as we did for convective stars: $\rho_c \propto M/R^3$, $P_c \propto M^2/R^4$ and $T_c \propto M/R$. Then, the radiative diffusion equation [12.4] gives us a further scaling relation for the luminosity,²

$$L \propto \frac{RT_c^4}{\kappa \rho_c}. \quad [21.1]$$

For simplicity, we'll assume that the opacity κ doesn't depend on temperature or density, and therefore drop it from subsequent expressions. Then, combining these four scaling relations, we arrive at the *mass-luminosity relation for radiative stars*:

$$L \propto M^3, \quad [21.2]$$

with no dependence on radius. This result tells us that a radiative star of a given mass lies (approximately) along a horizontal (constant- L) line in the HR diagram. It provides us with a narrative for understanding Henyey tracks: pre-main sequence stars moving along these tracks are *mostly* radiative in their interiors, and so the tracks are nearly horizontal in the HR diagram (see Fig. 21.1).

Main-Sequence Stars

As well as describing Henyey tracks, the mass-luminosity relation [21.2] does a reasonable job of reproducing the behavior of main-sequence stars; this is because main sequence stars with masses $M \gtrsim 0.4 M_\odot$ are mostly radiative. In fact, as Fig. 21.2 shows, the scaling is more like $L \propto M^{3.5}$ (due largely to the dependence of opacity on temperature and density, which we neglected in our analysis); but we're not off by much.

With a little further effort, we can derive a similar scaling relation for the radius of main-sequence stars. We begin by writing the thermal equilibrium condition [10.4] as³

$$\frac{L}{R} \propto R^2 \rho_c \epsilon_{\text{nuc},c}. \quad [21.3]$$

Let's further assume a power-law dependence of $\epsilon_{\text{nuc},c}$ on temperature and density,

$$\epsilon_{\text{nuc},c} = \epsilon_{\text{nuc},0} \rho_c^\alpha T_c^\beta, \quad [21.4]$$

where $\epsilon_{\text{nuc},0}$, α and β are constants. Then, combining this with the other scaling relations and solving for the radius, we obtain

$$R \propto M^{\frac{\alpha+\beta-3}{3\alpha+\beta}}. \quad [21.5]$$

¹ Hayashi tracks, of course!

² To derive this expression from eqn. [12.4], on the left-hand side approximate ℓ_{rad} with the surface luminosity L ; and on the right-hand side, approximate ρ with ρ_c , r with R , T with T_c , and $\partial T/\partial r$ with $-T_c/R$.

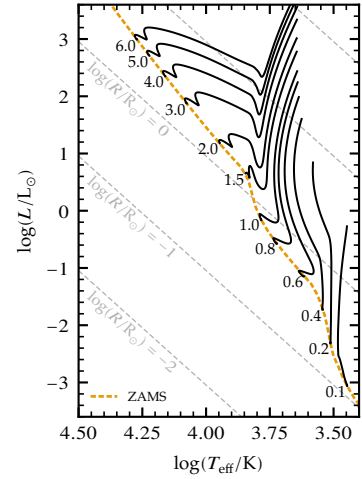


Figure 21.1: Evolutionary tracks in the Hertzsprung-Russell diagram for stars in the pre-main sequence phase, calculated using *MESA*. Each track is labeled at the zero-age main sequence (ZAMS) with the stellar mass in M_\odot . With increasing mass, the (nearly) horizontal Henyey tracks are displaced toward higher luminosities, as predicted by eqn. [21.2]. Taken from Fig. 8.1.

³ To derive this expression from eqn. [10.4], on the left-hand side approximate $\partial \ell_{\text{rad}}/\partial r$ with L/R ; and on the right-hand side, approximate r with R , ρ with ρ_c , ϵ_{nuc} with its central value $\epsilon_{\text{nuc},c}$, and neglect ϵ_ν (because neutrino losses on the main sequence are always small).

For hydrogen burning, $\alpha = 1$ while β varies between about 5 (for burning via the pp chain) and 17 (for burning by the CNO cycle)⁴. Taking an intermediate value $\beta \approx 11$ leads to the *mass-radius relation for main-sequence stars*:

$$R \propto M^{0.64} \quad [21.6]$$

In reality the exponent is close to 0.72 (see Fig. 21.2), so again our very simple analysis isn't off by too much.

We should at this point recognize an important difference between the mass-luminosity relation [21.2] and the mass-radius relation [21.6]. The former was derived with no reference to nuclear reactions, and indeed it holds for pre-main sequence stars on the Henyey track, in which there are *no* nuclear reactions. By contrast, the latter depends sensitively on which nuclear reactions are taking place, as evidenced by the exponents α and β appearing in eqn. [21.5].

Main-Sequence Lifetimes

Armed with the mass-luminosity relation [21.2], we can estimate how long stars will remain on the main sequence burning hydrogen. Suppose a star converts some fraction f of its mass from hydrogen into helium; and suppose the energy released by this conversion, per unit mass, is e . Then, if τ_{MS} denotes the star's main-sequence lifetime,

$$fM e = L \tau_{\text{MS}}, \quad [21.7]$$

where the left-hand side represents the total nuclear energy released during the main-sequence phase, and the right-hand side represents the total energy radiated into space. Solving for the lifetime,

$$\tau_{\text{MS}} = \frac{fM e}{L} \propto M^{-2}, \quad [21.8]$$

where the second equality follows from the mass-luminosity relation [21.2]. Therefore, we see that high-mass stars have much shorter lifetimes than low-mass stars⁵. This explains an important property of HR diagrams of star clusters⁶: there exists a point on the main sequence (the *turn-off*) above which stars are not observed because they have already completed their hydrogen burning. For progressively older clusters, the turn-off appears at progressively lower luminosities; and by measuring the position of the turn-off, we can in principle determine the age of the cluster.

Further Reading

Kippenhahn, Weigert & Weiss, §22.1; Ostlie & Carroll, §10.6.

⁴ These two reaction pathways for hydrogen burning are discussed in a later handout.

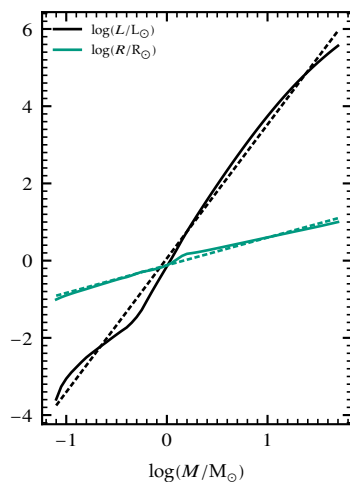


Figure 21.2: The logarithm of the luminosity L and radius R , plotted as a function of the logarithm of the mass M for MESA models of ZAMS stars. The dotted lines are linear best fits to the data, and have slopes $d\log L / d\log M \approx 3.5$ and $d\log R / d\log M \approx 0.72$.

⁵ Even though they have more hydrogen fuel to burn, they burn it so much faster that they run out sooner.

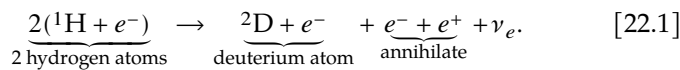
⁶ Remember that the stars in a cluster are co-eval: they were all born at (approximately) the same time, and hence have the same age. Of course, this doesn't mean that they all evolve at the same rate.

22 Hydrogen Burning Reactions

The Proton-Proton Chain

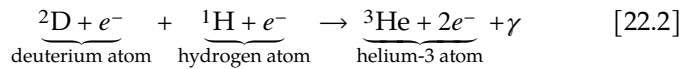
In *Handout 9* we wrote down a reaction for the fusion of four hydrogen nuclei into one helium nucleus (see eqn. [9.4]). In this reaction there are a sequence of intermediate steps that we're now going to examine in detail.

The simplest sequence, known as the *proton-proton (pp) chain*, begins with the interaction of a proton with another proton. During this interaction, one of the protons transforms into a neutron¹, forming a deuteron (deuterium nucleus) and releasing a positron and an electron neutrino. In balanced form, with electrons added to each side to ensure zero net charge,

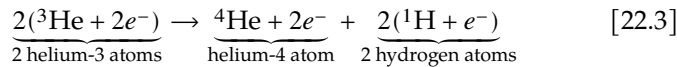


The net energy release, in the form of the neutrino, two γ rays² and the kinetic energy of the other particles, is given by the mass-energy difference between a deuterium atom and two hydrogen atoms: $\Delta E = (2m_H - m_D)c^2 = 1.44 \text{ MeV}$ (see Table 22.1 for atomic mass data).

The next step in the pp chain is a reaction between the deuteron and another proton. Again in balanced form,

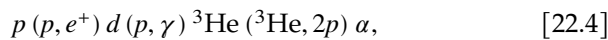


The energy release from this reaction is $\Delta E = 5.49 \text{ MeV}$. The final step involves two ^3He nuclei combining to form a ^4He nucleus and two protons:



The energy release from this reaction is $\Delta E = 12.86 \text{ MeV}$. Taken together, these three reactions — with the first two occurring twice, to provide the two ^3He nuclei required for the third — release a total energy of $\Delta E = 26.72 \text{ MeV}$. This energy is released in the form of two neutrinos, six γ rays and kinetic energy.

The above description of pp-chain chain reactions is complete, but rather verbose. An abbreviated notation writes a reaction between a target nucleus 'a' and an incoming particle 'b', to produce a final nucleus 'd' and an outgoing particle 'c', as $a(b, c)d$. Written in this form, the pp chain becomes



where p , d and α are shorthands for a proton, a deuteron and an α particle (a ^4He nucleus), respectively. Note that neutrinos are not explicitly listed here, but are implied by lepton number conservation.

¹ This transformation is a highly unlikely process, because first the two protons must overcome their mutual Coulomb repulsion to get close enough for nuclear forces to become important; and then a weak interaction must take place. On average, proton at the center of a star like the Sun must wait billions of years before a successful transformation occurs.

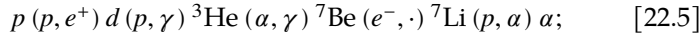
² These γ rays are released when the positron annihilates with the electron.

Isotope	Atomic Mass (u)
^1H	1.007 825
^2D	2.014 102
^3He	3.016 029
^4He	4.002 603
^7Li	7.016 004
^7Be	7.016 929
^8Be	8.005 305
^8B	8.024 607
^{12}C	12.000 000
^{13}C	13.003 355
^{13}N	13.005 739
^{14}N	14.003 074
^{15}N	15.000 109
^{15}O	15.003 066
^{16}O	15.994 915

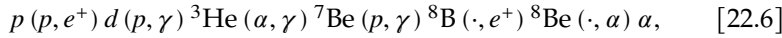
Table 22.1: Atomic masses (in atomic mass units, $1 \text{ u} = 1.6605 \times 10^{-24} \text{ g} = 931.5 \text{ MeV}/c^2$) for selected isotopes. From Table D of Audi & Wapstra (1993, *Nucl. Phys. A.*, **565**, 1).

Other pp Chains

The pp chain described above is one possible variant of the reaction sequence that begins with the proton-proton reaction [22.1]. It is known as pp-I, to distinguish it from other possibilities. The pp-II chain is



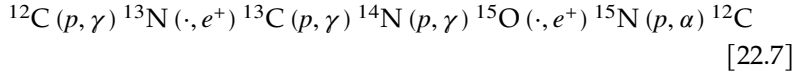
note the electron capture reaction (e^-, \cdot), with the dot indicating that there is no outgoing particle (apart from a neutrino). The pp-III chain is



and involves a couple of spontaneous decays, marked by the dot in front of the comma to indicate that they do not require an incoming particle. Like pp-I, both pp-II and pp-III release 26.72 MeV per ${}^4\text{He}$ nucleus produced; however, the distribution of this energy between neutrinos, γ rays and kinetic energy differs between the three chains.

The CNO Cycle

While the pp chains are responsible for hydrogen burning in the Sun, stars with hotter cores burn hydrogen by a different path: the CNO (*carbon-nitrogen-oxygen*) cycle. In shorthand form, the cycle is



Importantly, the C, N and O involved in this reaction are *catalytic*³. As with the pp chains, the total energy release is 26.72 MeV per ${}^4\text{He}$ nucleus produced.

The pp-CNO Switchover

The switchover between pp chains and the CNO cycle occurs because the latter is far more temperature sensitive than the former⁴. The energy generation rates for the two reaction networks follow the approximate scalings

$$\epsilon_{\text{nuc,pp}} \approx \epsilon_{0,pp} \rho T^{4.9}, \quad \epsilon_{\text{nuc,CNO}} \approx \epsilon_{0,CNO} \rho T^{16}, \quad [22.8]$$

respectively, where $\epsilon_{0,pp}$ and $\epsilon_{0,CNO}$ are constants (see Fig. [22.1]). Because $\epsilon_{0,pp} \gg \epsilon_{0,CNO}$, the pp chains dominate at temperatures $\log(T/\text{K}) \lesssim 7.3$; but at higher temperatures, as encountered in more-massive stars ($M \gtrsim 1.4 M_\odot$) the CNO cycle is more important.

Further Reading

Kippenhahn, Weigert & Weiss, §18.5.1; Ostlie & Carroll, §10.3; Prialnik, §§4.3,4.4.

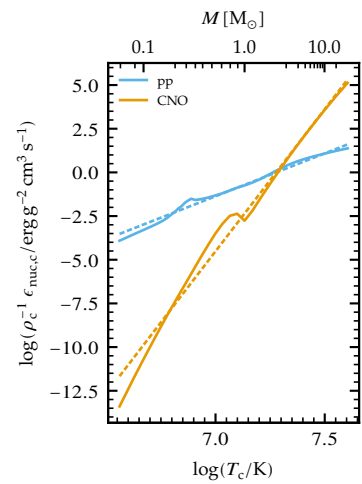


Figure 22.1: The logarithm of the central nuclear energy generation rate $\epsilon_{\text{nuc},c}$ divided by the central density ρ_c , plotted as a function of the logarithm of the central temperature T_c for MESA models of ZAMS stars spanning the mass range $0.1 M_\odot \leq M \leq 10 M_\odot$ (indicated along the top axis). Separate curves are shown for energy generation by the pp chains and the CNO cycle. The dotted lines are linear best fits to the data, and have slopes $d\log(\rho_c^{-1} \epsilon_{\text{nuc},c}) / d\log T_c \approx 4.9$ (pp) and $d\log(\rho_c^{-1} \epsilon_{\text{nuc},c}) / d\log T_c \approx 16$ (CNO).

³I.e., they facilitate the reaction, but are not consumed.

⁴Ultimately, this is a consequence of the steeper Coulomb barrier of heavier nuclei such as carbon-12, compared to a proton.

23 The Red Giant Branch

Evolution onto the Red Giant Branch

When a star runs out of hydrogen at its center, its time on the main sequence has reached an end, and it embarks on a series of dramatic changes. For low- and intermediate-mass stars like the Sun, hydrogen burning continues in a shell around the core (now composed predominantly of helium), and the star evolves to the right in the Hertzsprung-Russell diagram. This phase is known as the *sub giant branch* (see Fig. 23.1).

Eventually, the star becomes mostly convective and it transitions to more-vertical evolution in the HR diagram. This phase is known as the *red giant branch (RGB)*, because the star becomes very large ($R \gtrsim 100 R_{\odot}$) and appears red due to its low effective temperature.

Core-Envelope Dichotomy on the RGB

A characteristic property of stars on the RGB is the division of the star into dichotomous regions:

- A high-density *radiative core* composed primarily of helium (plus a small amount of metals). The core can encompass a significant fraction of the star's mass, but spans only a small fraction of the star's radius.
- A surrounding low-density *convective envelope* composed of hydrogen-rich material. The envelope contains the remainder of the star's mass, and spans almost all of the star's radius.

Fig. 23.2 illustrates the marked contrast between the core and the envelope, for a $1 M_{\odot}$ MESA model at $R = 10 R_{\odot}$ on the RGB. Note how the density at the top of the core is 5 orders of magnitude larger than the density at the bottom of the envelope. For this model, the core contains around 25% of the star's mass, but spans only $\sim 0.3\%$ of its radius. The envelope encompasses almost all of the remaining mass and radius. Because 95% by radius of the star is convective, its evolution in the HR diagram (Fig. 23.1) closely resembles a Hayashi track (see Handout 8 and Handout 20).

Shell Energy Generation

The *hydrogen burning shell* sits in the narrow region of rapidly varying density between the core and the envelope. Within the shell, the strong energy generation (primarily by the CNO cycle) results in a very steep luminosity gradient (see Fig. 23.3). Interior and exterior to the shell, however, the absence of any significant energy generation leads to a flat luminosity gradient there. Hence, the interior luminosity shows a characteristic step-like profile, as seen in the lower panel of Fig. 23.3, with the step coinciding with the burning shell.

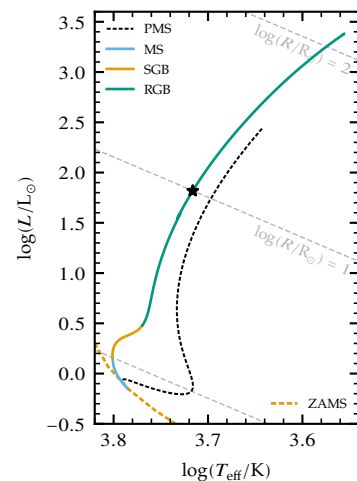


Figure 23.1: Evolutionary track in the Hertzsprung-Russell diagram for a $1 M_{\odot}$ MESA model, spanning the pre-main sequence (PMS), main sequence (MS), sub giant branch (SGB), and red giant branch (RGB) phases. The asterisk marks the case plotted in Figs. 23.2 and 23.3.

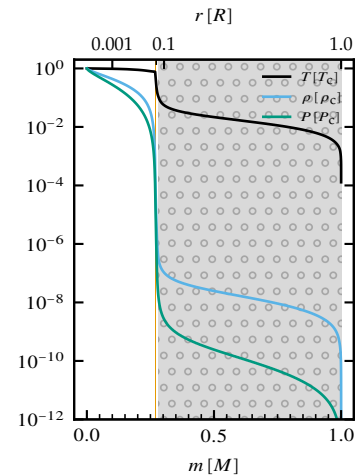


Figure 23.2: The temperature T , density ρ and pressure P (in units of their central values $T_c = 4.04 \times 10^7 \text{ K}$, $\rho_c = 2.25 \times 10^5 \text{ g cm}^{-3}$, $P_c = 2.62 \times 10^{21} \text{ Ba}$), plotted as a function of interior mass m for the $1 M_{\odot}$ model at $R = 10 R_{\odot}$ (marked by the asterisk in Fig. 23.1). The ticks at the top mark the position of layers with radial coordinates $r = 0.001, 0.01, 0.1$ and $1 R$ (the $0.01 R$ tick isn't labeled due to lack of space). The orange-shaded region indicates the (very narrow) hydrogen-burning shell; the gray-shaded/dotted region indicates the extended convective envelope. Compare against Fig. 6.1.

During RGB evolution, the stellar luminosity grows significantly. To understand why, let's create simple scaling relations for the properties of the hydrogen-burning shell based on the following assumptions:

- (i) the mass Δm and radial extent Δr of the shell are small compared to the mass M_c and radius R_c of the core;
- (ii) the temperature, density and pressure at the top of the shell are negligible compared to their values at the bottom of the shell, and vice versa for the interior luminosity;
- (iii) energy is transported within the shell by radiation, with an opacity that's independent of density and temperature;
- (iv) neutrino losses are negligible within the shell, and nuclear energy generation follows the scaling $\epsilon_{\text{nuc}} \propto \rho^\alpha T^\beta$.

Then, by applying the stellar structure equations [18.1]–[18.4] across the shell, we obtain¹

$$\begin{aligned} \frac{\Delta r}{\Delta m} &\propto \frac{1}{R_c^2 \rho_b}, & \frac{P_b}{\Delta m} &\propto \frac{M_c}{R_c^4}, \\ \frac{\ell_t}{\Delta m} &\propto \rho_b^\alpha T_b^\beta, & \frac{T_b}{\Delta m} &\propto \frac{\ell_t}{R_c^4 T_b^3}, \end{aligned} \quad [23.1]$$

where the subscripts 'b' and 't' refer to the bottom and top of the shell, respectively. We need two further equations to close this system. For one, we adopt the ideal-gas scaling $P_b \propto \rho_b T_b$; for the other we assume that the shell's radial extent is a fixed fraction of the core radius, so that $\Delta r \propto R_c$. Then, we solve the equations to find the following scalings²:

$$\ell_t \propto M_c^{\frac{4\alpha+\beta+4}{\alpha+2}} R_c^{\frac{-3\alpha-\beta}{\alpha+2}}, \quad T_b \propto M_c R_c^{-1}, \quad \Delta m \propto M_c^{\frac{-\beta+4}{\alpha+2}} R_c^{\frac{3\alpha+\beta}{\alpha+2}} \quad [23.2]$$

At the high temperatures encountered in hydrogen-burning shells, $\alpha = 1$ and $\beta \approx 13$. With these values, the luminosity and mass scalings above become

$$\ell_t \propto M_c^7 R_c^{-16/3}, \quad \Delta m \propto M_c^{-3} R_c^{16/3} \quad [23.3]$$

As we'll see in the next handout, the core radius varies inversely with core mass. Therefore, these expressions indicates that the stellar luminosity³ grows extremely rapidly with increasing core mass; and the shell mass likewise shrinks.

Further Reading

Kippenhahn, Weigert & Weiss, §§33.1,33.2; Ostlie & Carroll, §13.2; Privalnik, §9.4.

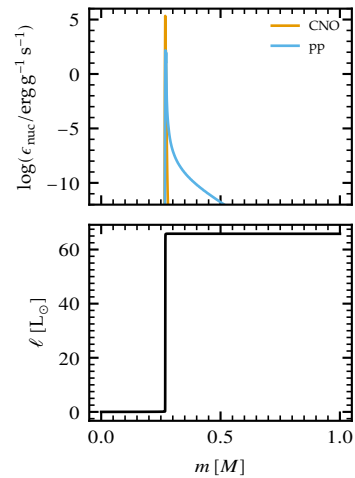


Figure 23.3: The logarithm of the nuclear energy generation rate ϵ_{nuc} from the pp chains and the CNO cycle (upper panel), and the interior luminosity ℓ (lower panel), plotted as a function of interior mass m for the same MESA model presented in Fig. (23.2).

¹ To derive the upper-left scaling relation from the mass equation [18.1], on the left-hand side approximate $\partial r/\partial m$ with $\Delta r/\Delta m$; and on the right-hand side, approximate r with R_c and ρ with ρ_b . Similar approaches give the other scaling relations.

² The scalings for P_b and ρ_b can also be derived, but are less interesting.

³ Because there is no energy generation above the shell (see lower panel of Fig. 23.3), the stellar luminosity L matches the interior luminosity ℓ_t at the top of the shell.

24 The Helium Flash

Core Degeneracy on the RGB

For low and intermediate-mass stars on the red giant branch, the central density ρ_c is sufficiently high (relative to the central temperature T_c) that $\mathcal{E}_{F,c} \gg k_B T_c$, and so the free electrons in the core are degenerate. This is demonstrated in Fig. 24.1, which shows the path followed by a $1 M_\odot$ model in the $\log \rho_c$ - $\log T_c$ plane, as it evolves from the pre-main sequence to the tip of the RGB.

The onset of electron degeneracy has an important consequence for how the radius R_c of the core changes as its mass M_c grows by the deposition of fresh helium¹. Assuming the electrons are completely degenerate in the core, and their pressure is much larger than the ion or radiation pressures, the EOS in the core follows the scaling²

$$P \propto \rho^{5/3}, \quad [24.1]$$

which can be recognized as an instance of the polytropic relation [19.1]. Because the envelope of an RGB star has negligible density compared to its core (see, e.g., Fig. 23.2), it's reasonable to pretend the envelope isn't there, and treat the core as a polytrope in its own right. From eqns. [19.11] and [19.12], the central density and pressure then follow the scalings

$$\rho_c \propto \frac{M_c}{R_c^3}, \quad P_c \propto \frac{M_c^2}{R_c^4}. \quad [24.2]$$

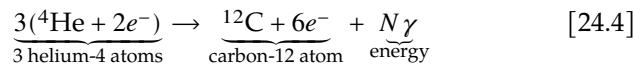
Substituting these back into the EOS [24.1] yields a *mass-radius relation for RGB cores*,

$$R_c \propto M_c^{-1/3}. \quad [24.3]$$

This scaling is approximate, but reproduces an important feature of RGB stars: as their core mass increases, their core radius decreases.

The Approach to Helium Ignition

In eqn. [23.2] we showed that the temperature at the bottom of the hydrogen-burning shell in an RGB star scales as $T_b \propto M_c/R_c$. With the core mass-radius relation [24.3], we can expect the shell temperature to grow $\propto M_c^{4/3}$ as the star ascends the RGB. During this evolutionary phase, the high thermal conductivity of the helium core³ maintains its temperature close to that of the shell; as the shell gets hotter, so does the core. Eventually, the core reaches the temperatures necessary for helium burning via the *triple alpha* (3α) reaction:



The ignition of helium doesn't take place at the very center of the star, because non-nuclear neutrino production causes the gradual removal of energy from the core, cooling it (see Fig. 24.2; also, *Handout 10*).

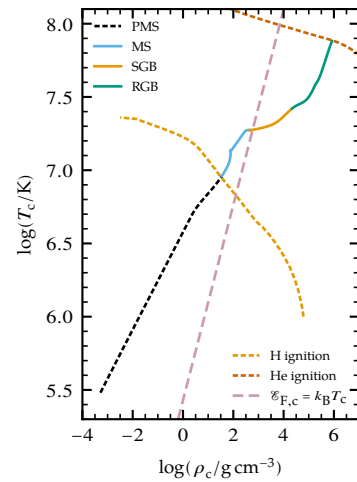


Figure 24.1: Path followed in the $\log \rho_c$ - $\log T_c$ plane for a $1 M_\odot$ MESA model, as it evolves from the pre-main sequence to the tip of the RGB (see Fig. 23.1 for the corresponding track in the HR diagram). The diagonal dashed line shows where $\mathcal{E}_{F,c} = k_B T_c$, and divides the plane into classical (left) and degenerate (right) regimes. The light (dark) orange dotted line shows the locus in the plane where hydrogen (respectively, helium) ignites.

¹ The helium is produced in the hydrogen-burning shell, situated just outside the core (see *Handout 23*).

² This expression comes from substituting the electron pressure [16.11] into eqn. [15.1], neglecting the P_{ion} and P_{rad} terms, and replacing n_e with $\rho/\mu_e m_H$. Note that it may appear similar to the adiabatic relation [6.8], but an important difference is that the constant of proportionality here is *independent* of temperature, and involves only on the composition of the core and physical constants.

³ A consequence of the degenerate electrons (and the same reason why copper, aluminum and other solid metals are good thermal conductors).

Instead, the ignition occurs off-center (but still within the core) at the point which first reaches the ignition temperature $T \approx 10^8$ K.

The Helium Flash

When helium ignition first occurs, the release of energy by the 3α reaction causes the temperature to rise. In ordinary matter, a temperature rise is accompanied by a pressure increase, which drives expansion and subsequent cooling. However, in degenerate matter this negative feedback loop doesn't work, because the pressure is decoupled from the temperature. Instead, the temperature continues to increase, raising the reaction rate and releasing even more energy. The runaway only ends when the temperature becomes so high that the free electrons are no longer degenerate; then, their pressure finally increases, expanding and cooling the burning region.

During this *helium flash* process, the luminosity generated by the 3α reaction spikes up to values $\sim 10^9 L_\odot$ comparable to a whole galaxy's worth of stars. After a few days, however, it drops back down to small values $\lesssim L_\odot$. A series of after-flashes then occur at locations progressively closer to the center of the star. The recurrence timescale between these flashes is on the order of a few hundred thousand years, and they are weaker but longer-lasting than the original. Eventually, helium ignites at the center of the star, which by now is non-degenerate, and the star settles into a state of steady helium burning. Fig. 24.3 illustrates this sequence of events for the $1 M_\odot$ model.

Although the luminosity generated by helium burning can reach immense values during flashes, none of this energy makes its way to the surface of the star. Instead, it is absorbed by the material in the outer parts of the core, driving the expansion of the core. Nevertheless, there is an observable consequence to a star passing through the helium flash phase. With the scaling

$$\ell_t \propto M_c^7 R_c^{-16/3}$$

derived in eqn. [23.3], the hydrogen-burning luminosity $L_H \sim \ell_t$ is significantly reduced when the core expands in response to helium ignition. This behavior can clearly be seen in Fig. 24.3, immediately after the initial flash and then after the subsequent flashes. Once the flashes die down and the star comes back into thermal equilibrium, its luminosity $L = L_H + L_{He}$ is smaller (by over an order-of-magnitude) than it was prior to helium ignition. This is typical behavior for core helium-burning stars, which appear at lower luminosities in the HR diagram than stars near the tip of the RGB.

Further Reading

Kippenhahn, Weigert & Weiss, §§33.4,33.5.

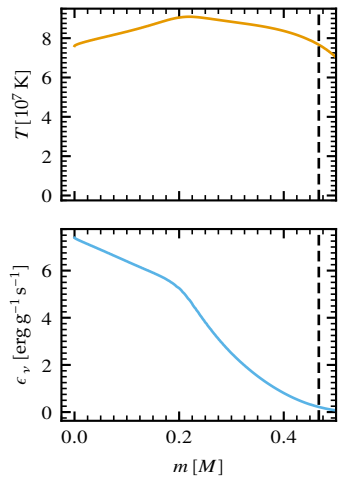


Figure 24.2: Temperature T (upper panel) and non-nuclear neutrino energy loss rate ϵ_ν , (lower panel), plotted as a function of interior mass m in the core of the $1 M_\odot$ MESA model just prior to helium ignition. Cooling at the center, predominantly by the creation of so-called *plasma neutrinos*, means that the temperature maximum, where the helium ignition will take place, is situated off-center at $m \approx 0.2 M_\odot$. The vertical dashed line in each panel marks the position of the core boundary.

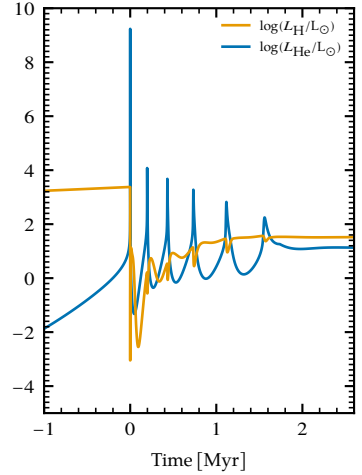
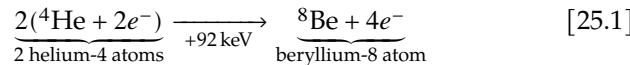


Figure 24.3: The hydrogen-burning luminosity L_H and the helium-burning luminosity L_{He} , plotted as a function of stellar age since the initial helium flash for the $1 M_\odot$ MESA model.

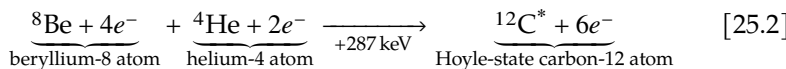
25 The Horizontal Branch

The Triple Alpha Reaction

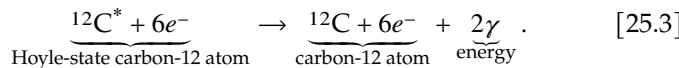
Helium in stars is fused to carbon via the triple alpha reaction. We've already encountered this reaction in schematic form (see eqn. [24.4]), but let's now examine it in detail. Because three-particle nuclear interactions are vanishingly improbable, the reaction proceeds via a pair of two-particle steps. In the first step, two alpha particles fuse to form a beryllium-8 nucleus; in balanced form,



Importantly, this is an *endothermic* reaction: it requires 92 keV of energy to occur, which is supplied through the kinetic energy of the alpha particles. The resulting beryllium-8 nucleus is highly unstable, and almost always fissions back into the alpha particles after $\sim 10^{-16}$ s. However, if a third alpha particle hits the beryllium-8 before this occurs, then something else can happen:



Again, this is an endothermic reaction, requiring 287 keV of kinetic energy to occur. The asterisk on the carbon-12 nucleus on the right-hand side indicates that this is an excited state of the nucleus — the so-called *Hoyle state*¹, at an energy 7.654 MeV above the ground state. Most of the time, the Hoyle state fissions back into a beryllium-8 nucleus and an alpha particle. However, it can also undergo a two-photon radiative decay to the carbon-12 ground state:



The net energy released by the triple alpha reaction is $\Delta E = (3m_{\text{He}} - m_{\text{C}})c^2 = 7.275 \text{ MeV}$; but we could also have calculated this value by differencing the energy inputs (as kinetic energy) and outputs (as gamma rays): $\Delta E = (7.654 - 0.092 - 0.287) \text{ MeV} = 7.275 \text{ MeV}$.

The Horizontal Branch & Red Clump

Stars that are steadily burning helium in their cores² are known as *horizontal branch* (HB) stars. This term originates from observations: the Hertzsprung–Russell diagrams of star clusters often show an over-density of stars lying along a horizontal line of approximately constant luminosity, extending from the RGB over to the blue (see Fig. 25.1). A simple theoretical explanation for the position and orientation of the horizontal branch is not straightforward to formulate, but numerical calculations confirm that stars on the horizontal branch must be burning helium in their cores.

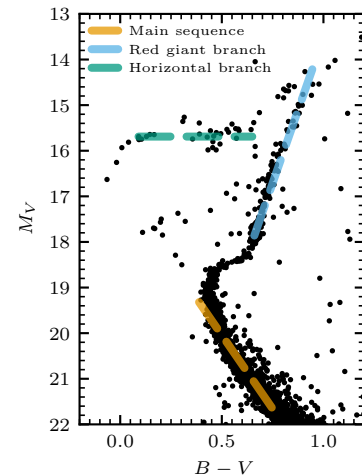


Figure 25.1: A color-magnitude diagram (CMD) for the globular cluster Messier 3, based on measurements by Rey et al. (2001, AJ, 122, 3219). CMDs are an observational type of HR diagram, with color shown on the horizontal axis and absolute magnitude on the vertical axis. The thick dashes lines highlight three evolutionary stages visible in the distribution of the cluster's stars.

¹ Named after Fred Hoyle, who hypothesized that this excited state must exist, otherwise there would be very little carbon formed in the universe — and hence no life as we know it. This is perhaps the most famous application of the *anthropic principle*. The existence of the Hoyle state was confirmed experimentally by Willie Fowler, who received the Nobel prize for his work.

² i.e., after the helium flash phase has completed.

The position of a given star on the HB depends on two important factors: the mass M_{env} of the hydrogen-rich envelope around the star's helium core, and the metallicity Z of this envelope. After the helium flash, all stars move onto the HB with approximately the same core mass $M_c \approx 0.47 M_\odot$; this is because the flash occurs when the core temperature reaches $T_c \approx 10^8 \text{ K}$, and — as we showed in *Handout 24* — the core temperature is set by M_c .

However, the envelope mass depends on the total mass of the star via $M_{\text{env}} = M - M_c$. Stars with M only a little above the initial $M_c \approx 0.47 M_\odot$ have a very thin envelope, and appear toward the blue end of the HB; whereas stars with an appreciably larger M have a correspondingly thicker envelope, and appear toward the red end of the HB. These trends are illustrated in Fig. 25.2, which plots the horizontal branches calculated by *MESA* for three different choices of metallicity. Each HB spans a range of stellar masses, with the low-mass end appearing on the left and the high-mass end on the right.

In addition to shifting the HB toward slightly lower luminosities, increasing the envelope metallicity Z reduces the relative number of stars at the blue end (see Fig. 25.2). For metallicities $Z \gtrsim 0.002$ (i.e., around one tenth of the Sun upward), the concentration of stars toward the red end becomes so pronounced that the horizontal branch no longer appears as a line in the HR diagram, but rather as a compact feature known as the *red clump*.

Energy Production on the Horizontal Branch

Even though much of the foregoing discussion focuses on core helium burning, this isn't the only way horizontal branch (and red clump) stars generate energy. In fact, the hydrogen-burning shell that was responsible for energy generation during the RGB phase remains operative, just outside the helium core. This is demonstrated in Fig. 25.3 for a $1 M_\odot$ in the red clump (compare against Fig. 23.3). Note how the luminosity generated by the shell, at a mass coordinate $m \approx 0.47 M$, exceeds the luminosity generated at the center. This indicates that more of the star's total luminosity is generated by hydrogen burning than by helium burning — even though we would typically describe the star as helium burning.

Further Reading

Kippenhahn, Weigert & Weiss, §33.6; Ostlie & Carroll, §13.2; Prialnik, §9.5.

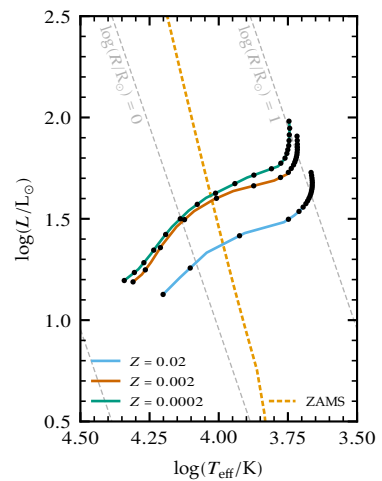


Figure 25.2: Horizontal branches in the Hertzsprung-Russell diagram calculated using *MESA* for three different choices of the metallicity Z . Each HB spans the mass range $0.49 M_\odot \leq M \leq 1.2 M_\odot$; the black dots show the positions of 20 stars in this range whose masses follow the distribution function $f(M) \propto M^{-2.35}$ (this is the so-called *Salpeter initial mass function*, which was derived from measurements of how many stars are born at each mass). The ZAMS line is for solar metallicity, $Z = 0.02$.

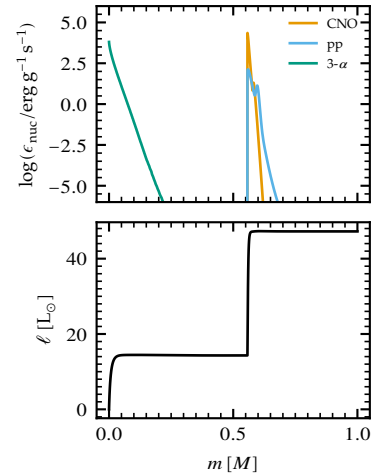


Figure 25.3: The logarithm of the nuclear energy generation rate ϵ_{nuc} from the pp chains, CNO cycle and triple alpha reaction (upper panel), and the interior luminosity ℓ (lower panel), plotted as a function of interior mass m for $1 M_\odot$ solar-metallicity *MESA* model soon after it arrives in the red clump.

26 The Asymptotic Giant Branch

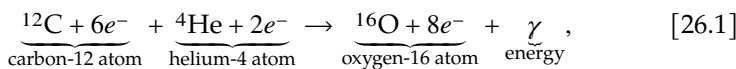
Evolution onto the Asymptotic Giant Branch

When a star on the horizontal branch or red clump eventually runs out of helium fuel in its core, it begins another series of dramatic changes. Much as it did during the red giant branch, it evolves along a mostly vertical path in the Hertzsprung-Russell diagram toward large radii and luminosities but low effective temperatures (see Fig. 26.1). This phase of evolution is known as the *asymptotic giant branch* (AGB).

Structure on the AGB

The internal structure of a star during the AGB phase shares many similarities with its structure during the earlier RGB phase. Most importantly, the star once again exhibits a pronounced dichotomy between core and envelope; a massive, dense radiative core, spanning only a small fraction of the star's radius, is surrounded by a low-density convective envelope (see Fig. 26.2).

One significant difference from the RGB phase, however, is the composition of the core. Unlike the almost-pure helium cores encountered on the RGB, the core of AGB stars are composed of a mixture of carbon and oxygen. The carbon is produced by the triple alpha reaction during the earlier core helium burning, as discussed in *Handout 25*. The oxygen results from fusion of carbon and helium,



an example of an *alpha capture* reaction. The reaction releases $\Delta E = (m_{\text{C}} + m_{\text{He}} - m_{\text{O}})c^2 = 7.161 \text{ MeV}$, and out-competes triple alpha toward the end of the core helium burning.

Double-Shell Energy Generation

Stars on the AGB generate energy in a pair of shells: an inner helium-burning shell, and an outer hydrogen-burning shell. These shells are sandwiched between the hydrogen-rich envelope and the carbon-oxygen core; and between the shells themselves is a narrow helium layer. The hydrogen-burning shell adds fresh helium to the top of this layer, and the helium-burning shell eats into the bottom of the layer. As a star ascends the AGB, both shells move outward to larger interior masses.

The Slow Neutron Capture Process

The AGB is an important phase of *stellar nucleosynthesis* — the process by which stars manufacture elements heavier than hydrogen, helium and lithium (the three elements created in the Big Bang). If some kind

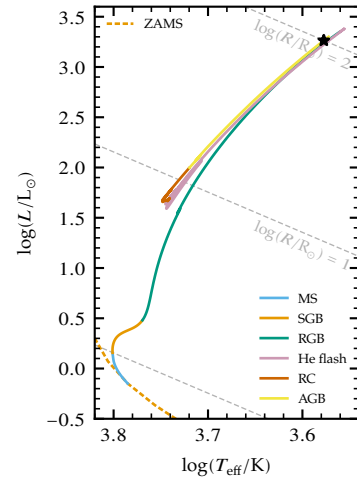


Figure 26.1: Evolutionary track in the Hertzsprung-Russell diagram for a $1 M_{\odot}$ MESA model, spanning the main sequence (MS), sub giant branch (SGB), red giant branch (RGB), helium flash, red clump (RC), and asymptotic giant branch (AGB) phases. The asterisk marks the case plotted in Fig. 26.2.

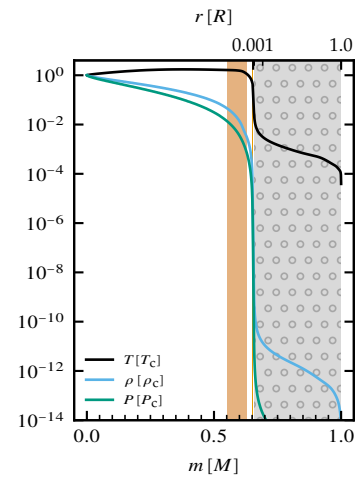
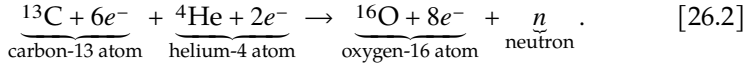
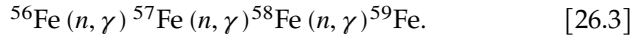


Figure 26.2: The temperature T , density ρ and pressure P (in units of their central values $T_c = 9.68 \times 10^7 \text{ K}$, $\rho_c = 1.32 \times 10^6 \text{ g cm}^{-3}$, $P_c = 4.04 \times 10^{22} \text{ Ba}$), plotted as a function of interior mass m for the $1 M_{\odot}$ model at $R = 100 R_{\odot}$ on the AGB (marked by an asterisk in Fig. 26.1). The ticks at the top mark the position of layers with radial coordinates $r = 0.001, 0.01, 0.1$ and $1 R$. The light (dark) orange-shaded region indicates the hydrogen-burning (respectively, helium-burning) shell; the gray-shaded/dotted region indicates the extended convective envelope. Compare against Figs. 6.1 and 23.2.

of mixing brings fresh hydrogen into the helium layer between the shells, then carbon-13 arising in an intermediary stage of the CNO cycle¹ will undergo alpha capture to produce oxygen and a free neutron:



Because it is not affected by Coulomb forces, the neutron can easily be captured by other nuclei. It is through this process of *neutron capture* that all of the elements heavier than iron-56 are manufactured inside stars². Neutron capture by iron-56 leads to the creation of successively heavier isotopes of iron; in shorthand form,

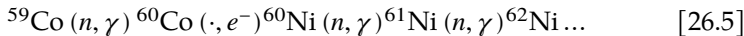


Unlike the lighter isotopes, iron-59 is radioactive, decaying to cobalt-59 via emission of a β particle:



(to conserve lepton number, an electron antineutrino is also produced in this reaction). This reaction is relatively slow, with a half-life of 44.5 d; however, the neutron production reaction [26.2] is even slower, and so there is a very low probability of the iron-59 capturing another neutron before it decays. This kind of neutron capture — where radioactive elements always decay before capturing another neutron — is known as *slow* or *s-process* capture, and is characteristic of AGB stars.

After the decay to cobalt-59, which is stable, the neutron capture proceeds again. As shown in the top panel of Fig. 26.3, the first few steps beyond cobalt-59 are as follows:



Through a sequence of neutron captures and radioactive decays, the s-process builds elements all the way up to bismuth-209, the heaviest stable element³. An additional neutron capture leads to the production of polonium-210, which then decays via α emission back to lead-206 (see the lower panel of Fig. 26.3). Thus, the s-process cannot proceed any further.

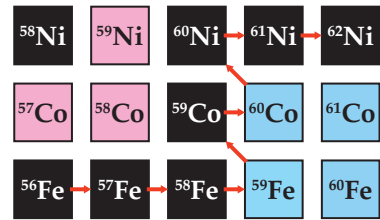
Further Reading

Kippenhahn, Weigert & Weiss, §18.6, 34; Ostlie & Carroll, §13.2; Privalnik, §9.6.

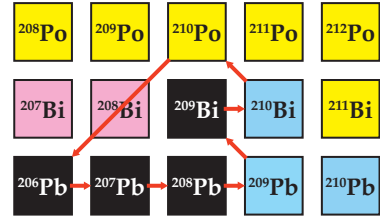
¹ See the first two steps of eqn. [22.7].

² As we'll discuss in later handouts, the iron-56 itself comes from earlier generations of stars that exploded as supernovae.

(a)



(b)



■ stable □ β^- decay
 ■ α decay □ β^+ decay

Figure 26.3: Nuclide charts (with atomic number increasing upward, and neutron number increasing rightward) for the start (a) and end (b) of s-process neutron capture in AGB stars. Isotopes are colored according to their principal decay mode. Neutron captures correspond to the right-pointing arrows; β emission to the up-left arrows; and α emission to the down-left arrows.

³ Strictly speaking, bismuth-209 is radioactive, decaying by α emission; but its half-life is 2.01×10^{19} yr, over a billion times longer than the current age of the Universe. So, it's effectively stable.

27 Thermal Pulses & Mass Loss

Thermal Pulses

As stars approach the top of the asymptotic giant branch, the helium-burning shell¹ exhibits a series of unstable events that are reminiscent of the core helium flash at the tip of the RGB. We'll delve into the cause of these *shell flashes* below, but first let's examine their consequences. During a shell flash, the luminosity produced by triple-alpha reaction spikes up by a factor $\sim 10^3$. This excess energy cannot be radiated by the star over short timescales, and is instead absorbed by the helium layer between the burning shells, causing it to expand. This expansion cools the hydrogen-burning shell atop the layer, to such an extent that its nuclear reactions almost cease. The overall effect is to significantly reduce the star's surface luminosity, in a manner reminiscent of the luminosity drop that occurs after the helium flash.

A shell flash cannot be sustained for long; having consumed most of the helium layer, the helium-burning shell runs out of fuel. After some time, the hydrogen-burning shell recovers and begins to rebuild the helium layer. Eventually, the layer becomes thick enough for another shell flash to occur, and the whole cycle — known as a *thermal pulse* — repeats. Fig. 27.1 illustrates a single thermal pulse for a $1 M_{\odot}$ MESA model.

The phase on the AGB when thermal pulses arise is known as the *thermally pulsing AGB (TP-AGB)*. During this phase, a star moves up and down the asymptotic giant branch in the Hertzsprung-Russell diagram (see Fig. 27.2), with maximal surface luminosity corresponding to minimal helium-burning luminosity, and vice versa (this anti-correlation can clearly be seen in Fig. 27.1).

The Thin-Shell Instability

While the core helium flash is a consequence of electron degeneracy, shell helium flashes arise even in non-degenerate conditions. To understand this, let's consider a thin shell which spans radial coordinates $[r_b, r_t]$ and interior masses $[m_b, m_t]$ ². The density in the shell can be approximated as its mass $\Delta m \equiv m_t - m_b$ divided by its volume,

$$\rho \approx \frac{\Delta m}{4\pi r_b^2 \Delta r}, \quad [27.1]$$

where $\Delta r \equiv r_t - r_b$ is the shell's radial thickness. Likewise, the pressure in the shell can be approximated by integrating the equation of hydrostatic equilibrium from the surface downward to the mass midpoint $m_m \equiv (m_b + m_t)/2$ of the shell:

$$P \approx \int_{m_m}^M \frac{Gm}{4\pi r^4} dm. \quad [27.2]$$

Now let's consider what happens to the shell pressure and density as r_t varies while keeping r_b fixed³. The change in density is

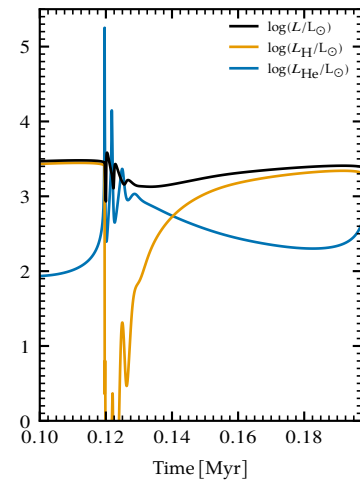


Figure 27.1: The surface luminosity L , hydrogen-burning luminosity L_H and helium-burning luminosity L_{He} , plotted as a function of time for a $1 M_{\odot}$ MESA model during a thermal pulse. The time zero-point is at the beginning of the TP-AGB phase. The plot reveals the interplay between L , L_H and L_{He} during the pulse.

¹ Recall that AGB stars are powered by two shells: an outer hydrogen-burning shell and an inner helium-burning shell, with a helium layer sandwiched between them. See *Handout 26* for more details.

² As in *Handout 23*, the subscripts 'b' and 't' refer to the bottom and top of the shell, respectively.

³ Since the shell always contains the same material, m_b and m_t also remain fixed.

$$\delta\rho = \frac{\partial\rho}{\partial r_t} \delta r_t \approx -\rho \frac{\delta r_t}{\Delta r}, \quad [27.3]$$

where δr_t is the change in r_t . To evaluate the change in pressure, we assume that the r term in the denominator of the integrand in eqn. [27.2] scales proportionately to r_t , leading to

$$\delta P = \frac{\partial P}{\partial r_t} \delta r_t \approx -4P \frac{\delta r_t}{r_t}. \quad [27.4]$$

Assuming the material in the shell behaves as an ideal gas, then the change δT in its temperature can be evaluated⁴ from $\delta\rho$ and δP as

$$\frac{\delta T}{T} = \frac{\delta P}{P} - \frac{\delta\rho}{\rho} \approx \left(1 - 4 \frac{\Delta r}{r_t}\right) \frac{\delta r_t}{\Delta r}. \quad [27.5]$$

For thin shells ($\Delta r \ll r_t$) the term in parentheses is positive, indicating that an expansion of the shell is accompanied by a rise in its temperature. This *thin-shell instability* drives the helium shell flashes during the TP-AGB: an expansion of the shell raises its temperature, increasing the energy release rate of the triple alpha reaction. This raises the temperature and pressure in the shell, causing it to expand further, and so on.

Mass Loss on the Giant Branches

The TP-AGB phase is ultimately brought to an end by mass loss. The large luminosities of both RGB and AGB stars drive significant *stellar winds*, with mass-loss rates given approximately by⁵

$$\begin{aligned} \dot{M}_{\text{RGB}} &\approx -4 \times 10^{-13} M_{\odot}/\text{yr} \times \left(\frac{L}{L_{\odot}}\right) \left(\frac{R}{R_{\odot}}\right) \left(\frac{M}{M_{\odot}}\right)^{-1}, \\ \dot{M}_{\text{AGB}} &\approx 5 \times 10^{-9} \dot{M}_{\text{RGB}} \times \left(\frac{M}{M_{\odot}}\right)^{-2.1} \left(\frac{L}{L_{\odot}}\right)^{2.7}, \end{aligned} \quad [27.6]$$

respectively. At the highest luminosities during the TP-AGB phase, \dot{M}_{AGB} can reach values $10^{-5} M_{\odot}/\text{yr}$. This so-called *superwind* rapidly strips most of the remaining hydrogen envelope from the star, terminating the TP-AGB phase and launching the star toward the blue in the HR diagram (see Fig. 27.2).

Further Reading

Kippenhahn, Weigert & Weiss, §§34.3,34.6; *Ostlie & Carroll*, §13.2; *Prialnik*, §§9.6,9.7.

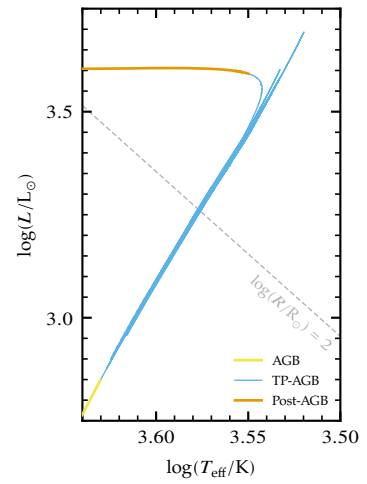


Figure 27.2: Evolutionary track in the Hertzsprung–Russell diagram for a $1 M_{\odot}$ MESA model, spanning the asymptotic giant branch (AGB), thermally pulsing AGB (TP-AGB) and post-AGB phases.

⁴ By applying eqn. [13.3].

⁵ The first expression is from an empirical fit to observations of RGB stars by Reimers (1975, *Problems in Stellar Atmospheres and Envelopes*); the second from numerical simulations of AGB stars by Blöcker (1995, *A&A*, **297**, 727).

28 White Dwarfs

Planetary Nebulae

With the onset of a superwind (see *Handout 27*), an AGB star rapidly ejects most of its hydrogen-rich envelope. This exposes the star's deeper, hotter layers, causing it to evolve rapidly toward the blue in the Hertzsprung-Russell diagram (see Fig. 28.1). Once the star's effective temperature increases above about 3×10^4 K, it emits sufficient radiation in the UV to ionize the ejecta. The ionized material appears as a glowing shell — or sometimes, a more-complex structure — around the star (see Fig. 28.2), and is known as a *planetary nebula*¹.

White Dwarfs

When the effective temperature of a post-AGB star reaches around 10^5 K, it turns a corner in the HR diagram: its luminosity drops rapidly, and then it begins to evolve diagonally down and to the red. The star has become a *white dwarf*, the final evolutionary state for all stars with initial masses $\lesssim 9 M_\odot$.

White dwarfs (WDs) are compact objects, with radii $\sim 10^{-2} R_\odot$ comparable to the Earth. Their central densities exceed 10^6 g cm^{-3} , while central temperatures are $\lesssim 10^7$ K; therefore, the free electrons at the center of white dwarfs are extremely degenerate². In fact, degeneracy holds throughout almost all of WD interiors; in only a very thin surface layer, comprising around a billionth of the star by mass, does the material behave like an ideal gas.

Fig. 28.3 plots the composition profile of a $0.54 M_\odot$ *carbon-oxygen white dwarf*, the end state of the $1 M_\odot$ MESA model we've been examining in previous handouts. The inner $\sim 95\%$ by mass is composed of carbon and oxygen; most of the remaining $\sim 5\%$ is composed of helium; and a tiny fraction $\sim 0.01\%$ is composed of hydrogen, the remnant of the hydrogen-rich layers that were ejected to form a planetary nebula.

White Dwarf Cooling

WDs cool down via the loss of thermal energy from the ions in their interior³. To explore this process, let's create simple scaling relations for the luminosity of a WD based on the following assumptions:

- (i) the star can be treated as a completely degenerate, isothermal core with radius R and mass M , surrounded by a thin ideal-gas atmosphere with thickness $\Delta r \ll R$ and mass $\Delta m \ll M$.
- (ii) the boundary between core and atmosphere occurs where the ideal and degenerate pressures match;
- (iii) the temperature, density and pressure at the top of the atmosphere

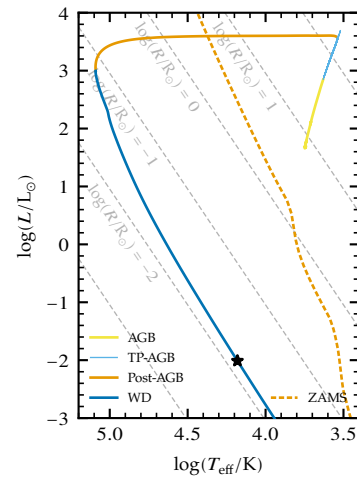


Figure 28.1: Evolutionary track in the Hertzsprung-Russell diagram for a $1 M_\odot$ MESA model, spanning the asymptotic giant branch (AGB), thermally pulsing AGB (TP-AGB), post-AGB and white dwarf (WD) phases. Note that by the WD phase, the mass of the model is only $0.54 M_\odot$, with the remaining material having been ejected. The asterisk marks the case plotted in Fig. 28.3.

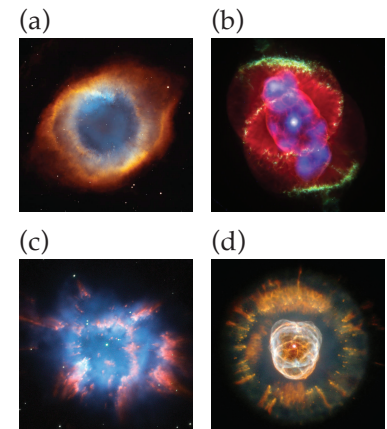


Figure 28.2: Images of four different planetary nebulae: (a) the Helix Nebula, (b) the Cat's Eye Nebula, (c) NGC 6326, and (d) the Eskimo Nebula. Image credits: NASA.

¹ A name coined in the 18th century by the astronomer William Herschel. In reality, planetary nebulae have nothing to do with planets.

² To see this, locate the $(\log \rho_c, \log T_c) = (6, 7)$ point in Fig. 24.1 of *Handout 24*.

³ Even though the electrons are completely degenerate, the ions still behave as an ideal gas.

are negligible compared to their values at the bottom of the atmosphere;

- (iv) the atmosphere is radiative, with a Kramers'-law opacity [12.8].

Then, applying the stellar structure equations [18.1]–[18.4] across the atmosphere (in a similar fashion to eqn. [23.1]), we obtain

$$\begin{aligned}\frac{\Delta r}{\Delta m} &\propto \frac{1}{R^2 \rho_b}, & \frac{P_b}{\Delta m} &\propto \frac{M}{R^4}, & \frac{T_b}{\Delta m} &\propto \frac{\ell_t \kappa}{R^4 T_b^3}, \\ P_b &\propto \rho_b T_b & \kappa &\propto \rho_b T_b^{-7/2},\end{aligned}\quad [28.1]$$

where the subscripts ‘b’ and ‘t’ refer to the bottom and top of the atmosphere, respectively. Solving for ℓ_t , we obtain the WD luminosity scaling as

$$L = \ell_t \propto M T_b^{7/2}. \quad [28.2]$$

The thermal energy of the ions in the interior scales⁴ as $U \sim M T_b$; with $L = -dU/dt$, we therefore arrive at a differential equation for the luminosity:

$$\frac{dL}{dt} \propto -M^{-5/7} L^{12/7}. \quad [28.3]$$

Solutions to this equation for fixed M follow the scaling $L \propto t^{-7/5}$, a result confirmed empirically in Fig. 28.4. Thus, the luminosity of a WD drops rapidly at first, but then decreases more and more gradually.

Other White Dwarf Varieties

The WD model plotted in Fig. 28.3 is classified as a DA-type star — the ‘D’ stands for dwarf, and the ‘A’ indicates that it shows strong hydrogen absorption lines in its spectrum (see *Handout 3*). Around 80% of WDs are DA type. Most of the remaining 20% are DB-type stars; these lack the thin outer layer of hydrogen shown in Fig. 28.3, and so show helium absorption lines instead of hydrogen in their spectra.

In addition to these atmospheric differences, it’s also possible for WDs to have different interior compositions than the carbon-oxygen case considered here. Extremely low mass (ELM) WDs, with masses $M \sim 0.1 - 0.2 M_\odot$ have helium interiors, and are thought to arise from binary evolution. Likewise, massive WDs ($M \gtrsim 1 M_\odot$) have oxygen-neon interiors, and arise from the evolution of stars with initial masses $M \sim 6 - 9 M_\odot$. We’ll discuss these possibilities in greater detail in later handouts.

Further Reading

Kippenhahn, Weigert & Weiss, §§16.4, 34.9, 37.3; *Ostlie & Carroll*, §16.2, 16.5; *Prialnik*, §§9.7, 9.8.

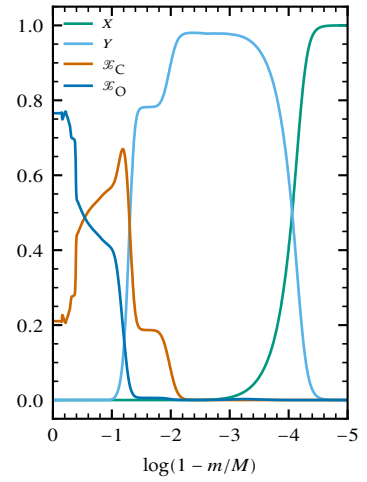


Figure 28.3: Composition profile of a $0.54 M_\odot$ MESA WD model at $L = 0.010 L_\odot$ (marked by an asterisk in Fig. 28.1), plotting mass fractions for hydrogen, helium, carbon and oxygen as a function of the logarithm of the fractional exterior mass $1 - m/M$.

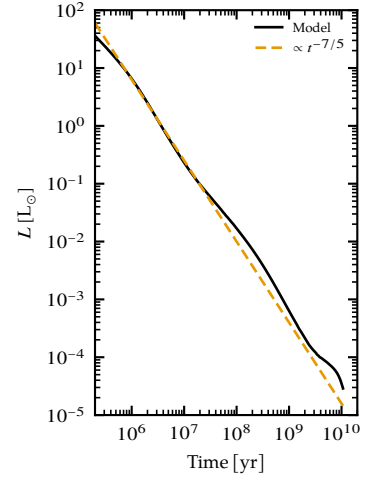


Figure 28.4: The luminosity L of the $0.54 M_\odot$ MESA WD model (Fig. 28.1), plotted as a function of time t since the beginning of the WD phase. The dashed line shows the scaling $L \sim t^{-5/7}$ derived in the text. In the lower-right corner of the plot, the effect of *crystallization* can be seen: the release of latent heat during the crystallization process causes a plateau in the star’s cooling.

⁴ This is because the interior is isothermal; see also eqn. [6.9].

29 Low-Mass Stellar Evolution

The Threshold for Helium Ignition

In Handout 25 we discussed how all stars arriving on the horizontal branch have the same core mass $M_c \approx 0.47 M_\odot$; and that this is a consequence of the temperature threshold $T_c \approx 10^8$ K for helium ignition in the core, coupled with the fact that T_c is set by M_c .

What happens, then, in stars which have a total mass $M \lesssim 0.47 M_\odot$? These *low-mass stars* can never create a sufficiently massive core for the helium to ignite, and thus they never experience a helium-burning phase. As a consequence, their evolution and final fate is rather different from stars like the Sun.

Evolution to the Red Giant Branch

Figure 29.1 plots the evolution of a $0.3 M_\odot$ star in the Hertzsprung-Russell diagram, extending from the pre-main sequence phase through to the star's final endpoint. Focusing first on the pre-main sequence, it's noteworthy that the track is vertically downward in the HR diagram, with no horizontal segment. This reflects the fact that this star¹ remains fully convective all the way to the ZAMS, and therefore follows a Hayashi track without ever switching to a Henyey track.

On the main sequence, the star moves almost vertically up in the HR diagram. About half-way through this phase, an intermediate radiative zone appears between the core and the envelope of the star. This zone, which soon grows to encompass the whole core, prevents any further convective mixing of fresh hydrogen from the envelope into the core. The development of the intermediate radiative zone can clearly be seen in Fig. 29.2, which plots the central hydrogen and helium mass fractions as a function of age; the abrupt steepening of the curves, around $t \approx 300$ Gyr, indicates that the core has become cut off from the envelope, causing its hydrogen content to diminish more rapidly (and vice versa for its helium content).

At the end of the main sequence, the star transitions onto the red giant branch with hydrogen burning in a shell around a helium core². As the star ascends the RGB, this shell burns its way outward through the envelope until *all* of the star (apart from a very thin surface layer) is helium.

Evolution beyond the Red Giant Branch

Once a low-mass star has run out of hydrogen, it begins to contract. However, unlike the earlier situation on the pre-main sequence, this contraction is not accompanied by heating of the stellar interior. As Fig. 29.3 shows, by the end of the RGB the conditions at the center of the $0.3 M_\odot$ star mean that free electrons are almost completely de-

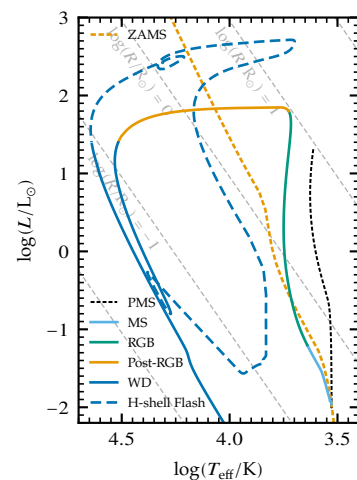


Figure 29.1: Evolutionary track in the Hertzsprung-Russell diagram for a MESA model of a $0.3 M_\odot$ star, spanning the pre-main sequence (PMS), main sequence (MS), red giant branch (RGB), post-RGB, white dwarf (WD) and hydrogen-shell flash phases.

¹ And, indeed, all stars with masses $M \lesssim 0.35 M_\odot$.

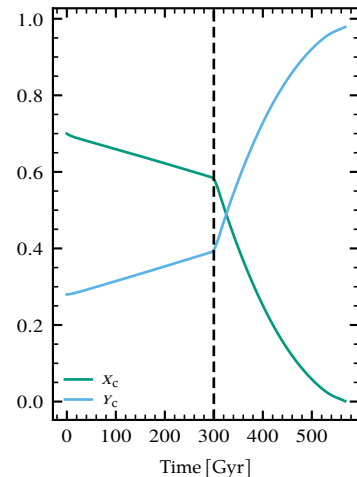


Figure 29.2: The hydrogen mass fraction X_c and helium mass fraction Y_c in the core of the $0.3 M_\odot$ MESA model, plotted as a function of stellar age since the ZAMS. The vertical dashed line shows the point where an intermediate radiative zone appears, preventing further mixing of hydrogen fuel from the envelope into the core.

² There is no meaningful sub-giant branch where the star moves to the right in the HR diagram; it transitions straight from the main sequence to the RGB.

generate. As a result, the virial theorem does not apply, and Kelvin-Helmholtz contraction³ does not occur. Rather, with increasing core density ρ_c , the core temperature T_c reaches a maximum and then drops rapidly. Since this maximum is well short of the $T_c \approx 10^8$ K required for the triple alpha reaction (*Handout 24*), the star never commences helium burning.

At the same time its core passes through the temperature maximum, the star evolves rapidly to the blue in the HR diagram (see Fig. 29.1), and then turns a corner to evolve diagonally down and to the red. This behavior is reminiscent of the solar model considered in *Handout 28*, and with good reason: the low-mass star also ends its life as white dwarf. However, there are a couple of important distinctions between the two cases. First, in the low-mass case a *helium white dwarf* is produced as the result of burning hydrogen into helium; whereas in the solar case a carbon-oxygen WD is produced as the result of hydrogen burning *followed by* helium burning. Second, if the helium WD has a mass $\gtrsim 0.15 M_\odot$, it experiences a *hydrogen-shell flash* during its cooling phase, which temporarily sends the star in the high-luminosity part of the HR diagram (see the dashed line in Fig. 29.1). This phase is brief, spanning only 50 Myr for the case shown. After the flash fizzles out, the WD continues to cool much as before.

Caveats

There are a couple of important caveats that apply to the foregoing discussion. First, the initial mass threshold for deciding whether a star will ultimately end up as a helium or carbon-oxygen WD is more like $M \lesssim 0.7 M_\odot$, due to the effects of mass loss on the RGB. Second, the main-sequence lifetimes of stars with masses $M \lesssim 0.8 M_\odot$ are expected to be longer⁴ than the current age of the Universe, ~ 13.8 Gyr. As a result, while the contents of this handout are a prediction of what we can expect in the future (if we hang around for long enough), the Universe is simply too young for any helium WDs to form via ordinary stellar evolution.

Curiously, however, we *do* actually observe helium WDs in the present-day Universe, in the guise of the ELM white dwarfs introduced in *Handout 28*. As we'll discuss in a later handout, these objects result from a more-massive star having its hydrogen envelope stripped away by a binary companion — i.e., *extraordinary* stellar evolution!

Further Reading

None; most textbooks ignore the topic of low-mass stellar evolution, because of the timescale caveat. But the physics is nevertheless interesting and illuminating, and certainly worth discussing.

³ Recall that K-H contraction is built on the virial theorem; see *Handout 8*.

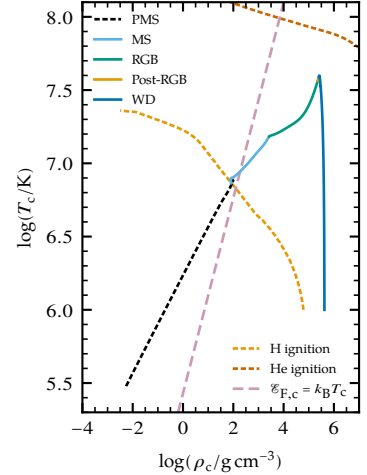


Figure 29.3: Path followed in the $\log \rho_c$ - $\log T_c$ plane for the $0.3 M_\odot$ MESA model shown in Fig. 29.1. The diagonal dashed line shows where $\mathcal{E}_{F,c} = k_B T_c$, and divides the plane into classical (left) and degenerate (right) regimes. The light (dark) orange dotted line shows the locus in the plane where hydrogen (respectively, helium) ignites.

⁴ For the $0.3 M_\odot$ model considered, this is abundantly clear from the horizontal axis of Fig. 29.2, which extends to almost 600 Gyr.

30 Binary Stars

Binary Stars and Optical Doubles

When we observe a pair of stars that are very close together on the sky — a so-called *double star* — it's natural to ask whether there's any kind of relationship between the stars. In some cases, the answer is 'no'; the stars' proximity is just a chance alignment, and in fact they're nowhere near one another in space. These are known as *optical doubles*.

In other cases, however, the answer is 'yes'; the stars are bound together by their own gravitational attraction, and orbit around their common center of mass. Such cases, known as *binary systems*, are particularly important tools for studying the structure and evolution of stars, as they offer unique opportunities to directly measure quantities like stellar mass. Moreover, if the stars in a binary system are sufficiently close, they can exchange mass during their lives, often with profound impacts on their final fate.

Types of Binary System

We divide binary systems into a number of different types, based on their observational characteristics. If we're able to resolve the two stars in a binary system (either with the naked eye, or with the use of a telescope) we classify the system as a *visual binary*. Otherwise, if we can only see one star in the system, or if both stars are so close together that they appear as a single point of light on the sky, we classify it as a *non-visual binary*.

Clearly, there has to be some property of a non-visual binary that tells us it comprises two stars. Again, there are a number of sub-types based on observational characteristics:

- *Spectrum binaries* show a spectrum that combines absorption lines from stars at different temperatures — for instance, lines due to singly ionized helium (only seen in stars with $T_{\text{eff}} \gtrsim 25\,000\text{ K}$) together with lines due to titanium dioxide (only seen in stars with $T_{\text{eff}} \lesssim 4000\text{ K}$).
- *Spectroscopic binaries* show a spectrum with absorption lines that undergo periodic changes in wavelength. These changes are due to the Doppler shifts arising as the stars move toward/away from the Earth. If the lines from only one star are seen¹, the binary is classified as a *single-lined spectroscopic binary*; if both sets are seen, it is a *double-lined spectroscopy binary*.
- *Astrometric binaries* show periodic changes in the position of one star on the sky, as it orbits around the system center of mass; the other star is too dim to detect.



Figure 30.1: The light curve of the eclipsing binary Algol (β Persei), plotting the changing magnitude as a function of time since minimum over one orbital cycle. From Stebbins (1921, *ApJ*, 53, 105). Note that Joel Stebbins would later take over as director of Washburn Observatory at UW-Madison, where he worked until he retired.

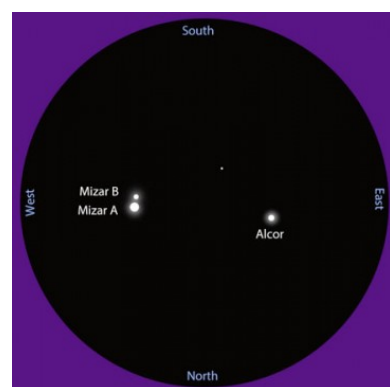


Figure 30.2: The ζ Ursae Majoris star system (the second star in from the end of the handle of the Big Dipper), as observed through a 4.5" telescope. As viewed here, the system is an optical double composed of Mizar and Alcor. Mizar itself is a visual binary, with components labeled A and B. Spectroscopy reveals that Mizar A, Mizar B and Alcor are all themselves spectroscopic binaries; and recent evidence suggests that the Mizar and Alcor systems are in fact gravitationally bound, making ζ UMa a hierarchical system of six stars.

¹ This can happen, for example, if the other star is so dim that it contributes negligibly to the binary spectrum.

- *Eclipsing binaries* show periodic changes in the overall brightness of the system, occurring as one star passes in front of the other and blocks out its light. For such eclipses to occur, the binary must be viewed from within the plane of the stars' orbits.

Often, a binary system may fall into multiple classifications; for instance, the famous eclipsing binary Algol² (whose light curve is shown in Fig. 30.1) is also a spectroscopic binary. Moreover, binaries often occur in hierarchical systems; an example is ζ Ursae Majoris, shown in Fig. 30.2.

Kepler's Laws

Stars in a binary system orbit around their common center of mass for the same reason that planets orbit around the Sun: mutual gravitational attraction. The motion of the planets was first (mostly) correctly described by Johannes Kepler, as an improvement on the earlier heliocentric model proposed by Nicolaus Copernicus. Kepler described this motion in the form of three laws:

1. The orbit of a planet is an ellipse with the Sun at one of the two foci (see Fig. 30.3 for a reminder of the properties of ellipses).
2. A line segment joining a planet and the Sun sweeps out equal areas during equal intervals of time (see Fig. 30.4 for a depiction of this equal-area law).
3. The square of the orbital period P of a planet is directly proportional to the cube of the semi-major axis a of its orbit. When the period is expressed in years, and the semi-major axis in astronomical units, the constant of proportionality is unity:

$$\left(\frac{P}{1 \text{ yr}}\right)^2 = \left(\frac{a}{1 \text{ au}}\right)^3 \quad [30.1]$$

Kepler's first law tells us about the shape of a planet's orbit (an ellipse); the second law tells us about the relative speed of the planet at different points on its orbit (fastest when closest to the Sun, slowest when furthest away); and the third law tells us about how the average speed changes from one planet to the next (dependent on the size of the orbit, but not on the mass of the planet). As we shall see, all three laws can be derived from Newton's laws of motion and gravitation.

Further Reading

Ostlie & Carroll, §§2.1,7.1; Prialnik, §11.1.

² From the Arabic *al ghūl*, literally 'the ghoul'.

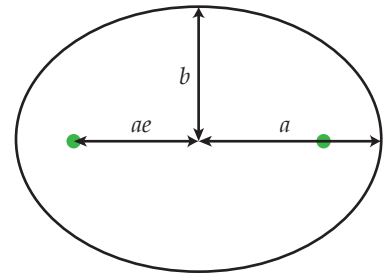


Figure 30.3: Schematic of an ellipse. The *semi-major axis* a and *semi-minor axis* b of the ellipse are the maximal and minimal distances of the boundary of the ellipse from its center. In terms of the eccentricity e of the ellipse, $b = a\sqrt{1 - e^2}$. For any point on the boundary, the sum of the distances from that point to each focus (shown by the green circles) is always $2a$.

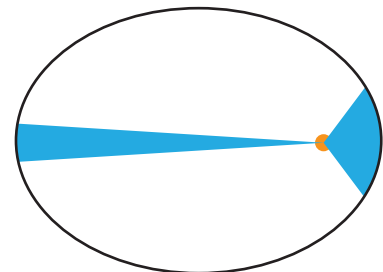


Figure 30.4: Kepler's second law illustrated graphically. The Sun is shown as the yellow circle at one focus of the elliptical orbit followed by a planet (there is nothing at the other focus). The areas of the shaded regions are the same, indicating that the planet takes equal times to sweep out these areas; therefore, it must be moving fastest when closest to the Sun (*perihelion*) and slowest when furthest from the Sun (*aphelion*).

31 Binary Orbits

The Two-Body Problem

Consider a pair of particles¹ with masses M_1 and M_2 , moving subject to their mutual gravitational attraction. Mathematically, this *two-body problem* involves solving the coupled differential equations that arise from applying Newton's second law and law of gravitation:

$$M_1 \ddot{\mathbf{r}}_1 = \frac{GM_1 M_2}{r^3} \mathbf{r}, \quad M_2 \ddot{\mathbf{r}}_2 = -\frac{GM_1 M_2}{r^3} \mathbf{r}, \quad [31.1]$$

where $\mathbf{r} \equiv \mathbf{r}_2 - \mathbf{r}_1$ is the displacement from the first particle to the second, $r \equiv |\mathbf{r}|$, and we use the standard notation that a dot indicates differentiation with respect to time.

¹ In our context, binary stars or a planet orbiting the Sun.

The One-Body Problem

Combining the two equations above, we can reduce the two-body problem to an equivalent *one-body problem* of a particle moving in a central potential:

$$\mathcal{M} \ddot{\mathbf{r}} = -\frac{GM_1 M_2}{r^3} \mathbf{r}, \quad [31.2]$$

where

$$\mathcal{M} \equiv \frac{M_1 M_2}{M_1 + M_2} \quad [31.3]$$

is the *reduced mass* of the system. It can be shown that solutions $\mathbf{r}(t)$ to the equation of motion [31.2] lie in a plane. Therefore, we write the equation in terms of polar coordinates² (r, θ) in this plane:

$$\mathcal{M} (\ddot{r} - r\dot{\theta}^2) = -\frac{GM_1 M_2}{r^2} \quad [31.4]$$

$$\mathcal{M} (r\ddot{\theta} + 2\dot{r}\dot{\theta}) = 0 \quad [31.5]$$

² Consult any classical mechanics text to understand the conversion of the equation of motion to polar coordinates.

The θ equation is trivially integrated once to obtain

$$\mathcal{M} r^2 \dot{\theta} = \mathcal{L} \quad [31.6]$$

where \mathcal{L} is a constant that we can recognize as the angular momentum of the system. The area swept out by the particle in time interval Δt is $r^2 \dot{\theta} \Delta t = (\mathcal{L}/\mathcal{M}) \Delta t$, and therefore we see that Kepler's second law (*Handout 30*) arises naturally from conservation of angular momentum.

To solve the r equation, we transform³ from t to θ as the independent variable, and to $u = 1/r$ as the dependent variable. After some algebra, we obtain

$$\frac{d^2 u}{d\theta^2} + u = \frac{GM_1 M_2 \mathcal{M}}{\mathcal{L}^2}. \quad [31.7]$$

The solution to this second-order differential equation is

$$u = \frac{GM_1 M_2 \mathcal{M}}{\mathcal{L}^2} (1 + e \cos \theta) \quad [31.8]$$

³ By applying the chain rule

$$\frac{d}{dt} = \frac{d\theta}{dt} \frac{d}{d\theta} = \frac{\mathcal{L}}{mr^2} \frac{d}{d\theta},$$

under the assumption that \mathcal{L} is non-zero.

where e is a constant of integration⁴. Hence, the solution to the radial equation is found as

$$r(\theta) = \frac{a(1 - e^2)}{1 + e \cos \theta}, \quad [31.9]$$

where

$$a = \frac{\mathcal{L}^2}{GM_1 M_2 \mathcal{M}} \frac{1}{1 - e^2}. \quad [31.10]$$

For $|e| < 1$ the solution [31.9] describes an ellipse with semi-major axis a , eccentricity e , and one focus situated at the origin⁵.

Suppose the origin of our coordinate system is at the center-of-mass of the system. It follows⁶ that the positions of each particle can be calculated from \mathbf{r} as⁷

$$\mathbf{r}_1 = -\frac{M_2}{M_1 + M_2} \mathbf{r}, \quad \mathbf{r}_2 = \frac{M_1}{M_1 + M_2} \mathbf{r}. \quad [31.11]$$

When we apply these expressions to the Solar System, with the Sun as particle 1 and a planet as particle 2, the fact that $M_1 \gg M_2$ leads to the approximations:

$$\mathbf{r}_1 \approx \mathbf{0}, \quad \mathbf{r}_2 \approx \mathbf{r}. \quad [31.12]$$

Hence, we find that the approximate orbit of the planet is an ellipse, with the Sun stationary at one focus; this is Kepler's first law. Of course, a more-precise description is that the orbits of the Sun and a planet are *both* ellipses⁸, with the center of mass at one focus.

The Orbital Period

To determine the orbital period P of a two-body system, consider the simple case of a circular⁹ binary ($e = 0$). The angular velocity of each particle is uniform, $\dot{\theta} = 2\pi/P$. Combining this with eqns. [31.6] and [31.10], we obtain after some algebra the result

$$P^2 = \frac{4\pi^2}{G(M_1 + M_2)} a^3. \quad [31.13]$$

Therefore, the period of the system depends only on combined mass of the particles and the semi-major axis of the system — not on their individual masses. When applied to planets in the Solar System, $M_1 + M_2 \approx M_\odot$, and we find that

$$\left(\frac{P}{1 \text{ yr}}\right)^2 = \left(\frac{a}{1 \text{ au}}\right)^3,$$

which is Kepler's third law [30.1].

Further Reading

Ostlie & Carroll, §2.3; *Prialnik*, §11.1.

⁴ Because this is the solution to a second-order equation, there should be two constants of integration. However, we've implicitly chosen one to ensure that u is maximal at $\theta = 0$.

⁵ For $|e| = 1$, eqn. [31.9] describes a parabola; and for $|e| > 1$ a hyperbola. However, these are not bound solutions ($r(\theta) \rightarrow \infty$ for certain choices of θ), and so we won't consider them further.

⁶ From setting the position coordinate of the center-of-mass, $\mathbf{r}_{\text{COM}} \equiv M_1 \mathbf{r}_1 + M_2 \mathbf{r}_2$, to zero.

⁷ The minus sign in the first equation means that the two particles are always on opposite sides of the center-of-mass.

⁸ The semi-major axes of these ellipses are not the same:

$$a_1 = \frac{M_2}{M_1 + M_2} a, \quad a_2 = \frac{M_1}{M_1 + M_2} a.$$

Note that $a_1 + a_2 = a$.

⁹ It can be shown (although with more effort) that the results derived here also apply to eccentric binaries.

32 Observing Binaries

The Inclination Problem

When we observe a binary system, we face the difficulty that we typically don't see the orbits face-on or edge-on, but rather from an arbitrary and (initially) unknown orientation. Conventionally, we characterize this orientation via the *inclination* i , defined as the angle between the orbital plane and the plane of the sky (onto which the orbit is projected; see Fig. 32.1); this is equivalent to the angle between the line-of-sight and the normal to the orbital plane.

Observing Visual Binaries

For visual binaries, the projection effect arising from an inclination $i > 0^\circ$ will alter the apparent shape of the orbit. Certain choices of i can make eccentric orbits appear more circular (smaller e), and vice versa. However, because projection works the same for both stars, the ratio of the semi-major axes in a visual binary follows as

$$\frac{a_1}{a_2} = \frac{\alpha_1}{\alpha_2}, \quad [32.1]$$

regardless of i ; here, α_1 is the angular size of the semi-major axis of the first star's *apparent* orbit, and similarly for α_2 . From note 8 of *Handout 31*, it follows that the mass ratio of the system is

$$\frac{M_2}{M_1} = \frac{a_1}{a_2} = \frac{\alpha_1}{\alpha_2}. \quad [32.2]$$

If the system happens to be face-on ($i = 0^\circ$; see Fig. 32.2 for a discussion of how to determine this), and if we know its distance d , then we can calculate a_1 and a_2 from α_1 and α_2 using the small-angle formulae

$$\frac{a_1}{1 \text{ au}} = \frac{\alpha_1}{1''} \frac{d}{1 \text{ pc}}, \quad \frac{a_2}{1 \text{ au}} = \frac{\alpha_2}{1''} \frac{d}{1 \text{ pc}}. \quad [32.3]$$

The semi-major axis of the one-body problem is then $a = a_1 + a_2$. With a and the measured period P , we apply the generalized form of Kepler's third law [31.13] to find the combined mass $M_1 + M_2$ of the system. Together with the mass ratio M_2/M_1 , we then have sufficient information to solve for the individual masses of the stars.

Observing Spectroscopic Binaries

For spectroscopic binaries, we can use the Doppler shifts of spectral lines to measure the *radial velocity*¹ of each component. A *radial velocity curve* is a plot of these measurements as a function of time or orbital phase. The shape of the radial velocity curve provides information about the eccentricity: a sinusoidal curve indicates a circular orbit ($e = 0$; see Fig. 32.3), while non-sinusoidal curves are the hallmarks of eccentric orbits ($e > 0$).

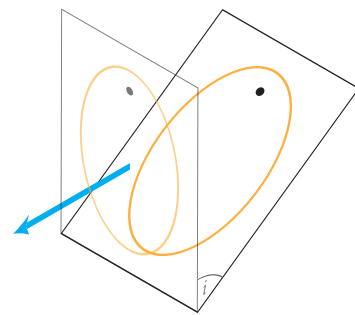


Figure 32.1: An elliptical orbit, with the center of mass at one focus marked by a black dot. The projection of the orbit on the sky plane is shown in faint, and the blue arrow indicates the line-of-sight. The angle between the orbit and sky planes defines the inclination i .

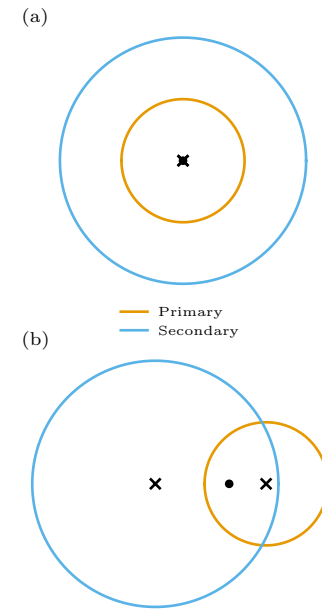


Figure 32.2: The apparent orbits of two binary systems, both having the same mass ratio $M_2/M_1 = 0.5$ but different eccentricities and inclinations. The crosses show the apparent focus of each orbit, and the black dot marks the center-of-mass of the system. A visual binary is being seen face-on if the apparent foci coincide; hence, we conclude that (a) is face-on but (b) is not. In fact, (a) is a circular ($e = 0$) system seen face-on, while (b) is an eccentric ($e = 0.6$) system seen at an inclination $i = 37^\circ$.

¹ The instantaneous orbital velocity projected along the line of sight

We can determine the mass ratio of the stars in a spectroscopic binary from the semi-amplitude² v_r of the radial velocity curves:

$$\frac{M_2}{M_1} = \frac{v_{r,1}}{v_{r,2}}. \quad [32.4]$$

If the system is circular, then the velocity semi-amplitudes are related to the semi-major axes, inclination and period via

$$2\pi a_1 = \frac{v_{r,1}}{\sin i} P, \quad 2\pi a_2 = \frac{v_{r,2}}{\sin i} P. \quad [32.5]$$

Combining this with Kepler's third law, we arrive at an expression for the combined mass of the system:

$$M_1 + M_2 = \frac{(v_{r,1} + v_{r,2})^3 P}{2\pi G \sin^3 i}. \quad [32.6]$$

If we don't know the inclination, this expression gives us only a lower bound on the combined mass (since $\sin i \leq 1$). However, if the system is also an eclipsing binary, the orbits must be close to edge-on ($i \approx 90^\circ$); then, we can find the combined mass and solve for the individual masses of the stars.

Observing Eclipsing Binaries

Eclipsing binaries are especially useful systems; not only do we know their inclination, we can also place constraints on the size and temperature of each star. Fig. 32.4 demonstrates the light curve of a typical eclipsing binary. If we measure the time difference between point a (when the primary begins to be eclipsed) and point b (when the primary completely disappears), and likewise between point a and point c (when the primary begins to reappear), then we can determine the radii of the two stars from

$$R_p = v_t \frac{t_b - t_a}{2}, \quad R_s = v_t \frac{t_c - t_a}{2}. \quad [32.7]$$

(the subscripts p and s denote the primary and secondary, respectively). Here, v_t is the *transverse velocity* of the stars relative to one another³. To obtain the effective temperatures, the fluxes during each phase of the eclipse (labeled 1–4 in see Fig. 32.4) are written as⁴

$$\begin{aligned} f_1 = f_3 &= \frac{\sigma}{d^2} \left[R_p^2 T_{\text{eff},p}^4 + R_s^2 T_{\text{eff},s}^4 \right], & f_2 &= \frac{\sigma}{d^2} \left[R_s^2 T_{\text{eff},s}^4 \right] \\ f_4 &= \frac{\sigma}{d^2} \left[R_p^2 T_{\text{eff},p}^4 + (R_s^2 - R_p^2) T_{\text{eff},s}^4 \right]. \end{aligned} \quad [32.8]$$

Solving these equations (with the radii determined using the previous expressions) yields the effective temperatures together with the distance d to the system.

²I.e., half the peak-to-peak amplitude.

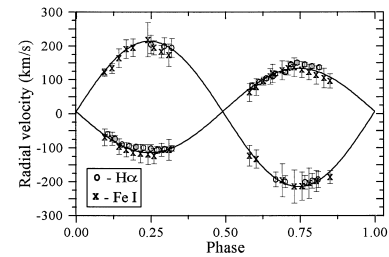


Figure 32.3: Radial velocity curves for the two components of SV Cam, a circular spectroscopic and eclipsing binary with $M_1 = 1.47 M_\odot$ and $M_2 = 0.87 M_\odot$. From Kjurkchieva et al. (2002, *A&A*, 386, 548).

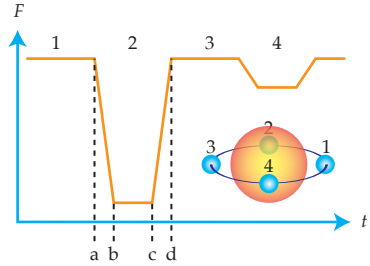


Figure 32.4: Schematic light curve for an eclipsing binary comprising a hot, smaller star (the primary) and a cool, larger star (the secondary). The inset figure shows the relative positions of the two stars at four orbital phases 1–4.

³For a circular eclipsing binary, $v_t = v_{r,1} + v_{r,2}$

⁴These equations come from application of eqn. [1.4] together with the Stefan-Boltzmann law [2.7]. Note that during phase 2, the primary is fully eclipsed and only the secondary contributes to the measured flux. Likewise during phase 4, the secondary is partially eclipsed by the primary.

Further Reading

Ostlie & Carroll, §§7.2, 7.3

33 Binary Evolution

Circularization and Synchronization

Observations of binary systems in clusters¹ reveal a lack of eccentric systems ($e > 0$) at short orbital periods (see Fig. 33.1). This is a consequence of *stellar tides*, which gradually transfer energy and angular momentum from the orbits to the individual stars. These tides, which are strongest for close (and hence short-period) binaries, ultimately leads both to the *circularization* of the orbits ($e \rightarrow 0$), and to the *synchronization* of the stars' rotation (such that the rotation period of each equals the orbital period P).

The Roche Model

To determine the shapes of stars in a circularized and synchronized binary system, we can use an approach developed originally by the astronomer Édouard Roche. In this so-called *Roche model*, we approximate the stars' gravitational potentials as arising from a pair of point masses. In the frame of reference co-rotating with the stars, the acceleration of an at-rest test particle can then be written as $\mathbf{a} = -\nabla\Phi_{\text{eff}}$, where

$$\Phi_{\text{eff}}(\mathbf{r}) = -\frac{GM_1}{|\mathbf{r} - \mathbf{r}_1|} - \frac{GM_2}{|\mathbf{r} - \mathbf{r}_2|} - \frac{1}{2}|\mathbf{r} \times \Omega|^2 \quad [33.1]$$

is the *effective potential* at position coordinate \mathbf{r} . Here \mathbf{r}_1 and \mathbf{r}_2 are the position coordinates of the primary and secondary stars, respectively, while Ω is the angular velocity vector of the system². On the right-hand side of this expression, the first two terms represent the gravitational potentials of the two stars, while the third term is a centrifugal potential.

The surfaces of constant effective potential define the level (horizontal) surfaces of the binary system, and surface of each star lies on one of these equipotentials. As shown in Fig. 33.2, the equipotentials are spherical close to the center of each star, but become distorted further away. Each star has a special equipotential known as a *Roche lobe*, which touches the L_1 Lagrange point³ of the system.

Roche Lobe Overflow

If a star expands to fill its Roche lobe, it will begin to spill mass onto its companion through the L_1 point. This *Roche-lobe overflow* (RLOF) can have a significant impact on the evolution of the stars and their orbits. When the overflow occurs during the main-sequence phase of the donor (overflowing) star, we refer to the mass transfer as *case A*; during the RGB phase it's *case B*; and during the AGB it's *case C*.

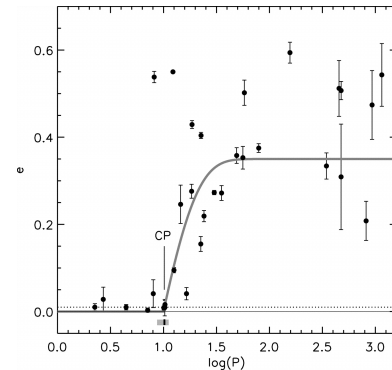


Figure 33.1: Scatter plot of eccentricity e versus orbital period P (in days) for binary systems in the open cluster M35. Note how systems with $P \lesssim 10$ d are close to circular. From Meibom & Mathieu (2005, *ApJ*, 620, 970).

¹ Remember that stars in clusters all have the same age.

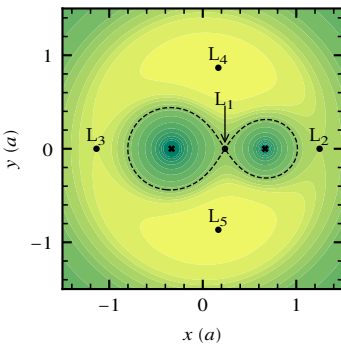


Figure 33.2: Contour plot of the effective potential Φ_{eff} in the orbital plane, for a circularized and synchronized binary system with a mass ratio $M_2/M_1 = 0.5$. The black crosses mark the centers of each star (the more-massive star is on the left), and the black dots indicate the Lagrange points. The Roche lobe of each star, shown by the dashed black contour, intersects the L_1 point.

² This vector points along the rotation axis, and has magnitude $|\Omega| = 2\pi/P$.

³ This is the point on the line between the two stars (but not necessarily at the center of mass) where effective potential shows a saddle point, and the acceleration \mathbf{a} vanishes. The L_1 point is marked in Fig. 33.2, together with the four other Lagrange points where \mathbf{a} vanishes.

Conservative Mass Transfer

Let's consider the special case of RLOF with *conservative mass transfer*, meaning that all of the mass and angular momentum lost by the donor star is gained by the recipient star. With the further assumption that the orbits remain circular, the rate-of-change of semi-major axis is found⁴ as

$$\frac{\dot{a}}{a} = -2 \frac{\dot{M}_2}{M_2} \left(1 - \frac{M_2}{M_1} \right). \quad [33.2]$$

The corresponding rate-of-change of the period is, from Kepler's third law,

$$2 \frac{\dot{P}}{P} = 3 \frac{\dot{a}}{a}. \quad [33.3]$$

Let's assume⁵ that the primary star is the donor ($\dot{M}_1 < 0$) and the secondary star is the recipient ($\dot{M}_2 = -\dot{M}_1 > 0$). Then, the above expressions show that the orbits will shrink and the period get shorter, if $M_2 < M_1$ — and vice versa. Put differently, mass transfer that tends to make the two stars closer in mass will also make them physically closer.

As the separation of the stars changes, the size of their Roche lobes will also change. The average radius⁶ of the primary Roche lobe can be well approximated by the formula

$$R_{L,1} \approx 0.49a \left(\frac{M_1}{M_1 + M_2} \right)^{1/3}. \quad [33.4]$$

Taking the time derivative, we find after some algebra that

$$\frac{\dot{R}_{L,1}}{R_{L,1}} = -2 \frac{\dot{M}_2}{M_2} \left(1 - \frac{5}{6} \frac{M_2}{M_1} \right). \quad [33.5]$$

With our assumption that $\dot{M}_2 > 0$, we can see that the primary Roche lobe will shrink with time ($\dot{R}_{L,1} < 0$) when $M_2/M_1 < 6/5$. The shrinkage leads to a positive feedback loop: as $R_{L,1}$ gets smaller, the mass loss from the donor star grows⁷, driving up \dot{M}_2 and accelerating $\dot{R}_{L,1}$.

Unless halted by M_2/M_1 rising above $6/5$, this *unstable mass transfer* ultimately deposits so much material on the recipient star that it, too, overflows its Roche lobe. The binary system then consists of a pair of stellar cores orbiting inside a *common envelope*. Friction between the stars and the envelope causes the stars to spiral in toward each other. The release of energy by this inspiral eventually drives off the envelope, leaving behind a very close binary system comprising the stripped donor and its companion.

⁴ To derive this result, take the time derivative of eqn. [31.10] of *Handout 31*, with $e = 0$, $\dot{M}_1 = -\dot{M}_2$ and $\dot{L} = 0$.

⁵ Our analysis doesn't rely on this assumption, since the labels 'primary' and 'secondary' are arbitrary; but it's easier to interpret results if we fix the signs of \dot{M}_1 and \dot{M}_2 .

⁶ Defined in an equal-volume sense.

⁷ The increasing mass loss from the donor, as its Roche lobe shrinks, can be understood with an analogy to a water-filled balloon: as the balloon shrinks, the water spurts out of its mouth.

Further Reading

Ostlie & Carroll, §18.1.

34 Nova

Tycho's Nova

In 1572, the Danish astronomer Tycho Brahe observed a new star in the constellation of Cassiopeia (see Fig. 34.1). In the following year, he described his observations in the report *De Nova Et Nullius Aevi Memoria, A Mundi Exordio Prius Conspecta Stella*¹, and the term *nova* entered into the astronomical lexicon to refer to stars that show sudden and dramatic brightening episodes.

Types of Novae

Nowadays, we divide novae (the plural of 'nova') into four different categories:

- *classical novae*, where the star brightens over a few days to reach a peak luminosity $L \approx 10^4 - 10^5 L_{\odot}$, and then fades away over timescales of a few months.
- *recurrent novae*, where the star passes through multiple episodes each resembling a classical nova. The timescales for recurrence extend from years through to centuries.
- *dwarf novae*, where the star passes through multiple brightenings, but with a much lower peak luminosity ($L \approx L_{\odot}$) than recurrent novae. The timescales for recurrence extend from days to decades.
- *supernovae*, where the star brightens over a couple of weeks to reach a peak luminosity $L \approx 10^{11} L_{\odot}$, and then fades away over timescales of many months.

This handout focuses on the first three categories; we'll discuss supernovae (of which Tycho's nova was an instance) in a later handout.

Cataclysmic Variables

Classical, recurrent and dwarf novae all arise in a special class of binary star system: *cataclysmic variables*. These consist of a white dwarf that accretes matter from a companion star that's in an earlier evolutionary phase (e.g., main sequence or RGB) and undergoing Roche-lobe overflow (see *Handout 33*). Because the material lost by the donor has significant angular momentum, it doesn't fall directly on the white dwarf, instead forming an accretion disk (see Fig. 34.2).

Classical and recurrent novae occur due to the steady build-up of accreted hydrogen in a surface layer on the white dwarf. As this layer accumulates, it reaches sufficient temperatures² near its lower boundary for hydrogen burning to commence — initially by the pp chain, but then quickly transitioning to the CNO cycle. The ignition takes place under degenerate conditions, and so there's a runaway (reminiscent of the helium flash; see *Handout 24*) that leads to an enormous spike in the star's hydrogen-burning luminosity L_{HI} .

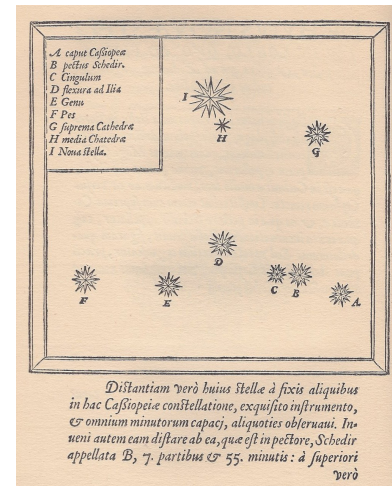


Figure 34.1: Sketch of the constellation Cassiopeia, drawn by Tycho Brahe to show the position of the new star (marked *I Noua stella*). From *De Nova....*

¹ Loosely translated, "Concerning the Star, new and never before seen in the life or memory of anyone".



Figure 34.2: Artist's impression of a cataclysmic variable, showing a red giant (right) undergoing Roche-lobe overflow and transferring mass into the accretion disk of a white dwarf (left). Image credit: Dr. Mark Garlick.

² The hydrogen layer heats up when it is compressed by the white dwarf's strong surface gravity.

During this phase, the star's surface luminosity L exceeds the *Eddington luminosity*³

$$L_{\text{edd}} = \frac{4\pi GMc}{\kappa}. \quad [34.1]$$

As a consequence, the outermost layers of the WD are no longer gravitationally bound, and are driven outward in a *super-Eddington wind*. After a couple of weeks (depending on the initial thickness of hydrogen layer), the material in the burning region transitions from degenerate to classical. This marks the beginning of the *super-soft source*⁴ (SSS) phase — an extended period (months-to-years) where the remaining hydrogen in the surface layer burns into helium under stable conditions.

After the hydrogen is exhausted, the white dwarf resumes accretion, building up a fresh hydrogen layer. Eventually, it will undergo another nova outburst. However, the timescale between outbursts can be very long, especially if the accretion rate is slow and/or the white dwarf mass is low. This explains the difference between classical and recurrent novae: they are both intrinsically the same phenomenon, but in the former the timescale between outbursts is so long that astronomers have only ever seen a single one. Of course, a classical nova will be re-categorized as a recurrent nova if and when it shows a second outburst.

Figures 34.3 and 34.4 illustrates a typical nova outburst for a massive CO white dwarf. The WD accretes hydrogen-rich material from its companion at a rate $\dot{M} = 10^{-9} M_{\odot}/\text{yr}$, until this fresh fuel ignites. The hydrogen-burning luminosity initially spikes up to $L_H \approx 10^9 L_{\odot}$, although most of this energy is reabsorbed in the outer parts of the hydrogen layer. Because the surface luminosity $L \approx 10^4 L_{\odot}$ exceeds the Eddington luminosity, a strong super-Eddington wind with $\dot{M} \approx -10^{-4} M_{\odot}/\text{yr}$ occurs. After a couple of weeks, the unstable burning transitions to stable burning, and the star enters a year-long SSS phase with $L \approx L_H \approx 10^4 L_{\odot}$.

Dwarf Novae

With their much smaller peak luminosities, dwarf novae arise from a different process. Although there remain many uncertainties, the current best narrative is that their outbursts (which are much less energetic than classical or recurrent novae) arise due to a sudden increase in the accretion rate onto the white dwarf, with the consequent rapid release of gravitational energy.

Further Reading

Kippenhahn, Weigert & Weiss, §36.1; Ostlie & Carroll, §§15.2; Prialnik, §§10.5,11.6.

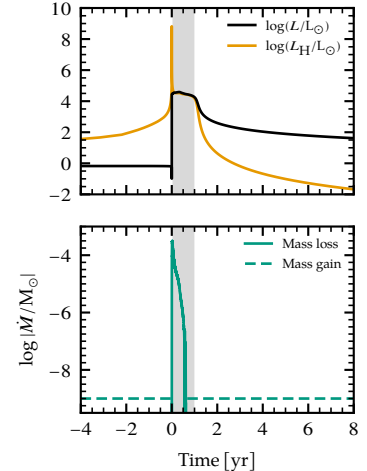


Figure 34.3: Plot of the surface luminosity L and hydrogen-burning nuclear luminosity L_H (top), and the mass loss/gain rate $|\dot{M}|$ (bottom), as a function of time for a *MESA* model of a $M = 1.12 M_{\odot}$ CO white dwarf as it passes through a nova outburst. The time zero-point is set to peak L_H , and the supersoft source phase is highlighted in gray.

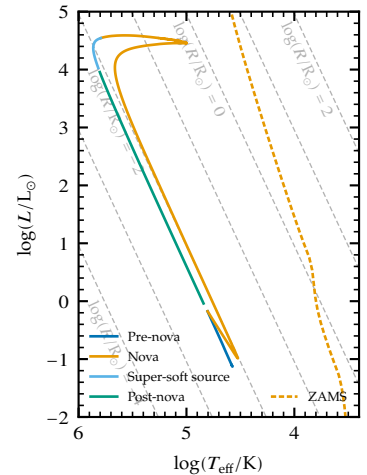


Figure 34.4: Track in the Hertzsprung-Russell diagram for one nova cycle of the WD shown in Fig. 34.3.

³ Defined by setting the outward acceleration due to radiation pressure, $g_{\text{rad}} \equiv \kappa F_{\text{rad}}/c$, equal to the inward acceleration due to gravity, g .

⁴ So named because during this phase, the high effective temperature of the WD (between 10^5 K and 10^6 K) means that it emits in the extremely soft ($\lesssim 0.1 \text{ keV}$) part of the X-ray spectrum.

35 Thermonuclear Supernovae

Classifying Supernovae

The *nova stella* observed by Tycho (see Fig. 34.1) was in fact a supernova. Supernovae are among the most energetic phenomena in the Universe, reaching luminosities $L \approx 10^{11} L_\odot$ and involving total energies on the order $\sim 10^{51}$ erg. We classify them on the basis of the absorption lines seen in their spectrum (see Fig. 35.1); Tycho's supernova was a type Ia, arising when the accretion of material onto a white dwarf triggers a thermonuclear explosion¹.

The Chandrasekhar Limit

As the mass of an accreting white dwarf increases, the degenerate EOS [24.1] causes its radius to shrink and central density to rise according to the approximate scalings

$$R \propto M^{-1/3}, \quad \rho_c \propto M^2 \quad [35.1]$$

(these follow from the same analysis used at the beginning of *Handout 24*). Eventually, the Fermi energy of the free electrons,

$$\mathcal{E}_{F,c} \propto \rho_c^{2/3} \propto M^{4/3}, \quad [35.2]$$

becomes comparable to their rest-mass energy $m_e c^2$, meaning that we need to update the EOS to account for relativistic effects².

For simplicity, let's focus on the completely degenerate ($\mathcal{E}_F \gg k_B T$) and completely relativistic ($\mathcal{E}_F \gg m_e c^2$) limits. Then, we follow the same steps as when deriving eqn. [16.11], with the one exception that we adopt a particle velocity $v(p) = c$ instead of $v(p) = p/m_e$. This leads to a free electron pressure

$$P_e = \left(\frac{3}{\pi} \right)^{1/3} \frac{hc}{8} n_e^{4/3}, \quad [35.3]$$

and so (assuming the electrons dominate the total pressure) the EOS becomes

$$P \propto \rho^{4/3}. \quad [35.4]$$

Initially, this revised expression applies only at the center of the WD, where the density is highest; the rest of the star follows the non-relativistic EOS [24.1]. However, as further mass is added to the WD, the relativistic EOS [35.4] applies throughout more and more of the interior.

Eventually, the entire star follows eqn. [35.4], and the structure of the WD has become a polytrope with index $n = 3$. Combining the EOS with the polytropic scalings. [24.2] yields the result

$$M \propto R^0; \quad [35.5]$$

¹ Type Ib, Ic and II supernovae do not arise from white dwarfs, but from the core collapse of a massive star; they will be discussed in a later handout.

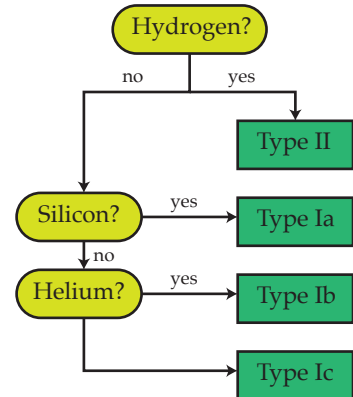


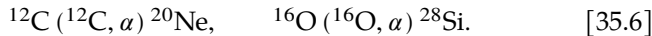
Figure 35.1: Flow chart for the classification of supernovae, on the basis of whether absorption lines from various elements can be seen in the spectrum. Note that some type Ic supernovae do show silicon lines, but they are much weaker than in type Ia.

² Remember that these were ignored in *Handout 16*.

that is, the mass is independent of the radius. In fact, the mass is given by the constant of proportionality in this expression, which depends only on the composition of the WD and physical constants. Therefore, we are led to conclude that a WD in which the free electrons are both completely degenerate and completely relativistic *throughout* can only have one possible mass: the so-called *Chandrasekhar mass* M_{ch} , which evaluates to about $1.4 M_{\odot}$ for the composition of a typical carbon-oxygen WD.

Exceeding the Limit

If we add even a tiny amount of mass to a WD that's already at the Chandrasekhar limit, then it's no longer possible for the star to remain in hydrostatic equilibrium; instead, it begins to collapse. During this initial collapse, compressional heating raises the temperature in the interior to the point $T \gtrsim 10^9$ K where new thermonuclear reaction sequences become possible. In a CO white dwarf, the key reactions are carbon and oxygen burning to produce neon- ^{20}Ne ³ and silicon-28, respectively:



The α particles released lead to a sequence of alpha-capture side reactions that transform the silicon-28 into heavier elements through to nickel-56. All of these reactions take place under degenerate conditions, and encompass essentially the whole WD; therefore, there is a rapid and enormous release of energy that suffices completely to destroy the star.

Supernovae for Distance Measurement

Observations of the light curves of many type Ia supernovae reveal they share a similar morphology (see Fig. 35.2). In the 1970's, a number of astronomers noticed that the rate of dimming after maximum brightness is related to the absolute magnitude (or alternative, luminosity) at the maximum. In the 1990's, Mark Phillips placed this correlation on a quantitative footing with the empirical relation

$$M_{\text{max}}(B) = -21.726 + 2.698\Delta m_{15}(B). \quad [35.7]$$

Here, $M_{\text{max}}(B)$ is the maximum absolute magnitude of the supernova in the B-band; and Δm_{15} is the change in the apparent magnitude in the B-band, over the 15 days after the maximum. Using this *Phillips relation*, we can determine the absolute magnitudes of type Ia supernovae from their light curves, and thereby measure their distances⁴.

Further Reading

Kippenhahn, Weigert & Weiss, §36.1; *Ostlie & Carroll*, §§15.2; *Prialnik*, §§10.5, 11.6.

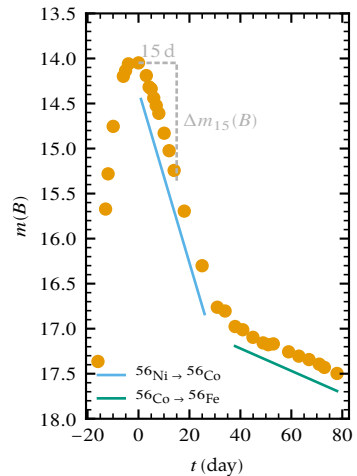


Figure 35.2: Light curve in the B -band (corresponding to wavelengths around 4450 Å) for the supernova 2002bo. The $t = 0$ point is defined as maximum brightness, when $m_B \approx 14.0$. The dashed lines indicate how the 15-day brightness change, $\Delta m_{15}(B)$, is measured. The solid lines indicate the primary energy source powering the supernova's luminosity; at early times ($t \lesssim 30$ d), this source is the radioactive decay of ^{56}Ni into ^{56}Co , whereas at later times it is the decay of ^{56}Co into ^{56}Fe . Data from Ganeshalingam et al. (2010, *ApJS*, **190**, 418).

³ This is the origin of the neon used in fluorescent light displays; so, we should thank supernovae for the city of Las Vegas!

⁴ The careful measurement of supernova distances, using this technique, revealed that the Universe's expansion is accelerating. This amazing discovery was acknowledged in the 2011 Nobel Prize for Physics).

36 Intermediate-Mass Stellar Evolution

Main-Sequence Structure

Our discussion of stellar evolution has so far focused mostly on the case of the Sun. As we saw in *Handout 29*, however, initial mass can have a significant impact on the evolutionary narratives of stars. In this handout, we take a look at these narratives for *intermediate-mass stars*, in the range $1.4 M_{\odot} \lesssim M \lesssim 10 M_{\odot}$.

On the main sequence, a key difference between intermediate-mass stars and stars like the Sun is the positioning of convection zones. As shown in *Handout 14*, stars with masses $M \gtrsim 1.4 M_{\odot}$ have a convective core and a radiative envelope — the opposite of the case for the Sun. This has important consequences for the stars' composition profiles as they evolve across the main sequence. For solar-like stars, the hydrogen mass fraction varies smoothly from the center (where it is most depleted, due to nuclear burning) out into the envelope (where it remains unchanged from its initial value, $X \approx 0.7$). Whereas for intermediate-mass stars, then hydrogen mass fraction is spatially uniform throughout the core, due to rapid mixing by the convection; then rises sharply over a narrow inhomogeneous zone; and is again spatially uniform and at its initial value throughout the envelope. Fig. 36.1 contrasts these features for models of a $5 M_{\odot}$ main-sequence star star and the present-day Sun.

Post-Main Sequence Evolution

Toward the end of the main sequence phase of an intermediate-mass star, the depletion of hydrogen throughout the entire convective core means that the hydrogen-burning nuclear luminosity L_H is unable to keep pace with the surface luminosity L . To make up for the luminosity deficit $L - L_H$, the star undergoes a short-lived Kelvin-Helmholtz contraction, evolving to the blue in the Hertzsprung-Russell diagram in a feature known as the *Heney hook* (see Fig. 36.2). This contraction has the side-effect of heating the inhomogeneous zone surrounding the core, to the point where it starts to burn hydrogen via the CNO cycle. This marks the end of main sequence.

During the post-MS phase, the hydrogen-burning shell generates more energy than the surface can radiate (i.e., $L_H > L$). The excess energy is re-absorbed by the stellar envelope situated above the shell, causing it to expand and making the star evolve across to the red side of the HR diagram. When it reaches low effective temperatures, the luminosity of the star begins to climb, and its evolutionary track turns vertically upward in the HR diagram.

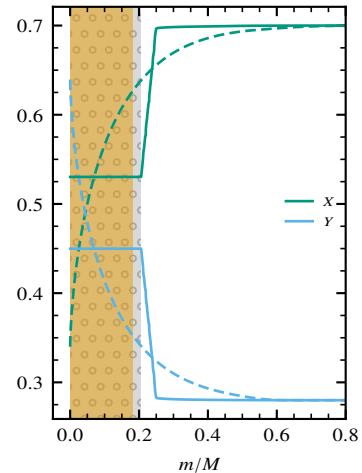


Figure 36.1: The hydrogen (X) and helium (Y) mass fractions plotted as a function of fractional interior mass m/M , for a $5 M_{\odot}$ MESA model (solid) and the Sun-similar model (dashed; see Fig. 4.1). The age of the $5 M_{\odot}$ model is chosen so that it has the same average mass fractions as the Sun-similar model. The orange-shaded region indicates the stellar core of the $5 M_{\odot}$ model, where fusion reactions are converting hydrogen into helium; the overlapping gray-shaded/dotted region indicates the core convection zone.

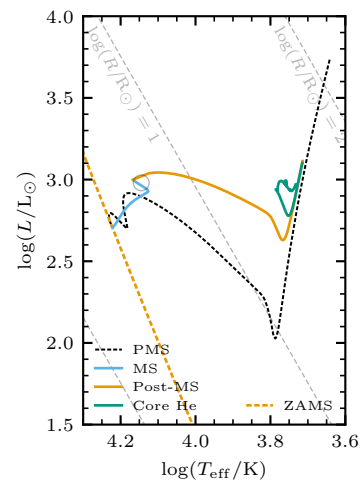


Figure 36.2: Evolutionary track in the Hertzsprung-Russell diagram for a $5 M_{\odot}$ MESA model, spanning the pre-main sequence (PMS) main sequence (MS), post-MS and core helium burning phases. The gray circle highlights the Heney hook portion of the MS phase.

Helium Ignition

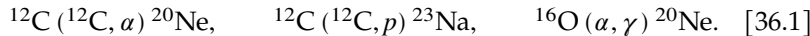
The next phase in the evolution of an intermediate-mass star is the ignition of helium burning via the 3α reaction [24.4]. How this proceeds depends on the equation-of-state in the star's core — and that in turn depends on the mass of the star. Recall that at low masses the free electrons in the core are very degenerate, and ignition leads to runaway burning in a helium flash (see *Handout 24*). Toward higher stellar masses, however, the lower central densities mean that the free electrons behave more classically¹, and the flash becomes less dramatic. Above the threshold $M \approx 2.3 M_\odot$, the flash disappears altogether — helium ignition begins at the center of the star, in a controlled, steady manner. This can be seen in Fig. 36.3 and 36.4, for the same $5 M_\odot$ model plotted previously.

Without a flash, the expansion of the core during helium ignition is relatively modest; therefore, the reductions in the shell-burning luminosity L_H and surface luminosity L are correspondingly modest. Fig. 36.2 shows that $\log(L/L_\odot)$ drops by ≈ 0.35 across He ignition in the $5 M_\odot$ model; this is significantly less than the ≈ 1.8 reduction seen in Fig. 26.1 during the He flash of the solar model.

Later Evolution

Upon completion of core helium burning, intermediate-mass stars in the interval $1.4 M_\odot \lesssim M \lesssim 7 M_\odot$ evolve up the asymptotic giant branch in much the same manner as their lower-mass cousins (*Handout 26*). Near the tip of the AGB they encounter thermal pulses (*Handout 27*), and eventually shed their remaining hydrogen envelopes in a superwind to become a CO white dwarf (*Handout 28*).

In the narrow interval $7 M_\odot \lesssim M \lesssim 10 M_\odot$, intermediate-mass stars follow a slightly different path. On the AGB their CO cores reach sufficiently high temperatures ($T \approx 5 \times 10^8$ K) for carbon burning to commence via the reactions



(the third reaction mops up the α particle produced by the first). The net effect of these reactions is to transform the core into a mixture of oxygen-16 ($\approx 65\%$ by mass), neon-20 ($\approx 30\%$) and sodium ($\approx 5\%$). After the loss of their envelope in a superwind, these stars (known as *super-AGB stars*) become oxygen-neon-sodium (ONeNa) white dwarfs.

Further Reading

Kippenhahn, Weigert & Weiss, §§31,34.8

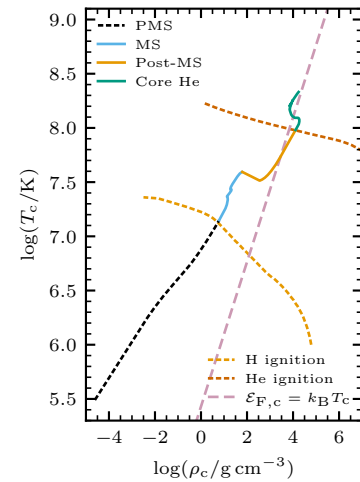


Figure 36.3: Path followed in the $\log \rho_c$ - $\log T_c$ plane for the $5 M_\odot$ *MESA* model shown in Fig. 36.2. The diagonal dashed line shows where $\mathcal{E}_{F,c} = k_B T_c$, and divides the plane into classical (left) and degenerate (right) regimes. The light (dark) orange dotted line shows the locus in the plane where hydrogen (respectively, helium) ignites.

¹ This trend can be seen in Fig. 9.2; note how, with increasing stellar mass, the tracks in the $\log \rho_c$ - $\log T_c$ plane are displaced toward lower densities.

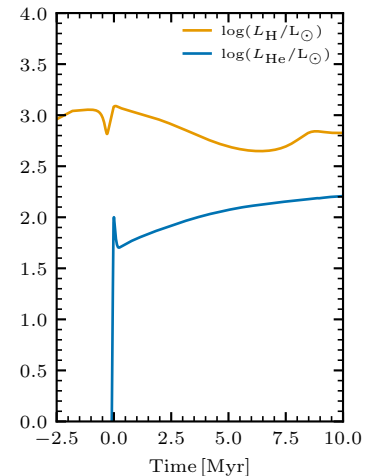


Figure 36.4: The hydrogen-burning component of the nuclear luminosity L_H , and the corresponding helium-burning component, L_{He} , plotted as a function of stellar age since initial helium ignition for the $5 M_\odot$ model shown in Fig. 36.2. Compare against Fig. 24.3.

37 High-Mass Stellar Evolution

Evolution through Helium Burning

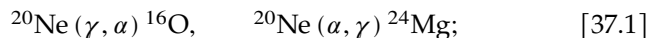
High-mass stars ($M \gtrsim 10 M_{\odot}$) share many similarities with the intermediate-mass stars discussed in Handout 36. On the main sequence, their internal structure is characterized by a convective core and a radiative envelope. Toward the end of the main-sequence phase, their evolution in the Hertzsprung-Russell diagram turns to the blue in a characteristic Henyey hook; and after hydrogen is exhausted in the core, they evolve rapidly to the red. Fig 37.1 shows this behavior for a $16 M_{\odot}$ model; for comparison, the $5 M_{\odot}$ model from Handout 36 is also plotted.

On the main-sequence, the high-mass star is almost a factor of 100 times more luminous than the intermediate-mass star. This is a direct consequence of the steep mass-luminosity relation $L \propto M^{3.5}$ discussed in Handout 21. After the main sequence, this difference persists because both stars evolve to the red at approximately constant luminosity. To maintain its huge luminosity even when its effective temperature drops down to ≈ 3500 K, the high-mass star puffs up to an immense size, with its radius approaching $10^3 R_{\odot}$. Evolved high-mass stars like this are known as *red supergiants* (RSGs).

Massive Stars Beyond Helium Burning

Helium ignites in RSGs under non-degenerate conditions, and so — like intermediate-mass stars with $M \gtrsim 2.4 M_{\odot}$ — there is no helium flash. After helium burning, the evolution of high-mass stars begins to diverge from that of intermediate-mass stars. They embark on a sequential burning process whereby the core exhausts one nuclear fuel; contracts and heats up; and then ignites the next fuel in the sequence. Table 37.1 summarizes the ignition temperature and duration of each burning stage.

Carbon burning follows helium burning, proceeding via the reactions introduced in eqn. [36.1]. Next comes neon burning,



the first (endothermic) reaction is an example of *photodisintegration*, and arises due to an abundance of energetic photons at the high burning temperatures. Neon burning is followed by oxygen burning¹,



Subsequent burning stages proceed by α -capture reactions, and steadily convert the silicon to heavier elements:

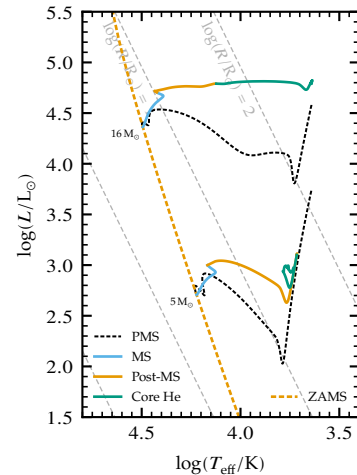
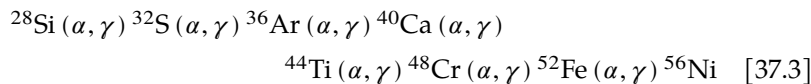


Figure 37.1: Evolutionary track in the Hertzsprung-Russell diagram for $16 M_{\odot}$ and $5 M_{\odot}$ MESA models, spanning the pre-main sequence (PMS) main sequence (MS), post-MS and core helium burning phases. The tracks are labeled at the ZAMS with the initial stellar mass.

Fuel	Ignition $T/10^9$ K	Duration
${}^1\text{H}$	0.035	11 Myr
${}^4\text{He}$	0.17	1.3 Myr
${}^{12}\text{C}$	0.63	2.1 kyr
${}^{20}\text{Ne}$	1.3	3 yr
${}^{16}\text{O}$	2.4	9 mo
${}^{28}\text{Si}$	4.1	1 wk

Table 37.1: Summary of the different burning stages in the life of the $16 M_{\odot}$ model plotted in Fig. 37.1, indicating the ignition temperature and duration of the stage.

¹ The reason why oxygen burning follows neon burning, even though oxygen has the smaller mass number, is that ${}^{16}\text{O}$ is a double-magic nucleus with 8 protons and 8 neutrons; therefore, it is unusually stable and difficult to burn.

The α particles required by these reactions are produced by photo-disintegration of other ^{28}Si nuclei. Although this sequence suggests that ^{56}Ni is the final product, in fact neutron captures² along the way mean that the core ends up composed predominantly of ^{56}Fe . This is the most stably bound of all isotopes, and no further nuclear energy can be extracted: the burning sequence has come to an end. As we shall see, an iron core inevitably collapses soon after its formation, triggering a supernova explosion.

Fig. 37.2 illustrates the progression of core burning from hydrogen through to iron for the $16 M_{\odot}$ model, plotting the central abundances of various isotopes as a function of time remaining until core collapse. Note how each burning phase is shorter than the previous one; this can also be seen from the duration data in Table 37.1. As the star exhausts a given fuel in the core, that fuel continues to burn in a shell around the core; therefore, the composition profile of the star at the instant of collapse resembles an onion, with nested shells of hydrogen, helium, carbon, neon, oxygen and silicon (going from surface inward) lying atop the iron core.

Neutrino Losses

During the later evolutionary stages of a high-mass star, a significant proportion of the energy release by nuclear reactions is converted to non-nuclear neutrinos and then lost from the star. This conversion involves the *pair-production process*, where a pair of photons with a total energy $> 1.02 \text{ MeV}$ ³ combine to form an electron and positron:

$$\gamma (\gamma, e^-) e^+. \quad [37.4]$$

The positron annihilates immediately with another free electron, almost always recreating a pair of photons. However, 1 in every 10^{19} annihilations a neutrino-antineutrino pair is produced instead:

$$e^+ (e^-, \nu_e) \bar{\nu}_e. \quad [37.5]$$

This pair then escapes the star without further interaction, representing a loss of at least 1.02 MeV of energy from where they were formed in the star.

From carbon burning onward, almost all energy released in the core by nuclear reactions is converted into these *pair neutrinos*. However, there's no noticeable effect on the star's surface luminosity, because the later burning stages are shorter than the Kelvin-Helmholtz timescale.

Further Reading

Kippenhahn, Weigert & Weiss, §§35.1,32.3,18.7; Ostlie & Carroll, §15.1; Prialnik, §9.9.

² Like the α particles, the neutrons come from photodisintegration of other nuclei.

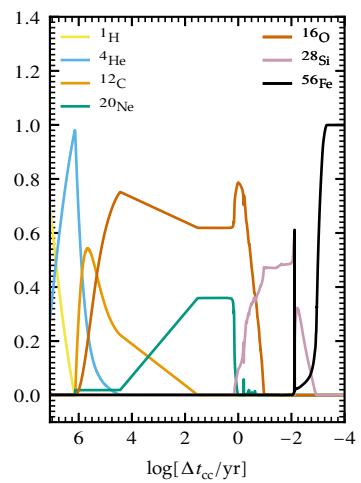


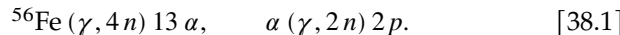
Figure 37.2: Central abundances of various isotopes during the evolution of the $16 M_{\odot}$ MESA model (Fig. 37.1), plotted as a function of time until core collapse Δt_{cc} . The sharp spike in the ^{56}Fe abundance is a numerical artifact.

³ This is just the rest mass of an electron and a positron.

38 Core-Collapse Supernovae

Initiating Core Collapse

As discussed in *Handout 37*, high-mass stars ($M \gtrsim 10 M_{\odot}$) are destined to burn all the way through to form an iron core. Soon (a matter of a day or so) after an iron core forms, it begins to collapse under the force of its own gravity. The collapse is initiated by a pair of important processes. First, as the core temperature rises toward 10^{10} K, photodisintegration begins to break the ^{56}Fe nuclei into α particles, and from there into protons and neutrons:



Second, at the very high densities found in the core, electron captures convert the protons liberated by photodisintegration into neutrons (a process known as *neutronization*):



Both processes abruptly decrease the pressure support of the core¹, initiating its collapse.

Collapse Dynamics

During the collapse, the inner part of the core contracts *homologously*, meaning that the velocity at any instant in time is proportional to the distance from the origin: $v \propto r$. At sufficient distances from the center, the homologous collapse velocity exceeds the local speed of sound, and the velocity transitions over to a free-fall profile $v^2 \propto 1/r$ (see Fig 38.1). As a result, the inner core (having a typical mass $\approx 1\text{--}2 M_{\odot}$) decouples from the outer core, leaving it behind.

A few tenths of a second after the start of the collapse, the density in the inner core becomes comparable to that of atomic nuclei, causing the equation-of-state to ‘stiffen’². The collapse is abruptly halted, and the inner core springs back a little. This *core bounce* launches a shock wave that begins to propagate outwards through the still-infalling outer core.

Supernova Explosion

As it travels outward, the shock wave heats and compresses the outer-core material that it passes through. This results in further photodisintegration and neutronization, which robs the shock of energy and causes it to stall³. However, the densities interior to the shock are so high that neutrinos formed in the inner core⁴ cannot escape from the star, and are instead re-absorbed below the shock. This injects sufficient energy that, after ~ 0.5 s, the shock re-energizes and resumes its march out through the star. As it passes through the outer core and

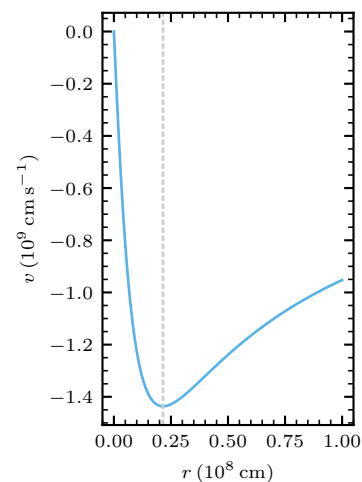


Figure 38.1: A typical velocity profile at the center of a massive star during core collapse. The vertical dotted line marks the boundary between the inner core (to the left; $v \propto r$) and the outer core (to the right; $v \propto 1/\sqrt{r}$).

¹ Photodisintegration decreases the radiation pressure, because it consumes photons; while neutronization decreases the gas pressure, because it consumes free electrons.

² I.e., the material becomes much more resistant to compression. This is a consequence of the repulsive nature of the strong nuclear force at short ranges.

³ Another important effect is the creation of new elements via capture of the neutrons produced by neutronization. Unlike the s-process neutron capture that occurs on the AGB (see *Handout 26*), the neutron capture rate in this instance is so rapid that there is little time for radioactive decay to occur between captures. This *rapid* or *r*-process neutron capture is responsible for creating all of the elements beyond ^{209}Bi .

⁴ These neutrinos are a result of further neutronization, as described by eqn. [38.2].

envelope of the star, the shock sends the material outward with a velocity in excess of the star's escape velocity — resulting in *core-collapse supernova* explosion.

Core-collapse supernovae are classified as type Ib, Ic or II, depending on the absorption lines in their spectra (see *Handout 35*). If the progenitor star still retains its hydrogen envelope, it produces a type II supernova. However, if it lacks this envelope (e.g., due to wind mass-loss during its evolution), it produces a type Ib. If it also lacks a helium envelope, it produces a type Ic.

Unlike type Ia supernovae, which are powered by thermonuclear reactions, the energy source in core-collapse supernovae is gravitational. We can estimate the total energy budget by calculating the gravitational energy released as the inner core collapses from its initial radius $R_{\text{c},\text{i}}$ to its final radius $R_{\text{c},\text{f}}$:

$$\Delta\Omega \approx \frac{GM_{\text{c}}^2}{R_{\text{c},\text{f}}} - \frac{GM_{\text{c}}^2}{R_{\text{c},\text{i}}} \quad [38.3]$$

With a core mass $M_{\text{c}} \sim 1 M_{\odot}$, and typical values $R_{\text{c},\text{i}} \sim 10^9 \text{ cm}$ and $R_{\text{c},\text{f}} \sim 10^6 \text{ cm}$, the energy release is $\Delta\Omega \approx 3 \times 10^{53} \text{ erg}$. Almost all of this energy is in the form of neutrinos, with about 1% absorbed to re-energize the shock wave (the remaining neutrinos escape into space). Of this 1%, corresponding to a few times 10^{51} erg , most ends up as kinetic energy of the ejecta; however, around 1% in turn⁵ is converted into electromagnetic radiation, and is responsible for the immense peak luminosities $\sim 10^9 L_{\odot}$ of core-collapse supernovae.

Gamma-Ray Bursts

In the 1960's, the US government initiated the *Vela* satellite program, to look for gamma rays originating from atmospheric nuclear weapon tests. Although none were found, the satellites discovered a new kind of astrophysical phenomenon: brief, intense flashes of gamma rays known as *gamma-ray bursts* (GRBs). The distribution of GRBs is uniform on the sky (see Fig. 38.2), indicating that they must originate from outside the Milky Way galaxy. In fact, we now believe that 'long' GRBs (with a duration of a few seconds) originate in core-collapse supernovae of rapidly rotating stars⁶. The rapid rotation focuses the explosion energy along a polar jet, and if this jet is directed toward Earth, we observe an intense flash of gamma rays as the jet breaks through the stellar surface.

Further Reading

Kippenhahn, Weigert & Weiss, §§36.3,36.4; Ostlie & Carroll, §15.3, Prialnik, §§10.2,10.3.

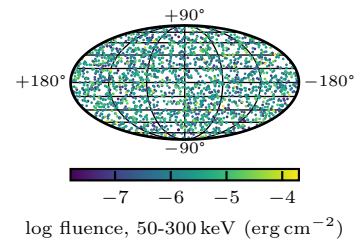


Figure 38.2: Distribution of GRBs on the sky, plotted in galactic coordinates using a homographic (equal-area) projection. The data are from the Burst and Transient Source Experiment (BATSE) instrument on board the *Compton Gamma Ray Explorer* satellite. The fluence values indicate the total amount of energy received, per unit area, during the burst.

⁵I.e., a few times 10^{49} erg .

⁶By contrast, 'short' GRBs (with durations of less than a second) originate from merging neutron stars.

39 Neutron Stars

Formation Process

Recall from *Handout 38* that the collapse of a massive star, at the end of its life, abruptly halts when the density of the inner core becomes comparable to that of atomic nuclei. The subsequent ‘bounce’ of the inner core launches a shock wave that ejects the outer core and envelope in the supernova explosion. The inner core is left behind as a hot ($T \approx 10^{10}$ K), massive ($M \approx 1.4 M_{\odot}$), compact ($R \approx 10$ km) object comprised of the densest matter found in the Universe — a *neutron star*.

Internal Structure

Figure 39.1 sketches the typical internal structure of a neutron star. Going from the surface to the center, the density increases by around 15 orders of magnitude, and this leads to important state changes in the material making up the star. The outermost layer, known as the ‘ocean’ due to its fluid nature, is mainly composed of light elements such as hydrogen and helium, with densities extending up to around 10^6 g cm $^{-3}$. Beneath the ocean lies a crystalline crust, composed of heavier nuclei arranged in a regular lattice. In the outer crust, these nuclei are surrounded by free electrons; but with increasing depth and density, these electrons are absorbed by protons in the nuclei via neutronization reactions (see eqn. [38.2]), resulting in ever-more neutron-rich isotopes. Eventually, the nuclei become so neutron-rich that the neutrons can no longer remain bound by the strong force, and they are squeezed out to establish a population of free neutrons. This transition begins at the *neutron drip* density of 4.3×10^{11} g cm $^{-3}$, which marks the boundary between the outer and inner crust.

The inner crust is a mixture of nuclei (still arranged in a lattice), free electrons and free neutrons, with the neutrons becoming more dominant as the density increases. Approaching the crust-core boundary, the lattice spacing becomes comparable to the size of the nuclei, and the lattice dissolves to form a mixture of free protons, electrons and neutrons. Toward ever higher-densities in the core (which makes up most of the star’s ≈ 10 km radius), the ratio of neutrons:protons:electrons approaches 8:1:1, and it is this neutron-dominated fluid that gives neutron stars their name. Once the density exceeds 10^{15} g cm $^{-3}$, in the inner core, the neutrons are moving so close to the speed of light¹ that their relativistic mass begins to exceed the rest mass of lower-mass hyperons such as Λ , Σ and Δ particles. When this happens, the neutrons begin to transform into these particles via a process of *hyperonization*.

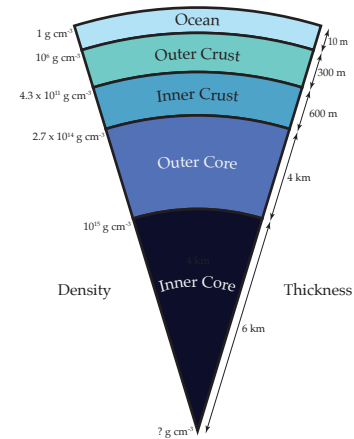


Figure 39.1: Sketch of the internal structure of a typical neutron star, showing the division into different regions. The density at the region boundaries is shown on the left, and the thickness of the regions (not plotted to scale) is shown on the right.

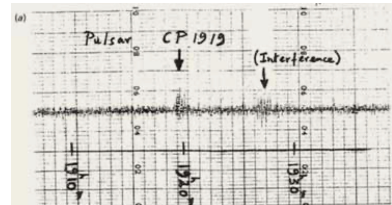


Figure 39.2: Graph of radio flux versus right ascension on the sky (see *Handout 1*), showing the anomalous signal detected by Bell and Hewish (marked as CP-1919).

¹ This relativistic motion arises because the neutrons are packed so tightly that all the lower-energy, sub-lightspeed states are all occupied (as Fermions, neutrons like electrons are subject to the Pauli exclusion principle).

There remains significant uncertainty about the correct equation of state to use in the inner parts of neutron stars; it's an area of active theoretical and experimental² research!

Pulsars

In 1967 the astronomers Jocelyn Bell and Anthony Hewish reported the detection of a source on the sky that emits radio-wave pulses every 1.33 s (see Fig. 39.2). This was the first discovery of a *pulsar* — a type of neutron star with rapid rotation and a strong magnetic field.

In the standard model for a pulsar, a strong electric field is generated by rapid rotation of the magnetic field (which is typically misaligned with the rotation axis; see Fig. 39.3). This electric field tears electrons and protons from the surface of the neutron star and accelerates them to relativistic speeds. As these particles spiral around the magnetic field lines, they emit synchrotron radiation in a tight beam aligned along the magnetic axis. If this beam periodically sweeps across the Earth (like a lighthouse beam periodically sweeping across a ship), a pulsed source of radiation like the Bell and Hewish detection is seen.

X-ray Binaries

It's not uncommon for neutron stars to be found in binary systems — the end result of the evolution of a pair of stars where one underwent a core-collapse supernova. In such cases, Roche-lobe overflow by the companion star (see *Handout 33*) can lead to the formation of an accretion disk around the neutron star (Fig. 39.4). This accretion disk is much more compact and hence much hotter than the disks in cataclysmic variable systems (*Handout 34*), and as a result radiates strongly at X-ray wavelengths³.

Such *X-ray binaries* (XRB) are important sources of high-energy photons on the sky. They are usually divided into two classes: high-mass X-ray binaries (HXRBS), where the companion is massive and luminous enough to detect at optical wavelengths; and low-mass X-ray binaries (LMXRBs), where the companion remains effectively invisible. In both cases, a variety of variability phenomena can manifest themselves. If sufficient accreted hydrogen and helium builds up on the surface of the neutron star for hydrogen-burning reactions to commence, then an outburst reminiscent of a nova occurs. However, these outbursts reach much higher temperatures than on white dwarfs⁴, and so are detected at X-ray wavelengths and known as *X-ray bursts*.

Further Reading

Kippenhahn, Weigert & Weiss, §38.

² The experimental dimension is provided by measurements of neutron star mergers, by the *Laser Interferometer Gravitational-Wave Observatory* (LIGO).

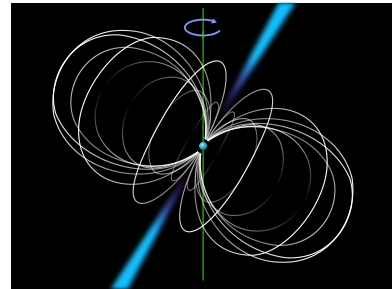


Figure 39.3: Schematic view of a pulsar. The sphere in the middle represents the neutron star, the curves indicate the magnetic field lines and the protruding cones represent the synchrotron emission beams. Credit: Mysid, from Wikipedia page for *Neutron Star*.

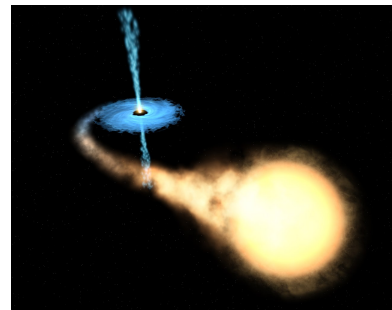


Figure 39.4: Artist's impression of a low-mass X-ray binary, showing a companion star (yellow) feeding an accretion disk (blue) via Roche-lobe overflow. In this case, the LMXRB contains a black hole rather than a neutron star, but the X-ray emission appears very similar in both cases. Image credit: NASA/ESA.

³ The neutron star itself also radiates in X-rays, but it is so small that its emission (at least, during quiescent phases) is dwarfed by disk emission.

⁴ This is because of the higher surface densities of neutron stars, which allow the runaway burning to continue for longer before degeneracy is lifted.

A Units & Constants

The Centimeter-Gram-Second System

It often comes as a shock to students that astronomers don't customarily use the SI system of units. Rather, they follow the *centimeter-gram-second* (cgs) system mixed with a variety of ad-hoc units based on convenience. As its name suggests, the cgs system adopts the centimeter ($1\text{ cm} = 1 \times 10^{-2}\text{ m}$) as the fundamental length unit, the gram ($1\text{ g} = 1 \times 10^{-3}\text{ kg}$) as the fundamental mass unit, and the second (s) as the fundamental time unit. These choices lead to the derived units given in Table A.1 below.

Quantity	Name	Conversion
Force	dyne	$1\text{ dyn} = 1\text{ g cm s}^{-2} = 1 \times 10^{-5}\text{ N}$
Energy	erg	$1\text{ erg} = 1\text{ g cm}^2\text{ s}^{-2} = 1 \times 10^{-7}\text{ J}$
Pressure	barye	$1\text{ Ba} = 1\text{ g cm}^{-1}\text{ s}^{-2} = 1 \times 10^{-1}\text{ Pa}$
Power	erg per second	$1\text{ erg s}^{-1} = 1\text{ g cm}^2\text{ s}^{-3} = 1 \times 10^{-7}\text{ W}$

The fundamental temperature unit in the cgs system is the kelvin (K), the same as in the SI system. When expressing wavelengths of electromagnetic radiation, the angstrom ($1\text{ \AA} = 1 \times 10^{-10}\text{ m}$) is used as a convenience; visible light spans the approximate range 4000 \AA – 7000 \AA .

This is likely a consequence of inertia: for a scientific field as old as Astronomy, change occurs at a slow pace.

Table A.1: Standard names for cgs derived units, together with their conversions to SI.

Physical Constants

In the cgs system, the fundamental constants we'll need throughout this course are given in Table A.2 below.

Name	Value
Gravitational constant	$G = 6.674 \times 10^{-8}\text{ cm}^3\text{ g}^{-1}\text{ s}^{-2}$
Boltzmann constant	$k_B = 1.381 \times 10^{-16}\text{ erg K}^{-1}$
Stefan-Boltzmann constant	$\sigma = 5.670 \times 10^{-5}\text{ erg cm}^{-2}\text{ s}^{-1}\text{ K}^{-4}$
Radiation constant	$a = 7.566 \times 10^{-15}\text{ erg cm}^{-3}\text{ K}^{-4}$
Speed of light in vacuum	$c = 2.998 \times 10^{10}\text{ cm s}^{-1}$
Planck constant	$h = 6.6261 \times 10^{-27}\text{ erg s}$
Electron mass	$m_e = 9.1094 \times 10^{-28}\text{ g}$
Proton mass	$m_p = 1.6726 \times 10^{-24}\text{ g}$
Hydrogen mass	$m_H = 1.6736 \times 10^{-24}\text{ g}$
Electron volt	$eV = 1.6022 \times 10^{-12}\text{ erg}$
Atomic mass unit	$u = 1.6605 \times 10^{-24}\text{ g} = 931.49\text{ MeV}/c^2$
Hydrogen ionization potential	$\chi = 2.1786 \times 10^{-11}\text{ erg} = 13.598\text{ eV}$

Table A.2: Useful physical constants in cgs units.

Astronomical Units

In addition to the cgs system, astronomers often use a system of supplementary units that are rooted in convenience. The nearest star out-

side the solar system, Proxima Centauri, is at a distance 4.02×10^{18} cm and has a mass 2.43×10^{32} g. These astronomically large numbers¹ are awkward to work with (especially when expressed verbally), and so we write them instead as 1.30 pc and 0.122 M_☉, respectively, where the parsec (pc) and the solar mass (M_☉) are defined in Table A.3 below. Most of the units in the table are defined with reference to the Sun² and solar system, which provide us a convenient yardstick with which to measure the cosmos.

Quantity	Name	Conversion
Length	Parsec	$1 \text{ pc} = 3.086 \times 10^{18} \text{ cm}$
Length	Astronomical unit	$1 \text{ au} = 1.496 \times 10^{13} \text{ cm}$
Length	Solar radius	$1 R_{\odot} = 6.957 \times 10^{10} \text{ cm}$
Mass	Solar mass	$1 M_{\odot} = 1.989 \times 10^{33} \text{ g}$
Power	Solar luminosity	$1 L_{\odot} = 3.828 \times 10^{33} \text{ erg s}^{-1}$

¹ Literally!

² Units relating to the Sun are indicated with the ☉ symbol (a dot inside a circle; or, if you prefer, a fried egg).

Table A.3: Astronomical units, together with their conversions to cgs. Note that the astronomical unit (singular) is based on the average distance from the center of the Earth to the center of the Sun.

Further Reading

A wealth of supplementary units, constants and other data can be found in *Allen's Astrophysical Quantities* (Cox 2000, 4th edition, AIP Press, New York).